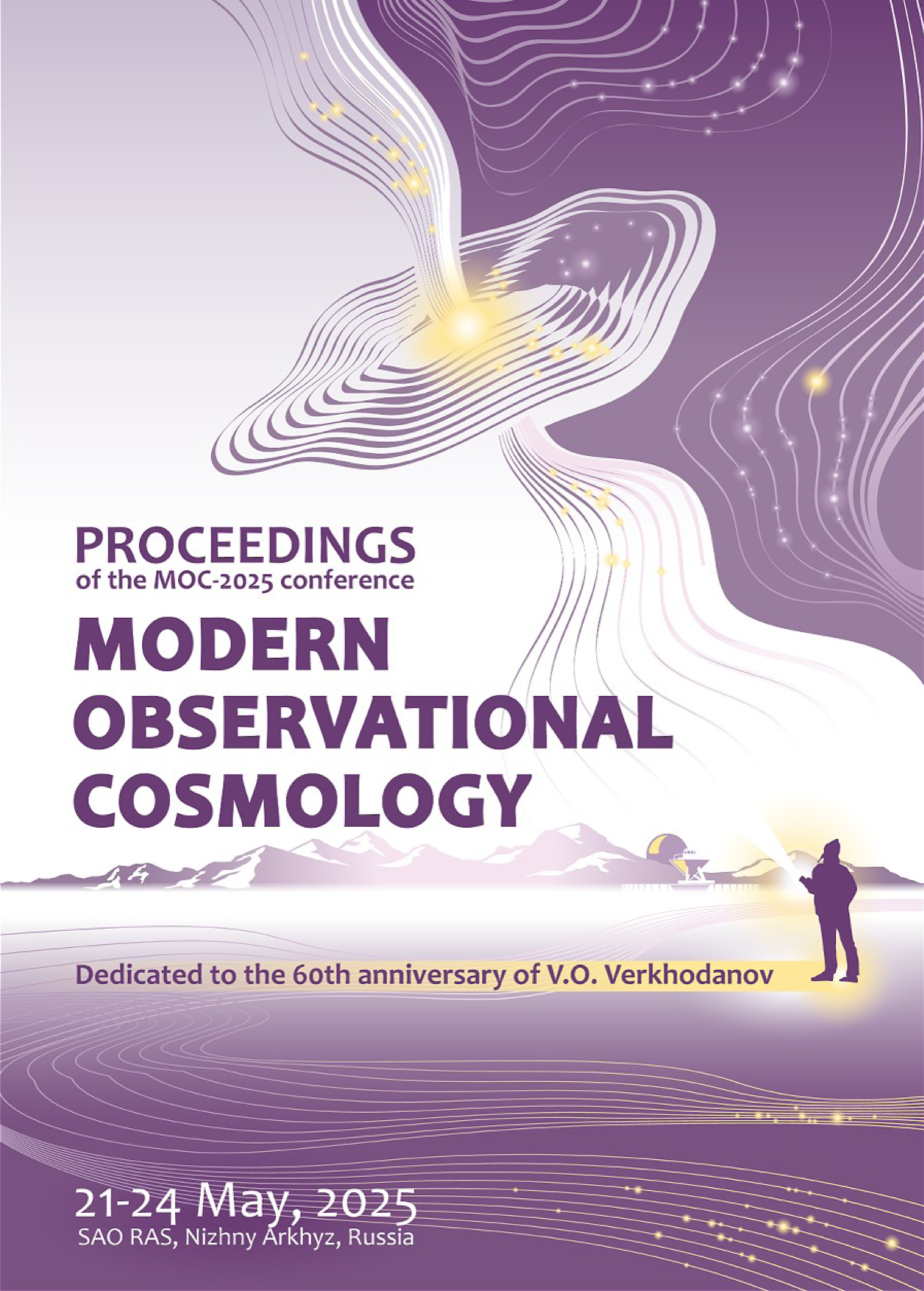

PROCEEDINGS
of the MOC-2025 conference

MODERN OBSERVATIONAL COSMOLOGY

Dedicated to the 60th anniversary of V.O. Verkhodanov

21-24 May, 2025
SAO RAS, Nizhny Arkhyz, Russia

Special Astrophysical Observatory
Russian Academy of Sciences

MODERN OBSERVATIONAL COSMOLOGY

DEDICATED TO THE 60TH ANNIVERSARY OF V.O. VERKHODANOV

Proceedings of the MOC-2025 conference
May 21–24, 2025

Edited by S.A. Trushkin, Yu.V. Sotnikova

Moscow
RIOR
2025

UDK 524.8(08)
BBK 22.637.6

Modern observational cosmology dedicated to the 60th anniversary of V.O. Verkhodanov.
Proceedings of the MOC-2025 conference, May 21–24, 2025 — Moscow, RIOR, 2025 (93 pp.)

ISBN 978-5-369-02171-2 (online)

Editors-in-Chief
Trushkin S. A., Sotnikova Yu. V.

Executive Editors-in-Chief
Kaisina E. I., Sotnikova Yu. V.

Scientific coordinators
Trushkin S. A., Doroshkevich A. G., Dagkesamanskii R. D., Ivanchik A. V., Kovalev Yu. A., Lukash V. N., Mamii D. K., Makarov D. I., Moiseev A. V., Pushkarev A. B., Stolyarov V. A., Vlasyuk V. V., Zinchenko I. I.

Technical editors
Cherepkova Yu. V., Sotnikova Yu. V., Kaisina E. I., Semenova T. A.

Editors of the English translation
Kudryavtsev D.O., Iuzhanina K.V.

Cover designer
Chmyreva E.G.

This volume contains papers based on the talks presented at the Russian Astronomical Conference MOC-2025 and comprises a wide range of the observational cosmology topics. We are grateful to all referees for their reviewing that helped us improve the Proceedings of the MOC-2025 conference.

Russian Astronomical Conference (MOC-2025)
Modern observational cosmology
dedicated to the 60th anniversary of V.O. Verkhodanov

The Special Astrophysical Observatory of the Russian Academy of Sciences (SAO RAS) has taken an initiative to hold the Russian Astronomical Conference MOC-2025 on the topical areas of observational cosmology carried out in the astronomical institutes of the Russian Federation. The conference is dedicated to the 60th anniversary of V.O. Verkhodanov.

The conference was held on May 21-34, 2025 at SAO RAS, Nizhny Arkhyz, Karachai-Cherkessian Republic

KEY CONFERENCE TOPICS
Early Universe
Galaxies and Cosmology
Multi-Channel Astronomy
Methods and Instruments
Astronomical Education and Outreach
Memorial

SCIENTIFIC ORGANIZING COMMITTEE
Trushkin S. A., SAO RAS, Dr. Sci.
Doroshkevich A. G., ASC, Dr. Sci.
Dagkesamanskii R. D., PRAO, Dr. Sci.
Ivanchik A. V., Ioffe Institute, Dr. Sci.
Kovalev Yu. A., ASC, Dr. Sci.
Lukash V. N., ASC, Dr. Sci.
Mamii D. K., ASU, PhD
Makarov D. I., SAO RAS, Dr. Sci.
Moiseev A. V., SAO RAS, Dr. Sci.
Pushkarev A. B., CrAO RAS, Dr. Sci.
Stolyarov V. A., SAO RAS, PhD
Zinchenko I. I. IAP RAS, Dr. Sci.

CHAIRMEN OF THE LOCAL ORGANIZING COMMITTEE
Sotnikova Yu. V., SAO RAS, PhD

INVITED SPEAKERS
Doroshkevich A. G., ASC, The “Dark” period of the Universe’s evolution and the formation of the first galaxies and magnetic fields
Lukash V. N., ASC, Dr. Sci., Cascade relaxation of the vacuum as a possible solution to observational cosmology problems
Ivanchik A. V., Ioffe Institute, Dr. Sci., The modern cosmology achievements and problems
Makarov D. I., SAO RAS, Dr. Sci., Galaxy flow in the Local Group
Popov S.B., SAI, Dr. Sci., Fast radio bursts
Shtern B.E., INR RAS, ASC, The DESI results and status of Hubble’s intensity

CONTENTS

Daily observations of blazars in the RATAN-600 Western Sector surveys

N. Bursov · A. Kudryashova · S. Trushkin

Special Astrophysical Observatory of the Russian Academy of Sciences,
Nizhny Arkhyz, 369167 Russia

DOI: 10.26119/2025-moc01
eLocator: moc01

EDN: dtejhv

Abstract. We present the results of a daily monitoring of blazars observed in survey mode with the RATAN-600 Western Sector in 2018–2019. Twelve blazars were observed in the survey at the declination of the Crab Pulsar and their light curves have been measured at 4.7 GHz. All the sources but one showed a radio variability level below 15%. The flux density of the blazar B2 1324+22 increased by a factor of two during the observing year. In 2019–2020, during a generally active state, a monitoring of the blazar PKS 1614+051 was conducted at 2.3 and 4.7 GHz. The flux density variability was low ($\sim$3%) at both frequencies. At 4.7 GHz the source was variable on a timescale of 25 days in its reference frame. A daily monitoring of the blazar AO 0235+164 was carried out at 2.3 and 4.7 GHz in 2021–2022. The light curves showed three repeating flares with a timescale of 57 days, and a periodicity of 52 days in the source's frame was found at 4.7 GHz.

Keywords: active galaxies: blazars; radio continuum

1. Introduction

Blazars are a class of active galactic nuclei (AGNs), known for their Doppler-boosted relativistic jets pointing nearly toward the observer's line of sight (Urry & Padovani 1995). Blazars exhibit emission and variability across the entire electromagnetic spectrum. They are divided into two subclasses: BL Lacertae objects (BL Lacs) and flat-spectrum radio quasars (FSRQs). In the radio band their emission is produced by the synchrotron and free-free radiation mechanisms. Studying the variability enables estimation of typical sizes of radiating regions and the distances between them. In this work we present a study of 14 blazars observed on a daily basis at 2.3 and 4.7 GHz with the RATAN-600 Western Sector.

The light curves of these blazars were examined as part of the sample in Kudryashova (2024). Additionally, two bright blazars, PKS 1614+051 and AO 0235+164, were studied in greater detail. General characteristics of the studied blazars, taken from the literature, are presented in Table 1.

The objects of the sample are in the redshift range from 0.3 to 4.2, the flux densities at 4.7 GHz are 34–1270 mJy with a median value of 230 mJy, the average spectral index $\alpha = -0.12$, the median radio luminosity of the FSRQ-type blazars is 1.5×10^{44} erg/s, while it is only 2.0×10^{42} erg/s for the rest of the objects.

2. Observations

The observations were carried out with the RATAN-600 Western Sector in round-the-clock radio survey mode using secondary mirror No. 5. The surveys were performed during a year at each of the three declinations: $22\overset{\circ}{.}0$, $16\overset{\circ}{.}5$, and $05\overset{\circ}{.}0$. Three or four identical four-channel radiometers at 4.7 GHz were used in all the observations, and an additional radiometer at 2.3 GHz was used in the surveys at $16\overset{\circ}{.}5$ and $05\overset{\circ}{.}0$.

The observed data were processed and analyzed as described in Kudryashova (2024). To increase the signal-to-noise ratio (S/N, where S is a signal in terms of antenna temperature, T_a), the data at 4.7 GHz were averaged over each radiometer channel and, if necessary, over several days. As a result, datasets for each object over 12 months were obtained. Further data processing resulted in the light curves with a daily or a three-day resolution for the sources with the highest S/N.

The obtained light curves at 4.7 GHz for the weaker (with lower S/N) and bright (with higher S/N) sources are presented in Figs. 1 and 2, respectively.

3. Radio variability analysis

The radio survey at Dec = $22\overset{\circ}{.}0$ was conducted in 2018–2019 at 4.7 GHz. A list of 205 bright sources has been obtained by Kudryashova (2024). Twelve of the radio sources are classified as blazars in the literature. In this work we improved the accuracy of their light curves and measured the variability.

To measure the variability level, we used the variability index defined in Alleret al. (1992):

$$V_S = \frac{(S_{\max} - \sigma_{S_{\max}}) - (S_{\min} + \sigma_{S_{\min}})}{(S_{\max} - \sigma_{S_{\max}}) + (S_{\min} + \sigma_{S_{\min}})}, \tag{1}$$

where $S_{\max}$ and $S_{\min}$ are the maximum and minimum flux densities, and $\sigma_{S_{\max}}$ and $\sigma_{S_{\min}}$ are their measurement errors.

The left panel of Fig. 3 shows the measured variability indices at 4.7 GHz compared to those for the sources of other types from Kudryashova (2024) depending on the measured flux densities. The distribution of the variability indices for 205 sources is shown in the right panel. It may be concluded that the blazar J132700+221050 (B2 1324+22) had the highest variability index

Table 1. General characteristics of studied blazars: col. 1 – the NVSS source name; col. 2 – redshift; col. 3 – type of the source; col. 4 – measured flux density with its error, in mJy; col. 5 – variability index with its error; col. 6 – two-frequency (1.4–4.7 GHz) spectral index with its error; col. 7 – luminosity of the source, in erg/s; col. 8 – reference: [1] – Ahumada et al. (2020); [2] – Gaia Collaboration et al. (2023); [3] – D'Abrusco et al. (2014); [4] – Massaro et al. (2009); [5] – Higley et al. (2020); [6] – D'Abrusco et al. (2019); [7] – Healey et al. (2008) [8] – Wilkes et al. (1983); [9] – Kudryashova (2024); [10] – Sotnikova et al. (2021); [11] – Cohen et al. (1987).

NVSS name	redshift	type	$S_{4.7} \pm \Delta S$	$V_S \pm \Delta V_S$	$\alpha \pm \Delta\alpha$	$L_{4.7}$	reference
(1)	(2)	(3)	(4)	(5)	(6)	(7)	(8)
J015218+220707	1.321	FSRQ	900±37	0.12±0.03	-0.10±0.04	2.26e+44	[1,4,9]
J023004+215909	0.529	bl.cand.	66±5	0.0±0.105	0.01±0.07	2.55e+42	[2,3,9]
J060351+215937	–	bl.cand.	1270±56	0.02±0.01	-0.64±0.04	-	[3,9]
J072614+215320	1.882	FSRQ	442±30	0.08±0.08	0.48±0.06	1.58e+44	[2,4,9]
J102016+220940	0.314	bl.cand.	61±4	0.0±0.125	0.11±0.06	7.32e+41	[5,6,9]
J103633+220312	0.595	FSRQ	265±20	0.11±0.03	0.01±0.02	1.02e+43	[4,5,9]
J105430+221055	4.161	BL Lac	52±4	0.10±0.07	-0.19±0.07	1.34e+44	[2,4,9]
J125433+221103	0.509	BL Lac	45±3	0.11±0.07	-0.67±0.07	2.00e+41	[4,5,9]
J132700+221050	1.398	FSRQ	690±23	0.29±0.01	-0.15±0.05	1.65e+44	[4,5,9]
J161847+215921	0.334	Unc.type	34±2	0.09±0.04	-0.69±0.06	5.61e+41	[4,5,9]
J171611+215214	2.380	FSRQ	298±14	0.04±0.07	-0.69±0.05	4.50e+44	[2,4,9]
J180738+220456	0.798	FSRQ	187±8	0.11±0.03	0.83±0.05	1.28e+43	[4,7,9]
PKS 1614+051	3.21	FSRQ	1100±30	0.02±0.001	0.51±0.09	8.63e+44	[4,8,9,10]
AO 0235+164	0.94	BL Lac	1560	0.32±0.07	0.37±0.07	1.79e+44	[4,9,11]

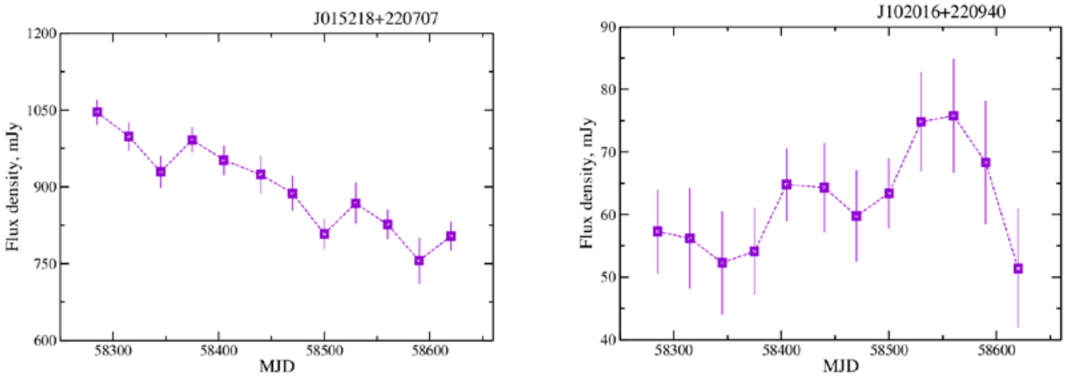

Figure 1. Light curves for the blazars NVSS J015218+220707 and NVSS J102016+220940 obtained by averaging daily records over 30 days.

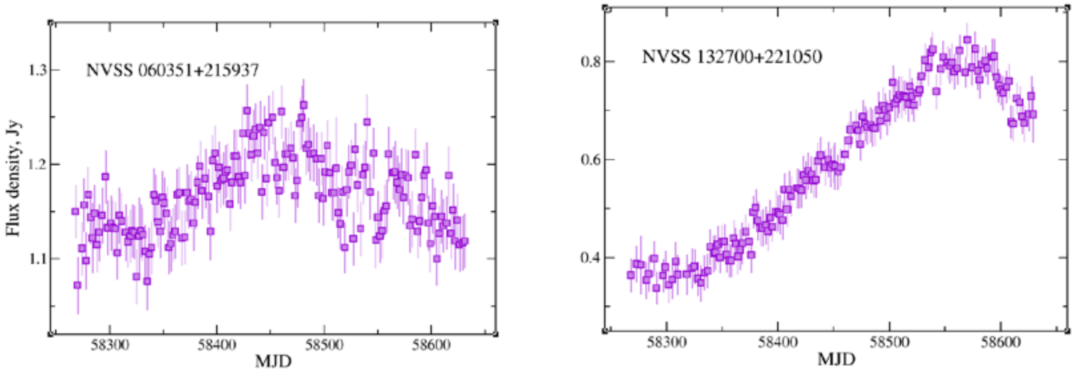

Figure 2. Light curves at 4.7 GHz for the blazars J060351+215937 and J132700+221050 obtained by averaging the observed data over 3 days.

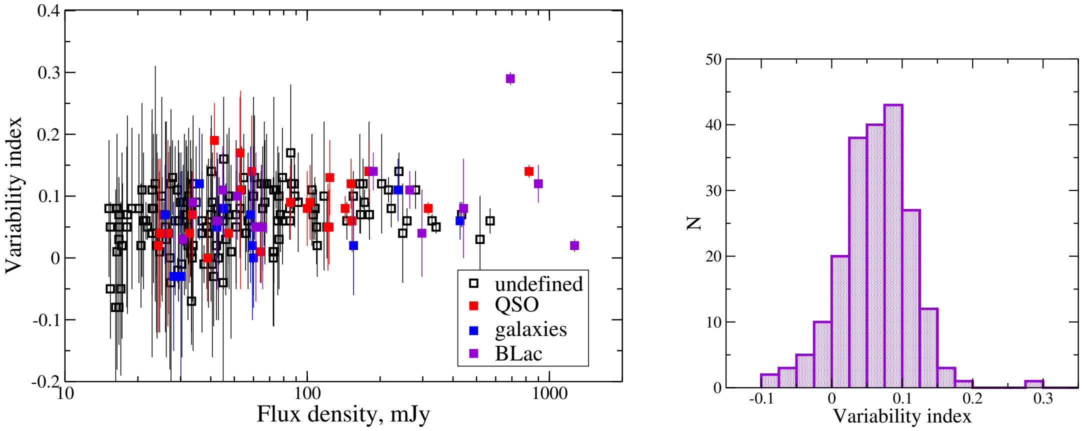

Figure 3. *Left:* the variability indices of the studied blazars compared to the sources of other types from Kudryashova (2024); *right:* the variability indices distribution.

$V_S = 0.3$. Its flux density increased by a factor of two during the observing year. For other sources, the variability indices $V_S < 0.2$.

Structure function (SF) analysis and the Lomb–Scargle (LS) periodogram were used for a more detailed study of the light curve variability properties. The SF analysis was developed by Kolmogorov in the turbulent plasma theory (Kolmogorov 1941a) and adopted by Simonetti, Cordes & Heeschen (1985) to search for typical timescales in astrophysical time series.

For the blazar B2 1324+22, SF analysis did not show any timescales, therefore it can be concluded that the timescales and periods, if exist, are significantly longer than the time span of our observations.

4. PKS 1614+051

The blazar PKS 1614+051 is of special interest due to its high redshift $z = 3.21$ (corresponding to about 15 % of the current age of the Universe), peaked spectrum in the radio band, and compact VLBI structure. It is classified as a gigahertz-peaked spectrum (GPS) radio source by O'Dea (1990) and later as a high-frequency-peaked (HFP) source by Dallacasa et al. (2000). One of the explanations for the nature of this class of radio sources is their young age. In this scenario, radio emission is produced inside the host galaxy and is affected by its interstellar medium. PKS 1614+051 was observed at 2.3 and 4.7 GHz in radio survey mode at RATAN-600 from May 2019 to June 2020. To improve the accuracy of the flux density measurements, we averaged three daily observations. The measured light curves are presented in Fig. 4 and indicate a slow decrease of flux density at 4.7 GHz throughout the period of observations. The median flux density uncertainty is $\sim 12\,\%$ for the data at 2.3 GHz and $\sim 2\,\%$ for 4.7 GHz.

The estimated variability level was quite low: $V_S = 0.03$. Using SF analysis, we found a typical timescale of 25 days in the source's reference frame. It gives a constraint on the emitting region size of less than a parsec. The LS periodogram did not reveal any significant periods.

5. AO 0235+164

The blazar AO 0235+164 at $z = 0.94$ is an object of various studies because of its brightness and the small angle between its jet and the observer's line of sight $\Theta = 1.7°$ (Kutkin et al. 2018) with an opening angle of $\sim 50°$ that makes it a useful object for investigating the jet properties. AO 0235+164 was observed with RATAN-600 daily from May 2021 to June 2022 at 2.3 and 4.7

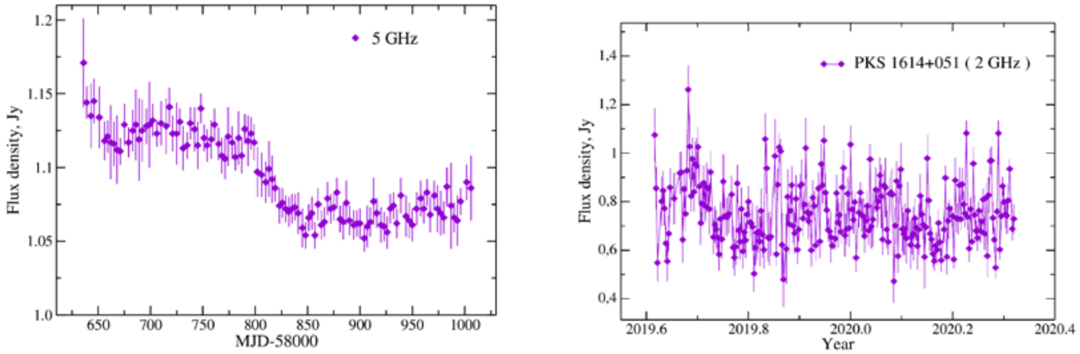

Figure 4. Light curve for blazar PKS 1614+051 obtained at 4.7 GHz (*left*) and 2.3 GHz (*right*) in a radio survey mode during from May 2019 to June 2020.

GHz. The measured light curves are presented in the left panel of Fig. 5. Their variability indices are $V_S = 0.22$ at 2.3 GHz and $V_S = 0.32$ at 4.7 GHz. The light curves exhibit three low-amplitude flares. To investigate their timescales and periodicity, we used SF analysis and the Lomb-Scargle periodogram. With the additional data at 5 GHz from Vlasyuk et al. (2024) (Fig. 5, right panel), four flares progressing in duration and amplitude are apparent. Outbursts lasting 3–5 days preceded each flare maximum.

We obtained a period of ~ 52 days in the source's reference frame with a false alarm probability of less than $1\,\%$. Thus, we can conclude about an episode of quasi-periodic behavior of AO 0235+164 from May 2021 to June 2022.

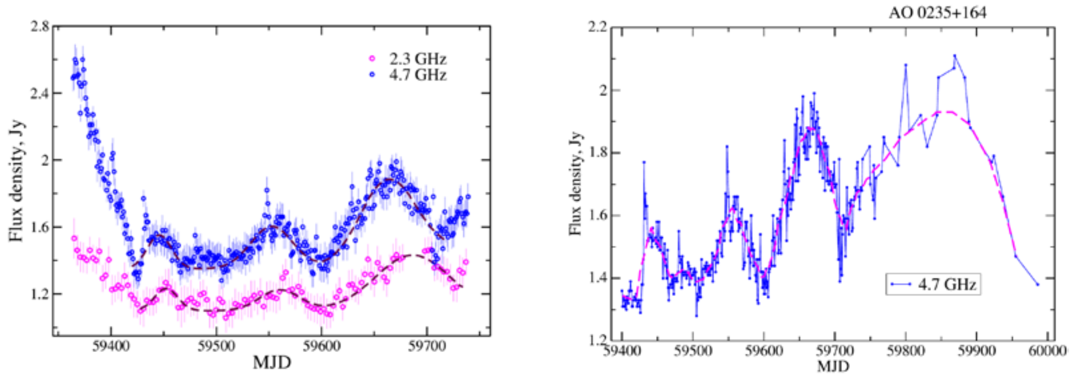

Figure 5. Light curves for the blazar AO 0235+164 obtained in 05.2021–06.2022 at 2.3 and 4.7 GHz.

SF analysis gave us a variability timescale of 57 days in the source's reference frame. Using discrete correlation function analysis, we obtained a time lag of 7 ± 1 days between the light curves at 2.3 and 4.7 GHz. Such a variability timescale and a time lag between 2.3 and 4.7 GHz give constraints on the emitting region radius $R \ll 1$ pc and on the distance between the emitting regions at the two frequencies of < 0.1 pc.

6. Summary

Daily observations at 2.3 and 4.7 GHz presented in this work give an opportunity to study shorter timescales and periods of the blazars variability. In this paper we analyzed the light curves of 14 blazars observed in radio survey mode at RATAN-600.

1. Among the 12 blazars observed at 4.7 GHz in 2018–2019, only B2 1324+22 showed significant variability with monotonic flux density growth without any timescales within the period of observations.
2. During daily observations in 2019–2020, the HFP blazar PKS 1614+051 showed at 2.3 and 4.7 GHz a low variability $V_S = 0.03$. At 4.7 GHz a variability timescale of 25 days in the source's reference frame was found, without any significant periodicity. The size of emitting region is estimated as less than 1 parsec.
3. The extremely compact blazar AO 0235+164, observed on a daily basis at 2.3 and 4.7 GHz, showed complex variability behavior during 2021–2022. Repeating flares with a period of ~ 52 days and a timescale of 57 days were found. By DCF analysis a time lag of 7 ± 1 days between the emission at 2.3 and 4.7 GHz was measured. This corresponds to a radius of the emitting region $R \ll 1$ parsec and a distance between the emitting regions at the two frequencies of < 0.1 pc.

Acknowledgements Observations with the SAO RAS telescopes are supported by the Ministry of Science and Higher Education of the Russian Federation. The renovation of telescope equipment is currently provided within the national project “Science and Universities.” This research has made use of the VizieR catalog access tool, CDS, Strasbourg Astronomical Observatory, France, and the CATS database, available on the Special Astrophysical Observatory website.

Funding

The work was performed as part of the SAO RAS government contract approved by the Ministry of Science and Higher Education of the Russian Federation.

References

Ahumada R., Allende Prieto C., Almeida A., et al., 2020, The Astrophysical Journal Supplement Series, 249, id. 3
Aller M., Aller H., Hughes P., et al., 1992, Astrophysical Journal, 399, id. 16
Cohen R.D., Smith H.E., Junkkarinen V.T., et al., 1987, Astrophysical Journal, 318, p. 577
D'Abrusco R., Massaro F., Paggi et al., 2014, The Astrophysical Journal Supplement, 215, id. 14
D'Abrusco R., Á lvarez Crespo N., Massaro F., et al., 2019, The Astrophysical Journal Supplement Series, 242, 1, id. 4
Dallacasa D., Stanghellini C., Centonza M., et al., 2000, Astronomy and Astrophysics, 363, p. 887
Gaia Collaboration, Vallenari A., Brown A.G.A., 2023, Astronomy and Astrophysics, 674, id. A1
Healey S.E., Romani R.W., Cotter G., et al., 2008, The Astrophysical Journal Supplement Series, 175, p. 97
Higley A.N., Lyke B.W., Myers A.D., et al., 2020, American Astronomical Society, 235, id. 219.03
Kolmogorov A.N., 1941, Doklady Akademii Nauk SSSR, 30, p. 299
Kudryashova A.A., Bursov N.N., Trushkin S.A., 2024, Astrophysical Bulletin, 79, p. 36
Kutkin A.M., Pashchenko I.N., Lisakov M.M., et al., 2018, Monthly Notices of the Royal Astronomical Society, 475, p. 4994
Massaro E., Giommi P., Leto C., et al., 2009, Astronomy and Astrophysics, 495, p. 691
O'Dea C.P., 1990, Monthly Notices of the Royal Astronomical Society, 245
Simonetti J.H., Cordes J.M., Heeschen D.S., 1985, Astrophysical Journal, 296, p. 46
Sotnikova Yu., Mikhailov A., Mufakharov T., et al., 2021, Monthly Notices of the Royal Astronomical Society, 508, 2, p. 2798
Vlasyuk V.V., Sotnikova Y.V., Volvach A.E., et al., 2024, Monthly Notices of the Royal Astronomical Society, 535, p. 2775
Urry C.M. and Padovani P., 1995, Publications of the Astronomical Society of the Pacific, 107, p. 803
Wilkes B.J., Wright A.E., Jauncey D.L., et al., 1983, Astronomical Society of Australia, Proceedings, 5, 1, p. 2

Variability of the blazar S5 1803+784 in July 2019 - December 2024 as a manifestation of the jet flow structure

**M. Butuzova · M. Gorbachev · V. Guseva · A. Krivenko ·
S. Nazarov · G. Baida**

Crimean Astrophysical Observatory of the Russian Academy of Sciences,
Nauchny, 298409 Russia

DOI: 10.26119/2025-moc02 EDN: wzqnfr
eLocator: moc02

Abstract. The TESS satellite provides unique data from nearly continuous observations with high temporal resolution. Each sky sector is observed for 27 days. For the blazar S5 1803+784, there are three observing seasons during which the object remains in the TESS field of view for extended periods, approximately 10 months in total. By supplementing these data with multi-band photometric observations from the Zwicky Transient Facility (ZTF) and the AZT-8 telescope at the Crimean Astrophysical Observatory of the Russian Academy of Sciences, we obtain a unique opportunity to study the relation between the shortest characteristic variability timescales and the parameters of long-term variability. Based on this analysis, we conclude that short-term variability is caused by the emergence and evolution of jet regions, whose motion deviates from the general trajectory, and, therefore, they have different Doppler factors. We performed light curve modeling under this assumption and obtained good qualitative agreement with the observations.

Keywords: active galaxies: blazars; optical variability

1. Introduction

Blazars exhibit prominent variability on timescales ranging from several hours to several years. Variability on timescales of several days has been poorly studied due to limitations imposed by Earth's diurnal rotation and weather conditions, which prevent continuous data collection over multiple days at a single observatory. To address this, international observational campaigns have previously been performed, such as the Whole Earth Blazar Telescope (WEBT). The situation has changed with the launch of the Transiting Exoplanet Survey Satellite (TESS). TESS observes a $24^\circ \times 96^\circ$ patch of the sky for 27 days (one sector) with a time resolution of 2 to 30 minutes. Afterwards, the observed field is shifted. Regions near the ecliptic poles are observed most frequently, allowing objects in these areas to accumulate long, nearly continuous light curves spanning several months to a year. We used such a unique dataset to study the blazar S5 1803+784. In Section 2, we describe the method used to construct the blazar's light curve from TESS data, taking into account the object's low brightness and the characteristics of TESS's CCD detectors. Section 3 presents the results of our analysis of the evolution of the shortest characteristic variability timescale (τ), and the search for possible correlations between τ and photometric variability properties as well as the spectral index α (defined as $F \propto \nu^\alpha$). Section 4 contains the results of light curve modeling under the assumption that the internal flow structure is responsible for the formation of variability on a short time scale. Discussion and conclusions are presented in Section 5.

2. Data

TESS provides three types of data products: SAP and PDCSAP light curves, and Full Frame Images (FFIs). SAP light curves account only for background subtraction. PDCSAP light curves include corrections for instrumental systematics and the overall field trend. Some authors (Weaver et al. 2020; Raiteri et al. 2021a,b) note that only SAP light curves are suitable for studying blazars, as they correspond to light curves obtained with ground-based telescopes, while the PDCSAP light curves remove long-term trends of astrophysical origin.

Since blazars are faint sources, both their SAP and PDCSAP light curves are strongly affected by Poisson noise, which distorts analyses of temporal variability properties (Butuzova et al. 2025; Gorbachev & Butuzova 2025). To reduce the noise component, we performed relative photometry of the blazar using cuts from the full-frame images, following the method proposed by Butuzova et al. (2025). The exposure time per image varied across TESS sectors; therefore, the number of cuts used for co-addition was varied and determined empirically to achieve a photometric precision better than 0.02 magnitudes. The comparison stars used in our analysis are listed in Table 1. Resulting TESS light curves are obtained for magnitudes.

One of the characteristics of TESS data is the variation in the zero point of the instrumental flux between different sectors. Additionally, we found that even within the same CCD chip, this zero point changes in an uncorrelated manner between adjacent sectors (Fig. 1). To demonstrate this effect, we selected sector 14 as a reference and identified several sources with no significant intrinsic variability that were observed in sectors 14, 15, and 16 on the same CCD chip. For each selected source, we computed the median SAP flux in each sector, and then calculated the difference between the median fluxes in sectors 15 and 16 relative to sector 14: $\Delta F^i = F^{14}_{\text{median}} - F^i_{\text{median}}$, where i is the sector index. We then normalized the data in each sector by subtracting the median flux values. To account for zero-point shifts, the corresponding ΔF^i value was added to the normalized fluxes in sectors 15 and 16.

Differences in CCD chip sensitivity must be taken into account when constructing a combined light curve of an object over multiple sectors. To do this, we used a combined ground-based light curve as a reference, constructed as follows. We matched the R-band photometry from the AZT-8 telescope to the g-band ZTF light curve for two observation seasons 2022 and 2024, for which AZT-8 data are available. For each observing intervals, we shifted the R-band light curve relative

Table 1. Stars used in the photometry of the S5 1803+784 blazar conducted for FFI cuts.

Star	R.A.	Dec.	TESS magnitude
TIC 288430540	269.83017	+78.50756	13.78
TIC 288432310	269.98167	+78.44307	13.82
TIC 288432315	270.40571	+78.44980	15.63
TIC 288432354	270.10727	+78.54506	15.66

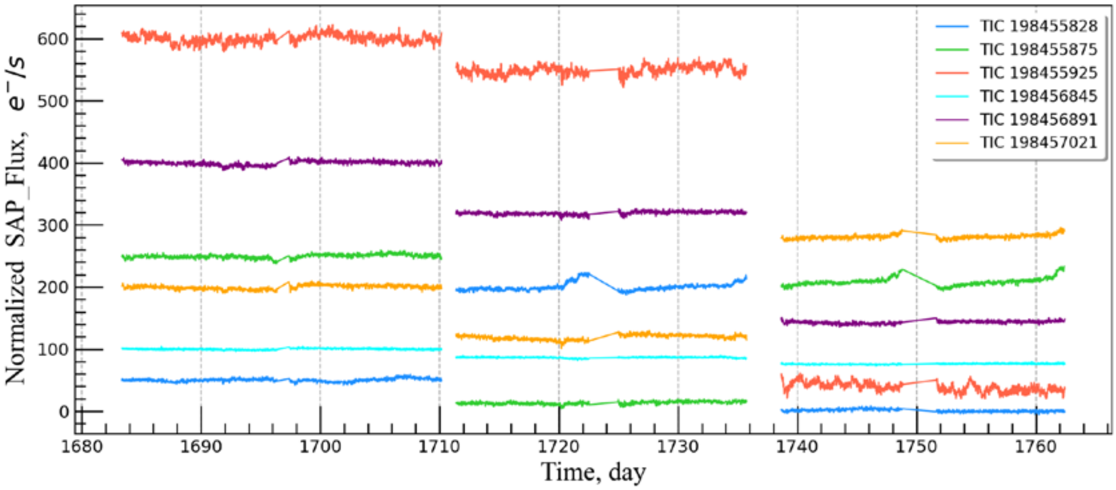

Figure 1. The change in the instrumental flux of six stars falling on one CCD in the period from sector 14 to 16. For ease of comparison, the data from different sources are presented with a vertical offset relative to each other.

to the g-band in such a way that the sum of squared differences between the R-band data points and the linear interpolation between the two nearest g-band points at the corresponding R-band epochs was minimized. The derived offsets were 0.72 and 0.67 magnitudes for 2022 and 2024, respectively.

Similarly, each continuous segment of the TESS light curve was aligned with the combined ground-based light curve of ZTF and AZT-8. However, some intervals of uniformly sampled TESS data lacked corresponding g- and R-band measurements or contained only a very small number of such points. For these segments, the vertical offset of the TESS light curve was determined by matching the flux levels at the edges with adjacent segments. These segments were excluded from further analysis. As for example, the final combined light curve is presented in the left panel of Fig. 2. Right panel shows obtained TESS light curves for observed seasons 2019-2020 (top) and 2024 (bottom).

Using ZTF and AZT-8 data, we calculated the spectral index following the method described by Gorbachev et al. (2024). The spectral indices derived from ZTF data are statistically lower than those based on AZT-8 data. We attribute this difference to the fact that AZT-8 observations were performed simultaneously in four photometric bands, whereas ZTF provides quasi-simultaneous observations (separated by one to two days) in two bands, and rarely in three, for the blazar S5 1803+784. On the basis of the ZTF data, we constructed a combined spectral index evolution curve using the same method applied to the light curves.

Due to data gaps within each TESS sector, a single continuous data segment spans only about ten days. The blazar S5 1803+784 was observed over three seasons, each consisting of several consecutive TESS sectors, sometimes separated by a gap of one or two sectors (Fig. 2). Each of these seasons (July 19, 2019 – June 8, 2020; December 31, 2021 – January 18, 2023;

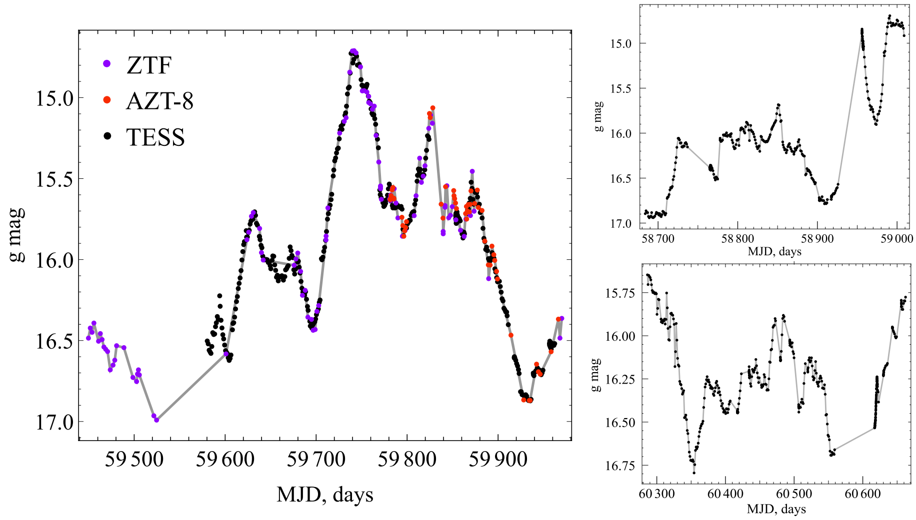

Figure 2. The light curves of the blazar S5 1803+784 for the period from 02.05.2019 to 13.07.2020 (right top), from 22.08.2021 to 21.01.2023 (left), and from 12.10.2023 to 20.12.2024 (right bottom).

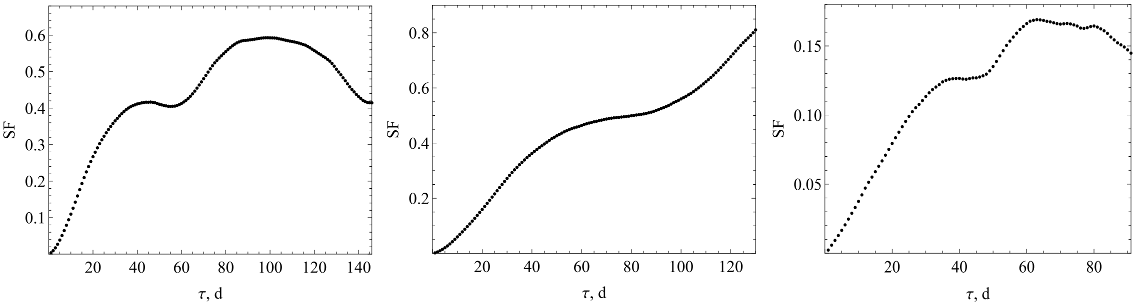

Figure 3. Structure functions for the three observation seasons of the blazar S5 1803+784. The maximum value along the abscissa axis is one third of the duration of the interval for which the corresponding SF is calculated.

and December 7, 2023 – December 18, 2024) covers approximately one year of high-cadence observations. These data are unique and enable the study of correlations between blazar flux variability properties on different timescales (Table 2). The fact that S5 1803+784 exhibited different mean brightness, variability amplitude, and characteristic variability timescale during each season (see Section 3) allows us to analyze the relationship between the shortest characteristic variability timescale and the photometric parameters of long-term variability, to identify the physical mechanisms driving variability at different timescales.

3. Relation of temporal and photometric variability properties

Since the blazar variability has a stochastic character, we consider it enough to find the characteristic variability time τ as the time interval during which it is possible to register an object's brightness change in both directions. Thus, τ is the position of the maximum of the structure function (SF) defined by Simonetti et al. (1985). In this case, the peak value of SF represents the square of the average variability amplitude within the considered time interval. To determine τ for observation intervals for almost a year, we used a combined light curve in the g, R, and TESS bands (Fig. 2), in which the TESS data were averaged over one day. Then, for data points evenly spaced for one day, we determined the magnitudes using linear interpolation between two adjacent data points. Then we calculated SF (Fig. 3) and obtained τ (Table 2).

Table 2. Characteristics of the long-term variability of the S5 1803+784 blazar.

Interval	designation in the text	median magnitude	amplitude	median spectral index	characteristic time of variability, d
07.2019 – 06.2020	2019	16.5	2.36	−1.68	43.0 and 93.3
12.2021 – 01.2023	2022	15.91	2.16	−1.64	76.4
12.2023 – 12.2024	2024	16.26	1.14	−1.56	33.9 and 64.3

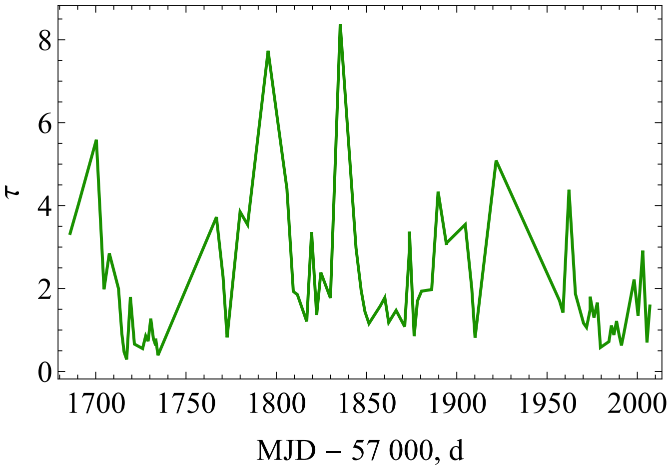

Figure 4. The evolution of the shortest characteristic time of variability for the period from 05.2019 to 07.2020.

On short time scales, variability occurs with smaller amplitude, so its characteristic time does not manifest in SF computed from data over long time intervals. Additionally, the characteristics of the process responsible for short-term variability may change over time, or the process itself may be replaced by another one. This leads to variations in τ of short-term variability. To determine τ, we used the method proposed by Butuzova et al. (2025), which involves adding data points to a short time series until a statistically significant maximum (at the 0.95 confidence level) appears in SF. The next consecutive short time series is then selected, and the procedure is repeated. This method was applied to segments of continuous, uniformly sampled TESS data. Figure 4 shows the evolution of the characteristic variability timescale from May 2019 to July 2020. It can be seen that τ varies by a factor of several times between neighboring time intervals.

For each interval with a determined τ, we calculated the average variability amplitude ($\overline{\text{var ampl}}$), the mean magnitude ($<\text{mag}>$), the maximum brightness variation (Δmag), and the spectral index. Figure 5 shows the relations between these parameters. The absence of a dependence between Δmag and τ indicates that long-term trends do not significantly affect variability on short timescales.

Blazar brightness variability is caused either by physical changes within the jet — such as the passage of a shock (Marscher & Gear 1985) — or by variations in the relativistic boosting factor (Doppler factor) due to changes in the jet's speed and/or direction relative to the observer. On short timescales, flux variations may arise, for example, from turbulent cells passing through a shock front (TEMZ model, Marscher (2025)). Alternatively, inhomogeneities and instabilities in the jet flow may give rise to regions (subcomponents) moving at some angle relative to the general jet trajectory, thereby resulting in a different Doppler factor. The continuous emergence and evolution of such subcomponents lead to variability characterized by a changing color index behavior with brightness (Butuzova 2021; Gorbachev et al. 2022), whereas physical changes within the jet would typically produce a clear dependence of the color index with brightness. Figure 5f shows no such dependence across all data under consideration.

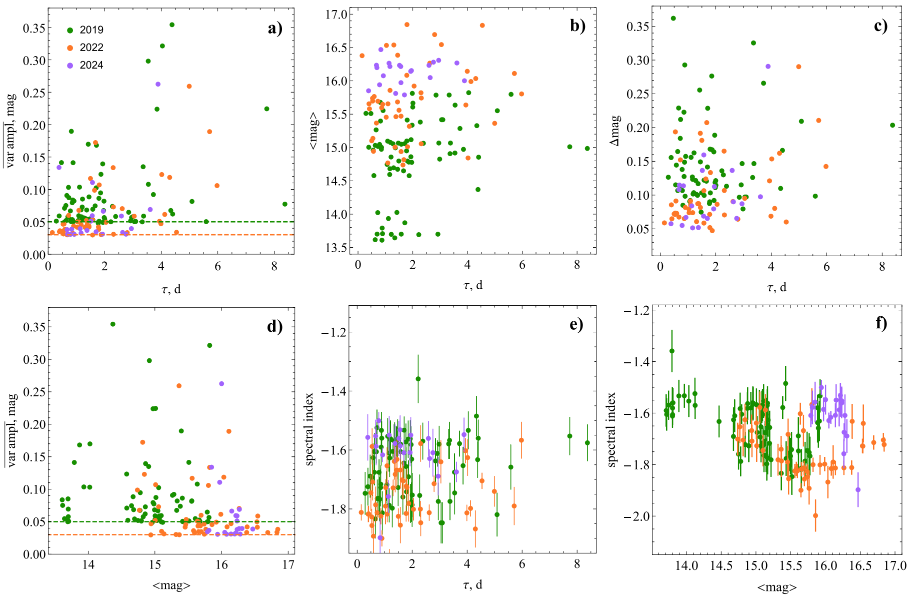

Figure 5. The correlation between photometric and temporal characteristics of the variability of the S5 1803+784 on various time scales. The dotted line on graphs ***a*** and ***d*** indicates the minimum value of the average amplitude of variability from which the calculation of the significance level of the SF peak begins when searching for the shortest characteristic time of variability.

Notably, the range of τ values does not depend on the spectral index (Fig. 5e) and remains approximately constant across all three observing seasons, during which the source exhibited different brightness levels (Fig. 5b). If the variability was driven by physical changes in the jet, this behavior would require an implausibly fine-tuned adjustment of parameters.

On the other hand, if long-term variability was caused by changes in the Doppler factor, then τ would decrease with increasing brightness. This trend is not observed (Fig. 5a), and its absence can be explained by the fact that subcomponents have different sizes (Butuzova 2021; Butuzova et al. 2025). If all subcomponents had the same size but different Doppler factors, the average variability amplitude would be larger for smaller τ values. Conversely, if the Doppler factors were the same but the sizes varied, the relation would be inverse. Furthermore, the continuous action of a single physical process driving short-term variability throughout all observing seasons is supported by the fact that the distribution of τ values follows a log-normal distribution with $\mu = 0.43$ and $\sigma = 0.75$ (Pearson $\chi^2 = 0.55$; Fig. 6).

4. Modeling of the light curve

We performed light curve simulations under the assumption that variability arises from subcomponents within the jet. To do this, we applied the formulas from (Butuzova 2021) to the geometric configuration described in (Gorbachev & Butuzova 2025). Specifically, we modeled the optical-emitting region as a cylinder with a length of $5 \cdot 10^{-2}$ pc and a radius of $5 \cdot 10^{-4}$ pc. Subcomponents appear randomly in time and location within this region, each moving along a helical trajectory on the surface of a cone with a half-opening angle $\chi \leqslant 4°$. The cone's axis coincides with the jet axis and is oriented at an angle of 5° to the line of sight. The angle between the cone generatrix and the subcomponent's velocity vector ranges from 1° to 10°. The velocities of both the jet and subcomponents are assumed to be $0.99c$, where c is the speed of light. The total volume of simultaneously existing subcomponents does not exceed 30% of the emitting region's volume. The flux of the non-variable component in the observer's frame is 1 mJy.

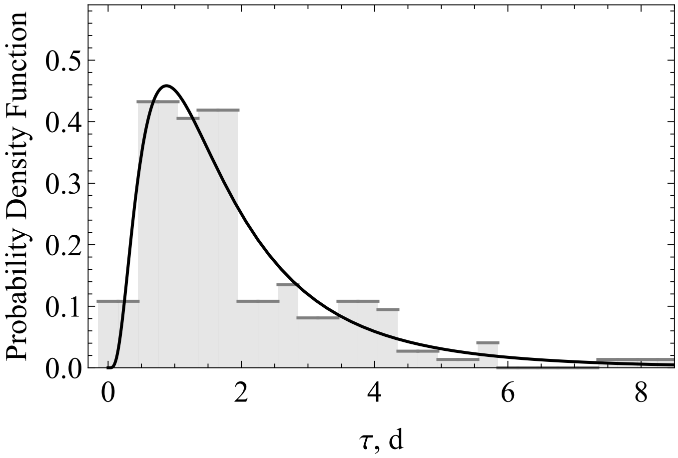

Figure 6. The probability density for τ and its fitting by a log-normal distribution.

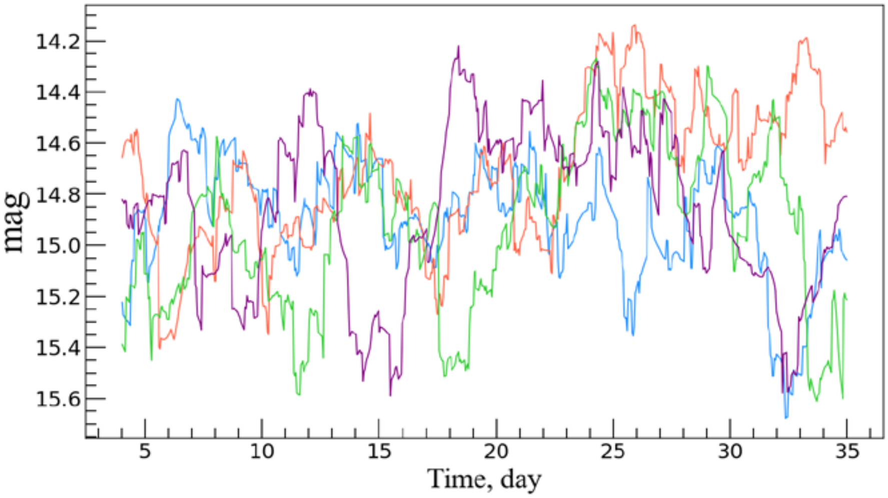

Figure 7. Light curves generated under the assumption of the appearance and evolution of subcomponents in the jet flow moving along a helical line relative to the axis of the emitting region. The different colors correspond to different realizations of the model's light curves.

Figure 7 shows a qualitatively good agreement between the simulated and observed light curves of the blazar S5 1803+784, namely, there are alternating individual sharp-peak flares. Importantly, the azimuthal angle of each subcomponent changes by only a few degrees during its passage through the emitting region. Therefore, the flares seen in the model light curves (Fig. 7) arise from the superposition of emission from multiple subcomponents, rather than from the rotation of a single subcomponent around the jet axis.

5. Summary

Over the observed period, the brightness of the blazar S5 1803+784 varied from 16.9 to 14.7 magnitudes in the g-band, while the spectral index ranged from −2.0 to −1.36. The long-term variability is achromatic.

The shortest characteristic variability timescale ranges from 0.2 to 8.5 days and changes irregularly between adjacent time intervals on the light curve, sometimes by factor of several times. The distribution of τ follows a log-normal law with $\mu = 0.43$ and $\sigma = 0.75$. This, together with the absence of correlations between τ and both short-term (variability amplitude) and long-term (mean brightness, spectral index) photometric parameters, suggests that the short-timescale variability arises from the emergence and evolution of subcomponents—regions within the jet flow that move at an angle relative to the overall jet trajectory. Light curve simulations based on this assumption show good qualitative agreement with the observed light curves.

Acknowledgements This paper includes data collected by the TESS missions and obtained from the MAST data archive at the Space Telescope Science Institute (STScI). Funding for the TESS mission is provided by the NASA Explorer Program.

Based on observations obtained with the Samuel Oschin Telescope 48-inch and the 60-inch Telescope at the Palomar Observatory as part of the Zwicky Transient Facility project.

Funding

This work was supported by the Russian Science Foundation, No. 24-22-00343.

References

Butuzova M.S., Guseva V.A., Gorbachev M.A., et al., 2025, Journal of High Energy Astrophysics, 45, p. 19
Butuzova M.S., 2021, Astroparticle Physics, 129, id. 102577
Gorbachev M.A. and Butuzova M.S., 2025, Astronomical and Astrophysical Transactions, in press
Gorbachev M.A., Butuzova M.S., Nazarov S.V., et al., 2024, Astroparticle Physics, 160, id. 102965
Gorbachev M.A., Butuzova M.S., Sergeev S.G., et al., 2022, Astrophysical Journal, 928, 1, p. 86
Marscher A.P. and Gear W.K., 1985, Astrophysical Journal, 298, p. 114
Marscher A.P., 2014, Astrophysical Journal, 780, 1, p. 87
Raiteri C.M., Villata M., Carosati D., et al., 2021a, Monthly Notices of the Royal Astronomical Society, 501, 1, p. 1100
Raiteri C.M., Villata M., Larionov V.M., et al., 2021b, Monthly Notices of the Royal Astronomical Society, 504, 4, p. 5629
Simonetti J.H., Cordes J.M., Heeschen D.S., 1985, Astrophysical Journal, 296, p. 46
Weaver Z.R., Williamson K.E., Jorstad S.G., et al., 2020, Astrophysical Journal, 900, 2, p. 137

A sample of giant radio sources from the NVGRC catalog

O. Zhelenkova[1] · **M. Khoruzhenko**[2]

[1] Special Astrophysical Observatory of the Russian Academy of Sciences, Nizhny Arkhyz, 369167 Russia

[2] Southern Federal University, Bolshaya Sadovaya st., 105/42, Rostov-on-Don,
344006 Russia

DOI: 10.26119/2025-moc03 EDN: edblkj
eLocator: moc03

Abstract. The NVGRC catalog contains radio sources selected by a pattern recognition algorithm as candidates for giant radio sources (GRSs). Besides genuine GRSs, the catalog includes sources with sizes below 0.7 Mpc and objects erroneously classified as single sources. We examined 370 NVGRC sources along with radio sources located within one degree of the target. The results showed that 48 % of objects are genuine GRSs, 14 % are compact sources with sizes under 0.7 Mpc, and 38 % are misclassified objects. Our study identified 197 giant sources, including 72 previously known GRSs and 125 newly confirmed GRSs. Analysis of the FRItoFRII ratio in the sample revealed nearly equal proportions of these types at $z < 0.05$. At higher redshifts ($z > 0.15$), there is a sharp decrease in the proportion of FRI sources. The predominance of FRII sources in GRS catalogs likely stems from observational selection effects caused by the sensitivity limitations of current radio surveys. Environmental analysis of the GRS sample demonstrated that 39 % have close neighbours within 50 kpc (based on photometric redshifts), 28 % reside in groups or clusters according to published data. When considering radio sources with deformed lobes, nearly 70 % of GRSs appear to be located in relatively dense environments.

Keywords: active galaxies: giant radio sources; general radio continuum

1. Introduction

Giant radio sources are galaxies or quasars, in which the linear size of the radio structure in the projection onto the celestial plane exceeds 0.7 Mpc. The largest known GRSs are approximately 5 Mpc in size, which is comparable to a galaxy cluster. By 2020, approximately 900 GRGs had been discovered (Willis et al. 1974; Lara et al. 2001a; Schoenmakers et al. 2001; Machalski et al. 2001, 2006; Saripalli et al. 2005; Solovyov & Verkhodanov 2014b; Dabhade et al. 2017, 2020; Kuzmicz et al. 2018), and they were considered to be relatively rare objects. Currently, about 12000 GRSs are known (Andernach et al. 2021; Oei et al. 2023; Mostert et al. 2024; Simonte et al. 2024). They were particularly numerous in the coverage area of the LoTSS low-frequency survey, which is characterized by high sensitivity. In other regions of the sky, their detection rate remains relatively low due to the lack of sensitive low-frequency surveys.

There are following hypotheses explaining the size of GRGs. One of them is related to the assumption that the radio source is located in a less dense IGM (InterGalactic Medium), which allows the lobes to expand unhindered (Subrahmanyan et al. 2008; Safouris et al. 2009; Malarecki et al. 2015). Another explanation is the large age of the radio structure, i.e. GRSs are old radio sources (Kaiser et al. 1997). And thirdly, the size is determined by the special properties of the galaxy nucleus, i.e. black hole mass, spin, and accretion rate (Kuzmicz & Jamrozy 2012). It is believed that the GRS is the final phase of the existence of a radio source generated by the galaxy nucleus. Murgia et al. (1999); Parma et al. (1999); Murgia (2003); Jamrozy et al. (2008) have revealed a tendency for the spectral age of radio sources to correlate with linear sizes, i.e. a large age is more often associated with large linear size. However, there also are old radio sources with small sizes that are up to 10^8 years old (Murgia et al. 2011).

Most of the known GRSs are located at close redshifts and are associated with bright elliptical galaxies, classified as FRII type (Fanaroff & Riley 1974) radio sources with radio luminosities in the range of 10^{23}–$10^{28}\mathrm{W\cdot Hz^{-1}}$ at 1.4 GHz.

GRSs can assist in determining IGM properties. This is due to studies of the interactions of the lobes of radio sources with the environment, detected by the asymmetry of radio structures. Their large size also makes it possible to study the distribution of the warm-hot intergalactic medium in the voids of the large-scale structure of the Universe (Pirya et al. 2012; Malarecki et al. 2015; Peng et al. 2015; Safouris et al. 2009).

Giants transport matter from the host galaxy over long distances and enrich IGM/ISM with non-thermal particles and magnetic fields (Kronberg 1994). This magnetized plasma can exist for billions of years and become a source of injection of high-energy particles into the intracluster medium (Enblin & Gopal-Krishna 2001; van Weeren et al. 2010). GRGs may play an important role in magnetizing the IGM (Oei et al. 2022). The megaparsec-sized radio lobes are the largest natural reservoirs of magnetic field and non-thermal relativistic particles associated with the galactic system, and store most of the energy released by black holes for a very long time (Kronberg et al. 2001). This makes GRSs a good tool for estimating the energy produced by central black holes. The extended GRS lobes with charged particles are large enough to accelerate particles to extremely high energies, and it is assumed that shock waves in radio jets and GRS lobes can generate cosmic rays (Kronberg et al. 2004; Hardcastle et al. 2009).

It was found that the IGM density is quite low in the vicinity of some GRSs (Machalski et al. 2006; Malarecki et al. 2015). Although no association was found between GRSs and voids (Kuzmicz et al. 2018). Moreover, Komberg & Pashchenko (2009) showed that there is no correlation between the size of the radio source and the density of galaxies in its vicinity.

GRGs with sizes $> 4'$ are of particular interest in terms of separating the emission of radio sources from the microwave background, as well as the contribution of sources of different natures to the angular power spectrum used in selecting a cosmological model (Solovyov & Verkhodanov 2014a; Verkhodanov et al. 2016).

Since the IGM density increases as $\rho \propto (1+z)^3$ (Kapahi 1989), the expansion of radio lobes should be difficult at high redshifts. In addition, the surface brightness decreases with redshift as

$(1+z)^{-4}$. This makes it difficult to detect extended radio structures of GRGs in earlier cosmological epochs.

For our work, we used the NVGRC catalog, which was compiled by Proctor (2016). This paper presents a list of GRS-candidates of size $\geq 4''$, selected from the NVSS catalog using pattern recognition algorithms. The identification of host galaxies and determination of their redshifts, which are necessary for determining the projected linear sizes of radio sources, were not carried out in this work. We made a visual inspection of 370 objects, which is about 23 % of the NVGRC catalog. We used all publicly available radio, optical, and infrared surveys to refine the morphology of radio sources and identify host galaxies. A similar study was conducted by Dabhade et al. (2017), where only those NVGRC objects for which a radio core was identified in the VLASS maps were considered. Unlike that publication, we inspected all NVGRC objects, including those for which a radio core was not detected in the VLASS maps.

In this paper, we adopt the ΛCDM flat cosmology based on the Planck results: $H_0 = 67.4\,\mathrm{km\cdot s^{-1}Mpc^{-1}}$, $\Omega_m = 0.315$ (Planck Collaboration 2020). The spectral index of the radio source α is defined as $\mathrm{S}_\nu \propto \nu^\alpha$.

2. Search for giant radio sources in the NVGRC catalog

The NVGRC catalog (Proctor 2016) is based on the NVSS (Condon et al. 1998) catalog, in which one radio source can be represented by several entries. To identify giant radio sources, Proctor (2016) used the Oblique Classifier One (OC1) software, which implements the decision tree method (Murthy et al. 1994). The OS1 classifiers were tuned to a training set prepared using the properties of 48 GRGs from Lara et al. (2001a). As a result, a list of 1616 GRS candidates was compiled.

Since radio source identification was not performed, the catalog's sources, in addition to actual giants, include radio sources with smaller projected linear sizes, as well as NVGRC objects in which each of the two components is an independent radio source. For this reason, it is necessary to check each candidate for its classification as a giant.

Next, we describe the methodology we used to recognize giants among the objects in the NVGRC catalog.

2.1. Radio and optical identifications of the candidates

Due to the large angular sizes of GRSs, the identification of their hosts is not an easy task. In addition, if the surface brightness of the radio lobes is low, it is difficult to recognize the GRS itself. If the candidate has a radio core that coincides with the optical object, then the identification is beyond doubt and will be reliable. For radio sources whose core is not detected on the VLASS maps, it is first necessary to recognize the radio structure of the source and determine the position of the host. Optical or ultraviolet radiation hidden by dust structures around the accretion disk of the AGN is re-emitted in the mid-IR range. And in this case, it is the mid-IR data that can help in identifying the host. Data from new radio surveys in the low- and high-frequency ranges help in classifying the radio structure.

Dabhade et al. (2020) conducted a massive search for GRS among NVGRC objects with a radio core in the VLASS maps. We conducted similar work, but, unlike the mentioned paper, we considered objects both with and without a radio core. We also additionally examined one-square-degree neighborhoods for the candidates under consideration.

We used the Aladin Sky Atlas (Bonnarel et al. 2000) and TOPCAT (Taylor 2005) applications to work with numerous catalogs and surveys.

To determine the radio structure of NVGRS objects, we used NVSS, VLASS (Gordon et al. 2021) and FIRST (Helfand et al. 2015)as well as surveys TGSS (Intema et al. 2017), GLEAM (Hurley-Walker et al. 2017), WENSS (Rengelink et al. 1997), SUMSS (Mauch et al. 2003), RACS (McConnell et al. 2020), and in some cases surveys GB6 (Gregory et al. 1996) and Apertif (Rottgering et al. 2011; Adams et al. 2022).

Table 1. The difference in the measured LAS of the giants.

List	N, obj.	$\Delta D \pm$ RMS
K18-D20	257	0.05±0.35
O23-K18	19	0.20±0.28
OL-O23	7	0.18±0.21
OL-D20	51	0.29±0.63
OL-K18	24	0.29±0.18

After the determination of the structure of the radio source, we moved on to optical identification using the surveys SDSS (Ahumada et al. 2020), PanSTARRS (Chambers et al. 2016), DES (Abbott et al. 2018), Legacy Surveys (Dey et al. 2018). If the source did not have a core on the VLASS maps, then the images in the WISE (Cutri et al. 2013) bands were also inspected. If two nearby optical objects were suitable for the role of the host galaxy, then the cutouts from UKIDSS (Lawrence et al. 2007; Lucas et al. 2008) were used. The brighter object in the K-band was considered as a more likely candidate. In addition, we checked the proper motion of the candidate using the GAIA catalog (Gaia Collaboration 2018).

We then searched for spectroscopic or photometric redshifts in the Simbad (Wenger et al. 2000), NED (Helou et al. 1995), NOIR DataLab (Olsen et al. 2019), and Vizier (Ochsenbein et al. 2000) databases.

2.2. Measurment of angular sizes of radio sources

For FR II sources, the angular size is usually measured as the distance between hotspots. For FRI sources and hybrid FRI/FRII objects, the angular size is estimated as the distance between the outer edges of the lobes. In the case of sources that have a strongly curved shape, the angular size is measured along the so-called ridge of the source. Proctor (2016) measured the angular size of the source along the outer edges of the lobes at a level of 3σ above the background level for FRI, FRII, and hybrid types. When measuring, we also did not distinguish between sources of FRI and FRII types. The measurements were performed using the Aladin instrument 'distance'. For sources with curved radio lobes, there is always a certain degree of subjectivity in such measurements.

We measured the angular sizes of the radio sources using VLASS and NVSS cutouts. Some sources on the VLASS maps have only a core and do not even have signs of radio lobes. For them we did not measure the VLASS sizes, and there were 29 such GRS sources. Note, that for 93 of the GRS candidates, the projected linear size obtained from the measurements on the VLASS maps turned out to be less than 0.7 Mpc.

We compared the projected sizes of GRSs that are available in Kuzmicz et al. (2018), Dabhade et al. (2020), Oei et al. (2023) and in our sample. We use for comparison the sizes of radio sources measured by the edges of the source using the NVSS maps. The result can be seen in the Table 1. The first column of the table shows catalogs, for which the difference in the measured angular sizes of the giants is calculated. The designations which are used here: D20 — Dabhade et al. (2020), K18 — Kuzmicz et al. (2018), O23 — Oei et al. (2023) and OL — our list. The second column shows the number of sources that matched in the compared lists. The last column shows the mean difference and the root mean square value in Mpc.

The systematic difference of 0.2–0.3 Mpc between our linear size estimates and the values obtained in Kuzmicz et al. (2018)[1], Dabhade et al. (2020)[2] and Oei et al. (2023) is most likely explained by the fact that we measured the distance not by hot spots, but by the edges of the source.

3. Results of a visual inspection of GRS-candidates

Of the 1616 objects in the NVGRC catalog, we examined 370 (23 %) objects within the right ascension range 00^h00^m < R.A. < 05^h20^m. We also inspected radio sources with angular sizes of $2.5'$ and larger, falling into NVSS cutouts with size of one sq. degree centered on the NVGRC object. Some NVGRC objects consist of NVSS components that are physically different radio sources. There are cases when only one component of NVGRC candidate belongs to a radio source classified by us as a GRS. In a number of cases, a GRS not included in the NVGRC was found in the considered NVSS cutouts. Taking into account the aforementioned, 20 GRSs were found that were not included in the NVGRC catalog.

Note that the source J003419.3+011857 in Proctor (2011) is considered as a group of sources, and in Proctor (2016) as a GRS candidate. This object consists of two fairly close radio quasars, as follows from their SDSS DR16 spectroscopic redshifts. The southern source in this pair is classified by Kuzmicz & Jamrozy (2012) as a source whose projected linear size is less than 0.7 Mpc. According to our measurements, and with a redshift higher than what was used in Kuzmicz & Jamrozy (2012), it has size greater than 0.7 Mpc.

Another candidate, J035339.2-011319, was classified as GRG by Dabhade et al. (2020). The radio structure of the northern and southern components of this candidate according to the VLASS maps is more suitable for two double radio sources, and there is definitely an optical identification for the northern component in the PanSTARRS survey. For the southern component, the parent object is a faint optical object in the DECals cutout. We did not consider this source as a giant radio galaxy.

Thus, out of 197 detected GRSs in our sample:

1. 86 GRGs with spectroscopic redshifts. 50 objects are known giant radio galaxies, 36 new GRSs were discovered by us. And six of them are not included in the NVGRC catalog.
2. 72 GRGs with photometric redshifts, 17 objects are included in Dabhade et al. (2020), 55 were discovered by us, and 5 of them are not included in the NVGRC catalog. For 2 of these 5 radio sources, the identification of their hosts turned out to be uncertain due to the complex radio structure. We classified these objects as GRS candidates.
3. Eight GRQs with spectroscopic redshifts. Five are known GRQs, three were discovered by us. And two of them are not included in the NVRSC catalog.
4. Eight quasars with photometric redshifts. They were discovered by us for the first time, and four of them are not included in the NVGSC catalog.
5. 23 parent objects have no redshift information. We consider these objects as candidates.

We could not confidently determine the radio structure of seven NVRGC objects in the catalog J000106.4+340303, J005451.5+564842, J021329.0+292139(2), J025347.1-200007, J032145.1+514855, J035800.3-393629(2), J050341.2-191142. Three NVRGS objects J011352.3+622434, J043503.2+215527, J051219.4+131945 have very weak optical hosts. They are visible only in the PanSTARRS cutouts, but are absent from the PanSTARRS catalog. Their

---

[1] Our measurements of the angular size for NVGRC J005748.3+302114 differ from Kuzmicz et al. (2018). In our opinion, the northern component of the source bends to the south and is more elongated.

[2] There are differences in the angular sizes for the two sources because we used z that is different from Dabhade et al. (2020). For NVGRC J000622.1+263549, we used z_{ph}=0.835 from the DESI survey instead of z_{ph}=0.436. And for NVGRC J042220.9+151101, we used z_{sp}=0.072 from NED instead of z=0.409.

location relative to the radio structure coincides well with the supposed center of the source. Note that hosts J011352.3+622434 and J051219.4+131945 are in the WISE catalog.

Of the 197 GRSs confirmed by us, 72 sources (68 galaxies and five quasars) are already known from Lara et al. (2001a); Schoenmakers et al. (2001); Kuzmicz & Jamrozy (2012); Kuzmicz et al. (2018); Dabhade et al. (2020); Oei et al. (2023). We found 97 new GRSs (86 GRGs and 11 GRQs) and assigned 28 radio sources to GRS candidates with identified hosts.

Of the 370 considered NVGRC objects, J005748.3+302114 and J010001.3+300249 are a single radio source, as well as J022318.0+425939 and J022251.6+425744, J050533.7-285707 and J050540.8-282445, J051601.7+245826 and J051605.7+245833. Objects J024733.6+615632 and J035322.1+355212 are HII regions.

So out of 370 NVGRC objects, 177 (49 %) were classified as GRSs[3]. The rest of the objects either have sizes less than 0.7 Mpc (13 %), or are physically unrelated radio sources (38 %), which were combined into one system by the recognition algorithm.

The area of the sky that we inspected using the NVGRC cutouts is about 370 sq. degrees. The area of the sky in the range of right ascensions from 00^h00^m to 05^h20^m is about 8600 sq. degrees. Of the 197 GRSs that fell within the surveyed areas, 20 sources were missed by the recognition algorithm and were not included in the NVGRC catalog. Based on this, the estimate of the number of objects missed by the algorithm in this area may be ≈430 objects. Thus, the estimate of the recognition algorithm efficiency is about 30 %. Note that the efficiency of the algorithm Proctor (2016), which is determined by Mostert et al. (2024) from the identifications of candidates with the radio core in Dabhade et al. (2020), is 10 %.

4. Types of parent objects

To classify the bright host objects as quasar/galaxy, we used information available in the Simbad, NED, Vizier, SDSS, and LS databases. Note that in the Simbad and NED databases, it is possible that an optical object is classified as both a galaxy and a quasar. Such a dual type assignment may be due to the appearance of new clarifying information in publications. Also, the host object may belong to “changing-look” AGN (Matt et al. 2000; Denney et al. 2014).

If only photometric data were available for an object, we used the following criteria (Glikman et al. 2018, 2022) based on the color indices using photometry from the AllWISE catalog[4], which are used to select quasars: $0.5 < W1 - W2 < 2$; $2 < W2 - W3 < 4.5$; $W3 - W4 > 1.9$, where W1, W2, W3, W4 are 3.4, 4.6, 12, and 22 μ bands of the Wide-field Infrared Survey Explorer (Wright et al. 2010), respectively.

For weakest hosts, we inspected the WISE cutouts, if an object was bright in the W1 and W2 bands, but was not detected in the W3 and W4 bands, then we attributed it to galaxies. Otherwise, i.e. the object was bright in the W3 and W4 bands, we attributed it to quasars.

As a result, we divided the parent objects into galaxies, quasars, and IR-excess galaxies, whose color indices correspond to the color indices of quasars according to WISE photometry, which amounted to 74 %, 11 %, and 15 %, respectively. For comparison, we note that galaxies among the GRG parent objects account for 82 % in Dabhade et al. (2020) and 80 % in Kuzmicz et al. (2018).

5. Redshifts and radio power

Of the 197 studied radio sources, 94 hosts have spectroscopic redshifts, 80 have photometric redshifts, and for 23 there is no information about redshifts.

---

[3] This includes GRS-candidates for which we have obtained a redshift estimate or we are not entirely sure about the host identity.

[4] VizieR On-line Data Catalog: II/328.

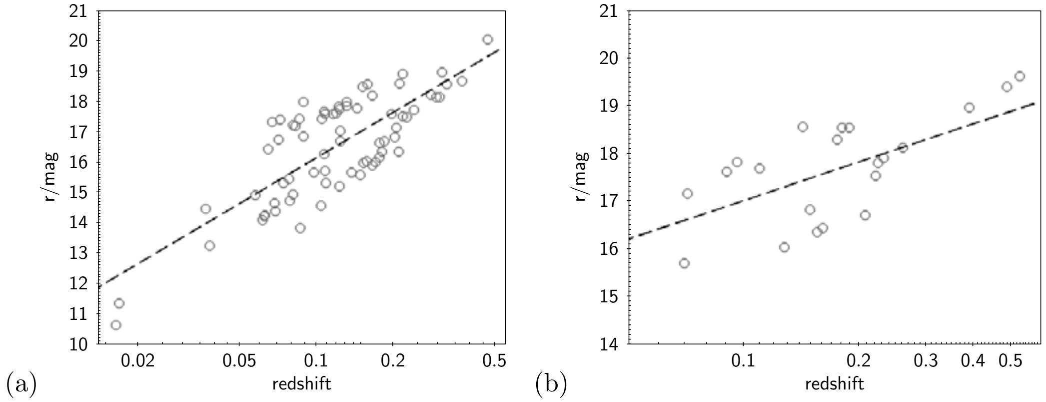

Figure 1. A scatter plot (a) for 71 GRGs with known spectroscopic redshifts and the linear regression (dotted line) between de-reddened apparent r-band magnitudes and spectroscopic redshifts and (b) scatter plot and the regression for 23 GRQs with spectroscopic redshifts. The X-axis is plotted on a logarithmic scale.

5.1. Redshift estimation

Kuzmicz et al. (2018) and Lara et al. (2001b) presented a correlation between the apparent magnitude of GRG hosts and their redshift. This relationship can be used to estimate the “photometric” redshift of galaxies for which redshift data are not available.

Using the r-band apparent magnitude data for GRGs and the spectroscopic redshifts, we constructed a linear regression between these values. The photometric data and spectroscopic redshifts were taken from PanSTARRS, LS and SDSS surveys, NED and SIMBAD databases.

For 71 GRGs the following relationship was obtained (see Fig. 1a):

$$m_r = 5.00 \times \log(z) + 21.16, \tag{1}$$

with a correlation coefficient of $r = 0.78$ and rms = 1.07 mag, where m_r is de-reddened r-band apparent magnitude and z is a spectroscopic redshift.

For GRQ, we constructed a separate dependence. For this, we selected eight quasars and 15 galaxies that can be classified as quasars according to the WISE color indices criterion. The following dependence was obtained (see Fig. 1b):

$$m_r = 2.66 \times \log(z) + 19.69, \tag{2}$$

with a correlation coefficient of $r = 0.72$ and rms = 0.75 mag. These relations were considered for objects with de-reddened magnitudes $m_r < 20.6$. After comparing the spectroscopic redshifts with the values calculated using the obtained formulas, the rms of the difference was about 0.07 for galaxies and 0.15 for quasars.

Using these relationships, we estimated the redshift for 23 parent objects (16 galaxies and 7 quasars), including objects fainter than $m_r = 20.6$. For 94 objects with spectroscopic redshifts, the median value was 0.13; for 80 objects with photometric redshifts — 0.31; for 23 objects with redshift estimates based on the found dependencies, it was 0.63.

5.2. Radio loudness

Relativistic jets, formed as a result of the extraction of the rotational energy of supermassive black holes by a magnetic field and supported by accreting matter, are such effective emitters of radio synchrotron photons that their presence classifies AGNs as members of the class of radio-loud AGN. Now, the classification of AGNs as jetted and non-jetted has become synonymous with the designation of radio-loud and radio-quiet AGNs (Panessa et al. 2019).

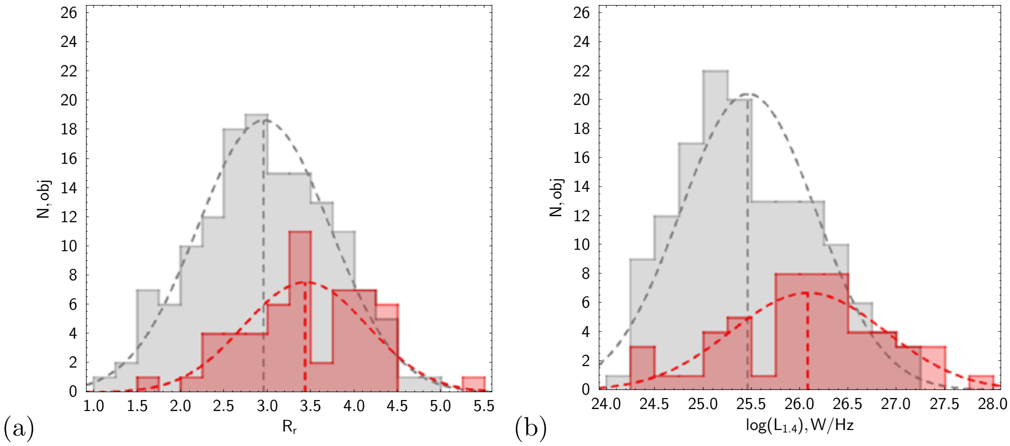

Figure 2. Histograms and their Gaussian fits showing distributions of radio loudness indices (a) and luminosities (b) at 1.4 GHz in W/Hz for galaxies (grey) and quasars and IR-galaxies (red).

To determine radio loudness, we used the approach proposed in the work Ivezic et al. (2002). Here we use the ratio R_r of the radio to optical flux density (without the K-correction) calculated by the formula from Ivezic et al. (2002):

$$R_r = 0.4 \times (m_r - t_N), \tag{3}$$

where m$_r$ is the de-reddened magnitude in the r-band; t_N is the NVSS flux density expressed in the magnitude of the AB-system by the formula:

$$t_N = -2.5 \times \log(F_N/3631\,Jy). \tag{4}$$

Radio sources with $R_r > 1$ are classified as radio-loud AGNs (Kimball & Ivezic 2008). The calculated index values of our list fall within the range from 1.04 to 5.31 (see Fig. 2a), that is, all objects belong to the radio-loud AGNs. The radio loudness index R_r for FRI and FRI/II sources does not exceed 3.5. For FRII sources, it can reach even higher values.

5.3. Radio luminosity

It is known that radio sources can be divided into FRI and FRII depending on morphological type, with the latter being more powerful in the radio band. The radio luminosities of FRI sources at 1.4 GHz lie in the range of 10^{23}–10^{26} W/Hz, of FRII sources — from $10^{24.5}$ W/Hz and higher (Owen & Ledlow 1994). The rest-frame radio power at 1.4 GHz of the sources was estimated using formula from Kuzmicz & Jamrozy (2012):

$$\log L_{1.4} = \log S_{1.4} - (1+\alpha) \times \log(1+z) + 2\log D_l + 17.08, \tag{5}$$

where $S_{1.4}$ is the observed 1.4 GHz flux density (mJy), D_l is the luminosity distance (Mpc), and α is the two-frequency spectral index at 150–1400 MHz, $L_{1.4}$ in W/Hz.

The radio luminosities at 1.4 GHz of the GRSs from our list lie in the range from $10^{24.2}$ to $10^{27.9}$ W/Hz (see Fig. 2b), that is, they all belong to the class of powerful radio sources.

6. Radio morphology

We performed a morphological classification of the giants using cutouts from the NVSS and RACS surveys, as well as cutouts from the FIRST and VLASS surveys with higher angular resolution. Note that the sources under consideration have from 2 to 20 NVSS components.

Table 2. Counts of FRI and FRII sources in redshifts bins

List	z<0.05	0.05÷0.10	0.10÷0.15	0.15÷0.20
D20	4/7	12/29	20/43	6/37
K18	7/5	13/35	10/34	2/32
OL	3/1	13/13	10/26	1/25
mean	52 %	33 %	28 %	9 %

According to the NVSS survey maps, we classified 10 % of the sources as the FRI type, 3 % as the FRI/II type, and 87 % as the FRII type. For Kuzmicz et al. (2018); Dabhade et al. (2020); Andernach et al. (2021), the proportion of FRII sources is 90 %, 89 %, and 93 %, respectively.

We compared the ratio of FRI and FRII sources as a function of redshift for three GRS lists (Dabhade et al. 2020; Kuzmicz et al. 2018; Oei et al. 2023) and our sample. Table 2 presents statistics on the number of FRI, FRI/II, and FRII sources for four redshift intervals. The notations in the list are the same as those in Table 1. In each table cell, the first number indicates the number of FRI and FRI/II sources, and after the slash, the number of FRII sources. The last row of the table shows the average percentage of FRI sources relative to all GRS sources falling in a given redshift interval.

It turns out that at low redshifts ($z < 0.05$) the number of FRI and FRI/II sources can be the same as the number of FRII sources. However, in the redshift interval z=0.15÷0.20, the fraction of FRI sources decreases significantly. Information on the fraction of FRI sources at redshifts $z > 0.2$ is not enough to make estimation. We believe that it is due to the low surface brightness of the outer parts of lobes of FRI sources, GRSs of this type are difficult to detect even at $z > 0.2$. And for this reason, their fraction in the GRS lists is small.

According to VLASS cutouts, we classified 10 % of GRSs as sources with a core-jet/core-lobes morphology, 17 % of the objects as double sources, 57 % of the sources as doubles with a core, and 16 % of the sources as triples[5]. Thus, it turned out that 83 % of the sources on the VLASS cutouts have a radio core, which makes it possible to identify hosts reliably.

Deformation, curvature of the lobes of a radio source is an indicator of its environment and/or processes occurring in the immediate vicinity of the AGN. So, tailed morphology (WAT, Wide-Angle Tailed or NAT, Narrow-Angle Tailed) indicates that the source can be located in clusters or groups of galaxies (Owen & Rudnick 1976; Missaglia et al. 2019). In 22 % of the giants, we noted HT (Head-Tail) features.

A X-, Z-, S-shaped morphology of the radiolobes is explained by a change in the orientation of the jets, either due to the merger of a small galaxy with the massive elliptical host, or due to accretion disk instabilities (Dennett-Thorpe et al. 2002; Liu 2004; Joshi et al. 2019).

Sources that show double-double morphology (Brocksopp et al. 2011) as well as triple morphology (Gopal-Krishna et al. 2012) are classified as AGN with radiophase restart. We combined S-, Z-, X- sources with double-double and triple sources, since their morphological features indicate processes occurring close to the active nucleus. In 26 % of the sources, it is possible to detect such features in the radiolobes.

Some of the GRGs from our sample exhibit a combination of the aforementioned morphological features. Thus, approximately half of the sources exhibited additional features of the morphology of the radio lobes.

Comparing the NVSS and VLASS cutouts, we found that some sources have radio lobes at 1.4 GHz, but they are absent or weakly expressed on 3 GHz maps. In our list of GRSs, such sources turned out to be 38 %.

---

[5] We refer to triple sources as those in which the integrated core flux density can be 10–20 % of the total flux of the source at the NVSS, RACS, or TGSS catalogs.

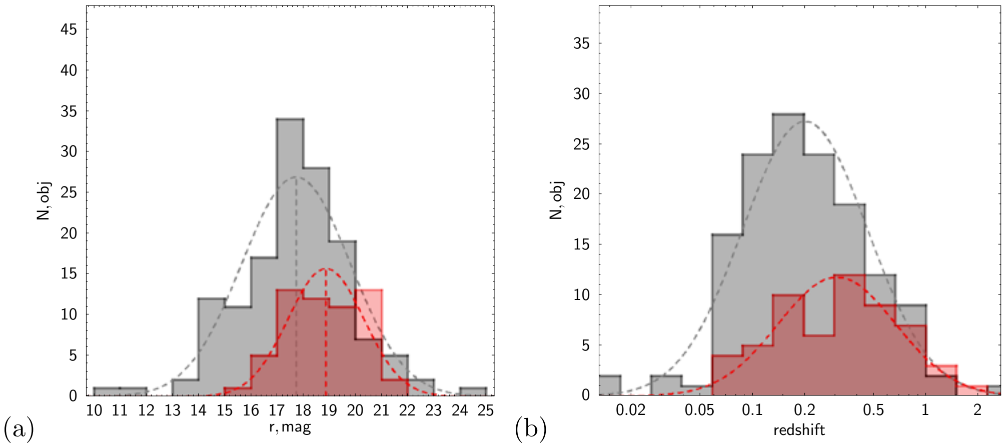

Figure 3. The histograms and their Gaussian fits show the distribution of de-redded magnitudes in the r band (a) and redshifts in logarithmic scale (b) of hosts for 140 GRSs with neighbors (gray) and 57 GRSs without neighbors (red).

If we take into account the occurrence of weakly pronounced lobes on the VLASS maps, then such feature occurs in 13–14 % of quasars and galaxies with an IR excess, and in 40 % of normal galaxies.

7. Environment of giant radio sources

When examining the environment of the GRGs, we considered the presence of optical neighbors and deformation of radio lobes, and also searched for indications of the host belonging to a group or cluster of galaxies in publications. During a detailed visual inspection of the giant hosts' surroundings using cutouts from optical surveys, we noted the presence of neighbors within the distance of approximately 50 kpc, which is between $1''$ and $2'$ depending on the redshift.

We divided the GRSs into groups, ranging from those with no signs of a nearby environment to those with confirmed membership in a group or cluster of galaxies as reported in the publications. No neighbors were found near 36 hosts, and for 21 hosts there is no information about the redshifts of their neighbors. The remaining hosts have neighbors with redshifts matching the hosts' redshifts within the measurement error, and/or the radio source has S-, Z-, or X-shaped morphology, and/or it belongs to a group or cluster of galaxies, and/or the giant has a head-tail morphology. As a result, we found that 140 (71 %) of the objects in our GRS list have close neighbors confirmed by redshift or radio lobe morphology and/or are members of galaxy groups or clusters.

Figure 3 shows the histograms showing the magnitude (a) and redshift (b) distributions for GRSs with neighbors (light grey) and GRSs without neighbors marked with a red line.

The median values of apparent r-band magnitudes and redshifts for host galaxies with confirmed neighbors and host galaxies without neighbors are $18^m.1$ and 0.19, $19^m.3$ and 0.31, respectively. Thus, host galaxies for which we did not find neighbors are fainter and more distant than those for which the neighbors are confirmed. We believe that these differences are partly explained by observational selection. It can be assumed that the number of host galaxies with neighbors may exceed 70 %.

8. Conclusions

We examined objects from the NVGRC catalog in the interval $00^h00^m < R.A. < 05^h20^m$ in order to search for giant radio sources. Of the 370 objects, 48 % were classified as giant radio sources, 14 % had sizes smaller than 0.72 Mpc, and 38 % were independent radio sources combined into one system by the recognition algorithm. When examining NVSS cutouts of one sq. degree, centered on the NVGRC object, 20 giants were detected that are absent from the catalog. Taking this into account, we estimated the efficiency of the recognition algorithm (Proctor 2016) to be approximately 30 %.

Of the 197 GRSs we discovered, 72 sources (68 galaxies and five quasars) are already known in the catalogs Lara et al. (2001a); Schoenmakers et al. (2001); Kuzmicz & Jamrozy (2012); Kuzmicz et al. (2018); Dabhade et al. (2020). We discovered 97 new giants (86 BRKs and 11 quasars) for which spectroscopic or photometric redshifts are known for their hosts. For another 28 GRSs, the redshifts were estimated using the $m_r - z$ relation.

After studying the NVSS cutouts, we classified 87 % of the sources as FRII. It should be noted that the proportion of FRII sources was approximately the same as in Kuzmicz et al. (2018); Dabhade et al. (2020); Andernach et al. (2021) — 90 %, 92 %, and 93 %, respectively. We compared the proportion of FRI giants by selecting sources in four redshift bins. For $z < 0.05$, the proportion of FRI and FRII sources was approximately equal, but already for $z > 0.15$, the proportion of FRI giants sharply decreases. Thus, the predominance of FRII type giants in the GRS lists is most likely associated with observational selection due to the sensitivity limit of existing radio surveys.

According to VLASS maps, 83 % of the sources exhibit core-jet, core-lobe, double-core, or triple morphology. Thus, it turned out that 83 % of the giants have a radio core, which makes it possible to reliably identify hosts.

Comparing the NVSS and VLASS cutouts, we found that 33 % of sources can be classified as “faded”. 25 % of the sources show a restart of the radio source phase. 38 % of the sources have deformed radio lobes.

With the help of parent objects with spectroscopic redshifts, relationships between apparent magnitudes and redshifts were determined, which were used to estimate redshifts for 28 GRSs without redshift data.

When determining the type of the parent object, we mainly used information from the Simbad and NED databases. For those objects for which we did not have this information, we applied the criteria that separate galaxies and quasars according to the WISE photometry. This was mainly used for faint objects. As a result, our GRG sample includes 74 % of galaxies, 15 % of IR-excess galaxies, which, according to the WISE photometric data, can be attributed to quasars, and 11 % of quasars.

When inspecting optical survey maps, we noted close neighbors and the association of host galaxies with groups or clusters of galaxies, taking into account radio morphology and, of course, information from publications. It turned out that close neighbors were found in 140 of the radio sources. Thus, 71 % of GRGs are in a fairly dense environment, and this fraction may be higher.

The area of the sky in the range of right ascensions from 00^h00^m to 05^h20^m is 8600 sq. degrees. Of which, we examined 370 sq. degrees. Of the 197 GRS sources that fell within the examined areas, 20 were missed by the recognition algorithm and are not included in the NVGRC catalog. Based on this, the estimate of the number of objects missed by the algorithm in this area may be ≈ 430 objects. Thus, the estimate of the efficiency of the recognition algorithm is about 30 %.

Acknowledgements This research uses services or data provided by the Astro Data Lab at NSF’s NOIRLab. NOIRLab is operated by the Association of Universities for Research in Astronomy (AURA), Inc. under a cooperative agreement with the National Science Foundation; This research has made use of the NASA/IPAC Extragalactic Database, which is funded by the National Aeronautics and Space Administration and operated by the California Institute of Technology; the CATS database, available on the Special Astrophysical Observatory website.

Funding

The work was carried out within the framework of the state assignment of SAO RAS, approved by the Ministry of Science and Higher Education of the Russian Federation.

References

Abbott T., Abdalla F., Allam S., et al., 2018, Astrophysical Journal Suppl., 239, 2, id. 18
Adams E., Adebahr B., de Blok W., et al., 2022, Astronomy and Astrophysics, 667, id. A38
Ahumada R., Allende P., Almeida A., et al., 2020, Astrophysical Journal Suppl., 249, 1, id. 3
Andernach H., Jimenez-Andrade E., Willis A., 2021, Galaxies, 9, 4, id. 99
Bonnarel F., Fernique P., Bienayme O., et al., 2000, Astronomy and Astrophysics Suppl., 143, p. 33
Brocksopp C., Kaiser C., Schoenmakers A., et al., 2011, Monthly Notices of the Royal Astronomical Society, 410, 1, p. 484
Chambers K.C., Magnier E.A., Metcalfe N., et al., 2016, eprint arXiv:1612.05560
Condon J., Cotton W., Greisen E., et al., 1998, Astronomical Journal, 115, 5, p. 1693
Cutri R., Wright E., Conrow T., et al., 2013, Explanatory Suppl. to the AllWISE DR Products
Dabhade P., Gaikwad M., Bagchi J., et al., 2017, Monthly Notices of the Royal Astronomical Society, 469, 3, p. 2886
Dabhade P., Mahato M., Bagchi J., et al., 2020, Astronomy and Astrophysics, 642, id. A153
Dennett-Thorpe J., Scheuer P., Laing R., et al., 2002, Monthly Notices of the Royal Astronomical Society, 330, 3, p. 609
Denney K., De Rosa G., Croxall K., et al., 2014, Astrophysical Journal, 796, 2, id. 134
Dey A., Schlegel D., Lang D., et al., 2018, Astronomical Journal, 157, 5, id. 168
Enblin T. and Gopal-Krishna, 2001, ASP Conference Series, 250, p. 454
Fanaroff B. and Riley J., 1974, Monthly Notices of the Royal Astronomical Society, 167, p. 31
Gaia Collaboration, Brown A., Vallenari A., et al., 2018, Astronomy and Astrophysics, 616, id.A1
Glikman E., Lacy M., LaMassa S., et al., 2018, Astrophysical Journal, 861, 1, id. 37
Glikman E., Lacy M., LaMassa S., et al., 2022, Astrophysical Journal, 934, 2, id. 119
Gopal-Krishna, Biermann P., Gergely L., et al., 2012, Research in Astronomy and Astrophysics, 12, 2, p. 127
Gordon Y., Boyce M., O'Dea C., et al., 2021, Astrophysical Journal Suppl., 255, 2, id.30
Gregory P., Scott W., Douglas K., et al., 1996, Astrophysical Journal Suppl., 103, p. 427
Hardcastle M., Cheung C., Feain I., et al., 2009, Monthly Notices of the Royal Astronomical Society, 393, 3, p. 1041
Helfand D., White R., Becker R., 2015, Astrophysical Journal, 801, 1, id. 26
Helou G.; Madore B.F.; Schmitz M., et al., 1995, Astrophysics and Space Science Library, 203, p.95
Hurley-Walker N., Callingham J., Hancock P., et al., 2017, Monthly Notices of the Royal Astronomical Society, 464, 1, p. 1146
Intema H., Jagannathan P., Mooley K., et al., 2017, Astronomy and Astrophysics, 598, id. A78
Ivezic Z., Menou K., Knapp G., et al., 2002, Astronomical Journal, 124, 5, p. 2364
Jamrozy M., Konar C., Machalski J., et al., 2008, Monthly Notices of the Royal Astronomical Society, 385, 3, p. 1286
Joshi R., Krishna G., Yang X., et al., 2019, Astrophysical Journal, 887, 2, id. 266
Kaiser C., Dennett-Thorpe J., Alexander P., 1997, Monthly Notices of the Royal Astronomical Society, 292, 3, p. 723
Kapahi V., 1989, Astronomical Journal, 97, p. 1
Kimball A. and Ivezic Z., 2008, Astronomical Journal, 136, 2, p. 684
Komberg B. and Pashchenko I., 2009, Astronomy Reports, 53, 12, p.1086
Kronberg P., 1994, Reports on Progress in Physics, 57, 4, p. 325
Kronberg P., Dufton Q., Li H., et al., 2001, Astrophysical Journal, 560, 1, p. 178
Kronberg P., Colgate S., Li H., et al., 2004, Astrophysical Journal, 604, 2, p. L77
Kuzmicz A. and Jamrozy M., 2012, Monthly Notices of the Royal Astronomical Society, 426, 2, p. 851
Kuzmicz A., Jamrozy M., Bronarska K., et al., 2018, Astrophysical Journal Suppl., 238, 1, id. 9
Lara L., Cotton W., Feretti L., et al., 2001, Astronomy and Astrophysics, 370, p. 409
Lara L., Márquez I., Cotton W., et al., 2001, Astronomy and Astrophysics, 378, p. 826
Lawrence A., Warren S., Almaini O., et al., 2007, Monthly Notices of the Royal Astronomical Society, 379, 4, p. 1599
Liu F., 2004, Monthly Notices of the Royal Astronomical Society, 347, 4, p. 1357
Lucas P., Hoare M., Longmore A., et al., 2008, Monthly Notices of the Royal Astronomical Society, 391, 1, p. 136
Machalski J., Jamrozy M., Zola S., 2001, Astronomy and Astrophysics, 371, p. 445
Machalski J., Jamrozy, M., Zola, S., et al., 2006, Astronomy and Astrophysics, 454, 1, p. 85
Malarecki J., Jones D., Saripalli L., et al., 2015, Monthly Notices of the Royal Astronomical Society, 449, 1, p. 955
Matt G., Guainazzi M., Maiolino R., 2000, Monthly Notice of the Royal Astronomical Society, 342, 2, p. 422
Mauch T., Murphy T., Buttery H., et al., 2003, Monthly Notice of the Royal Astronomical Society, 342, 4, p. 1117
McConnell D., Hale C., Lenc, E., et al., 2020, Publications of the Astronomical Society of Australia, 37, id. E048
Missaglia V., Massaro F., Capetti A., et al., 2019, Astronomy and Astrophysics, 626, id. A8
Mostert R., Oei M., Barkus B., et al., 2024, Astronomy and Astrophysics, 691, id. A185
Murgia M., Fanti C., Fanti R., et al., 1999, Astronomy and Astrophysics, 345, p. 769
Murgia M., 2003, Publications of the Astronomical Society of Australia, 20, 1, p. 19
Murgia M., Parma P., Mack K., 2011, Astronomy and Astrophysics, 526, id. A148
Murthy S., Kasif S., Salzberg S., 1994, arXiv e-prints, cs/9408103
Ochsenbein F., Bauer P., Marcout J., 2000, Astronomy and Astrophysics Suppl., 143, p. 23
Oei M., van Weeren R., Hardcastle M., et al., 2022, Astronomy and Astrophysics, 660, id. A2

Oei M., van Weeren R., Gast A., et al., 2023, Astronomy and Astrophysics, 672, id. A163
Olsen K., Bolton A., Juneau S., et al., 2019, Bulletin of the American Astronomical Society, 51, 7, id. 61
Owen F. and Ledlow M., 1994, ASP Conf. Ser., 54, p. 319
Owen F. and Rudnick L., 1976, Astrophysical Journal Letters, 205, p. L1
Panessa F., Baldi R., Laor A., et al., 2019, Nature Astronomy, 3, p. 387
Parma P., Murgia M., Morganti R., et al., 1999, Astronomy and Astrophysics, 344, p. 7
Peng B., Chen R., Strom R., 2015, Proc. of AASKA14, Online at http://pos.sissa.it/cgi-bin/reader/conf.cgi?confid=215, id.109
Pirya A., Saikia D., Singh M., et al., 2012, Monthly Notices of the Royal Astronomical Society, 426, 1, p. 758
Planck Collaboration, 2020, Astronomy and Astrophysics, 641, id. A6
Proctor D., 2011, Astrophysical Journal Suppl., 194, 2, id. 31
Proctor D., 2016, Astrophysical Journal Suppl., 224, 2, id. 18
Rengelink R., Tang Y., de Bruyn A., et al., 1997, Astronomy and Astrophysics Suppl., 124, p. 259
Rottgering H., Afonso J., Barthel P., et al., 2011, Journal of Astrophysics and Astronomy, 32, 4, p. 557
Safouris V., Subrahmanyan R., Bicknell G., et al., 2009, Monthly Notices of the Royal Astronomical Society, 393, 1, p. 2
Saripalli L., Hunstead R., Subrahmanyan R., et al., 2005, Astronomical Journal, 130, 3, p. 896
Schoenmakers A., de Bruyn A., Rottgering H., et al., 2001, Astronomy and Astrophysics, 374, p. 861
Simonte M., Andernach H., Bruggen M., et al., 2024, Astronomy and Astrophysics, 686, id. A21
Solovyov D. and Verkhodanov O., 2014, Astronomy Reports, 58, 8, p. 506
Solovyov D. and Verkhodanov O., 2014, Astrophysical Bulletin, 69, 2, p. 141
Subrahmanyan R., Saripalli L., Safouris V., et al., 2008, ASP Conf. Ser., 395, p. 380
Taylor M., 2005, ADASS XIV, ASP Conf. Ser, 347, p. 29
van Weeren R., Rottgering H., Bruggen M., et al., 2010, Science, 330, 6002, p. 347
Verkhodanov O., Solovyov D., Ulakhovich O., et al., 2016, Astrophysical Bulletin, 71, 2, p. 139
Wenger M., Ochsenbein F., Egret D., et al., 2000, Astronomy and Astrophysics Suppl., 143, p. 9
Willis A., Strom R., Wilson A., 1974, Nature, 250, 5468, p. 625
Wright E., Eisenhardt P., Mainzer A., et al., 2010, Astronomical Journal, 140, 6, pp. 1868

New radio data for the radio galaxies from the Big Trio program

O. Zhelenkova[1] · **A. Temirova**[2] · **Yu. Parijskij** ·
N. Soboleva

[1] Special Astrophysical Observatory of the Russian Academy of Sciences, Nizhny Arkhyz, 369167 Russia

[2] St. Petersburg Branch of the Special Astrophysical Observatory of the Russian Academy of Sciences, St. Petersburg, 196140 Russia

DOI: 10.26119/2025-moc04
eLocator: moc04
EDN: ovapur

Abstract. The Big Trio program, based on steep and ultra-steep spectrum sources from RATAN-600 Cold Experiment surveys, targeted distant radio galaxies. New multiwavelength surveys enabled indepth analysis of 113 sources to determine their evolutionary status, environmental characteristics, and long-term spectral changes. Analysis revealed that 20 % show signs of initial, fading, or resumed activity. Twenty four sources reside in galaxy groups/clusters or show jet reorientation; four paired sources have parent galaxies just tens of kpc apart. Spectral index analysis ($\alpha \leq -0.9$) showed a declining trend: 90 sources (out of 113) met the criterion in the 365–3940 MHz range (pre-1996 data), dropping to 70 in 340–3000 MHz (modern surveys) and 39 in 76–226 MHz (GLEAM). This decrease stems from instrumental effects (angular resolution differences affecting flux density measurements) and improved low-frequency spectral characterization. For individual sources, spectral index variations may also reflect intrinsic evolutionary processes and source variability.

Keywords: active galaxies: high-redshift radio galaxies; general radio continuum

1. Introduction

Radio galaxies with redshift $z > 2$ and luminosity at 500 MHz $L_{500} > 10^{27}\mathrm{W{\cdot}Hz^{-1}}$ are distinguished as a separate population of high-redshift radio galaxies (HzRG) (Miley & De Breuck 2008).

The components of the HzRG radiation are the emission of dust, stars, and an active nucleus. Studies of the first two components show that HzRGs belong to the most massive stellar systems in the early Universe (Seymour et al. 2007; Bryant et al. 2009; De Breuck et al. 2010) and demonstrate signs of a massive galaxy at the stage of formation (Miley & De Breuck 2008), as well as rapid accretion of matter onto a supermassive black hole (SMBH) (Carilli et al. 1997; Vernet et al. 2001; Nesvadba et al. 2008; Drouart et al. 2012). The powerful submillimeter emission is also directly related to active star formation (Rawlings et al. 2013). The dust torus of the radio galaxy obscures the light from the hot accretion disk and provides more opportunities to study the stellar population of the host galaxy than in the case of the quasar (Hopkins & Beacom 2006; Aird et al. 2010).

There is a reason to believe that the galaxy and the SMBH are formed simultaneously (Magorrian et al. 1998; Haring & Rix 2004; Hopkins et al. 2006). According to the hierarchical model, the most massive star systems form at peaks of dark matter density by merging of large numbers of small galaxies (White & Rees 1978). At z$\gtrsim 2 - 2.5$, galaxy clusters are still in the process of forming, as there is not enough time to virialize. For this reason, they are called protoclusters. Observations show that HzRGs are most often found in fairly dense environments (Stevens et al. 2003; Falder et al. 2010; Stevens et al. 2010; Galametz et al. 2012; Mayo et al. 2012), and protoclusters are likely to be found in their immediate vicinity. Since HzRGs are found at high redshifts, they may mark galaxy clusters at cosmological distances.

Bright radio galaxies at $z > 6$ can be used to study the reionization process in detail (Saxena et al. 2018a). The red-shifted $\lambda = 21\,\mathrm{cm}$ (1.4 GHz) ultra-fine transition line of neutral hydrogen falls within the low-frequency radio range ($\nu < 200\,\mathrm{MHz}$) and can be observed as absorption in the spectra of the radio galaxy at $z > 6$ (Carilli et al. 2002). Such absorption lines can, in principle, be detected by current and next-generation radio telescopes (Saxena 2019).

Blind search for distant radio galaxies is not effective. At high redshifts, identifying the host galaxy and determining its properties requires a large investment of observing time, and is often beyond the reach of most existing instruments.

Tielens et al. (1979) discovered that distant radio sources have steep spectra. It was confirmed in subsequent studies, for example, Kapahi & Kulkarni (1990). Although steep spectra are also observed in pulsars and dying radio galaxies, this criterion is often used in the selection of distant radio galaxy candidates. The effectiveness of this approach was demonstrated by Roettgering et al. (1994, 1997); De Breuck et al. (2000, 2004, 2006); Broderick et al. (2007). Additional criteria are also used — small angular sizes, quite a weak integrated flux density, the absence of candidates in the optical and infrared ranges, as well as the shape of the spectrum — a convex spectrum at low frequencies. Similar criteria were used in Saxena et al. (2018b), where a radio galaxy with $z = 5.72$ was found in their sample, which is currently the most distant radio galaxy.

The Big Trio program. In the SAO RAS, the Big Trio program (Goss et al. 1992b; Parijskij et al. 2000) was launched in the early 1990s aimed at searching for distant radio galaxies and their further study. The selection of objects was made from radio sources discovered in the Cold experiment[1] and included in the RC (RATAN Cold) catalog (Parijskij et al. 1991; Pariiskij et al. 1992).

---

[1] The Cold experiment (Berlin et al. 1981, 1984a,b) consisted of series of long-term surveys of a wide sky strip ($24^h \times 0.7°$) at the declination of microquasar SS 433 ($\delta \approx 5°$) at several frequencies, have been carried out in 1980-1987. The aim of the surveys was the search for cosmic microwave background fluctuations. The deepest flux density limit ($\simeq$2.5 mJy) had been reached at 3.94 GHz.

The main selection criterion was the steepness of the radio spectrum ($\alpha \leq -0.9$). The two-frequency spectral indices of the sources were determined using data from RC (3.94 GHz) and UTRAO (365 MHz) (Douglas et al. 1980), which was one of the early releases of the Texas Sky Survey. Additional criteria were also used – flux density (not brighter than several hundred millijansky at 3.94 GHz), double radio sources of small angular sizes (LAS $< 20''$) (Kopylov et al. 1995).

For the SS (Steep Spectra) sample sources, the radio coordinates were refined, the morphological structure and angular sizes were determined using the observations available in the MIT-GB-VLA archive (Fletcher et al. 1996), and observations were also carried out using the VLA for other sources from the RC catalog (Parijskij et al. 1995). In total, 389 radio maps were obtained for 208 RC sources at a frequency of 1.4 GHz with an angular resolution from $1.5''$ to $4.5''$. Some of the unresolved objects were observed at frequencies of 4.8–14 GHz with a resolution of $0.4''$.

Within the framework of the Big Trio program in 1991–2003, 113 objects were observed with the 6-meter optical telescope BTA. In addition, frames for 22 radio sources with subsecond visibility were obtained using the 2-meter NORDIC telescope (Pursimo et al. 1999). For most sources (94 %) of the SS sample, optical companions were found at a limiting magnitude of $m_R \approx 24.5^m$ (Goss et al. 1992a; Kopylov et al. 1995; Parijskij et al. 1996). Based on BVRI photometry, photometric redshift estimates were made for 48 % of the sample (Verkhodanov et al. 2002a).

Spectroscopic studies of parent objects were carried out using the BTA with the SCORPIO focal reducer (Afanasiev& Moiseev 2005). Spectra were obtained for 71 objects (Dodonov et al. 1999; Afanasiev et al. 2003; Kopylov et al. 2006; Parijskij et al. 2010). 50 % of the hosts were classified as radio galaxies according to the type of optical spectrum (narrow emission lines), and half of them have $z > 1$. A quarter of the hosts were classified as quasars (broad spectral lines), 70 % of which have $z > 1$. No lines were detected in the spectra of the remaining quarter of candidates due to the weak brightness of the objects in optical band.

Among 54 radio sources with measured spectral redshifts, 5 galaxies and 5 quasars with $z > 2$ were discovered, including two sources with $z > 3$ and one with $z > 4$. The last three sources with $z > 3$ have extreme radio luminosities at 500 MHz $L_{500} > 10^{28}\mathrm{W\cdot Hz^{-1}}$. Currently, RC J0311+0507, $z = 4.514$ (Kopylov et al. 2006; Wang et al. 2021), is one of the two most powerful known radio galaxies, along with 8C 1435+635, with a luminosity of $L_{150} > 10^{30}\mathrm{W\cdot Hz^{-1}}$ (Saxena et al. 2018b).

The sample of the Big Trio program has been studied quite well. With the advent of deep sky surveys, it became possible to confirm or refine optical identifications, understand the morphology of the radio source, refine the radio spectra, etc.

The paper adopts the flat ΛCDM cosmology based on Planck's results: $H_0 = 67.4\,\mathrm{km\cdot s^{-1}Mpc^{-1}}$, $\Omega_m = 0.315$ (Planck Collaboration 2020). The spectral index of the radio source α is defined as $S_\nu \propto \nu^\alpha$.

2. Used information resources and software

To study radio sources, we took information from the surveys VLSSr (Lane et al. 2014), TGSS (Intema et al. 2017), GLEAM (Hurley-Walker et al. 2017), VCSS (Polisensky et al. 2016; Peters et al. 2021), TXS (Douglas et al. 1996, 1980), MRC (Large et al. 1991), RACS (Hale et al. 2021; Duchesne et al. 2024), NVSS (Condon et al. 1998), FIRST (Helfand et al. 2015), VLASS (Gordon et al. 2023), RC (Parijskij et al. 1991; Pariiskij et al. 1992), PMN (Wright et al. 1994), GB6 (Gregory et al. 1996), PKS (Wright & Otrupcek 1990).

To clarify the morphological structure of radio sources, in addition to the existing collection of data obtained on the VLA for the Big Trio program (Parijskij et al. 1996), we looked through the radio maps from the GLEAM, TGSS, RACS, FIRST, VLASS surveys, and the NRAO archive.

To work with catalogs and surveys, the Aladin Sky Atlas software (Bonnarel et al. 2000) was used, as well as to work with tables — TOPCAT (Taylor 2005).

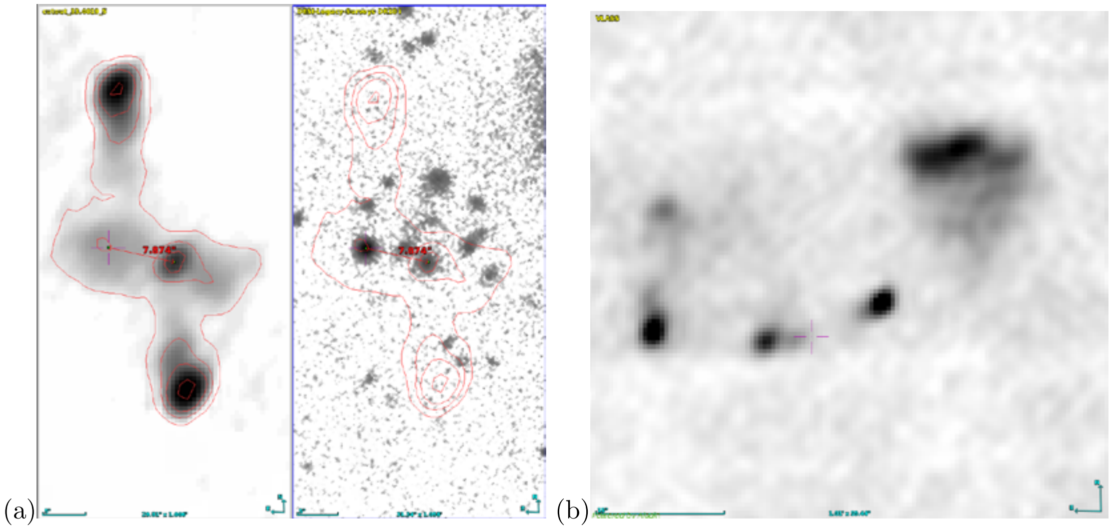

Figure 1. Examples of radio sources: a) X-shaped radio source RC J0213+0516. Near its host galaxy (z_{sp}=0.935) there is a quasar (z_{sp}=0.934) associated with a weak radio source. The distance between the galaxy and the quasar is 7.9″ or 61 kpc; b) RC J0519+0510 is a DDRG-type radio source, which can also be classified as a rare morphological type of HSR sources.

The radio spectra were plotted using the spg program from the FADPS data processing package (Verkhodanov et al. 1993) .

To search for information about the radio sources, we used the SIMBAD (Wenger et al. 2000), VizieR, CATS (Verkhodanov et al. 2005), NED, DataLab (Huang et al. 2020) databases, as well as the optical surveys LS, DES (Abbott et al. 2018, 2021), HSC-SPP (Aihara et al. 2019, 2022), including near- and mid-infrared surveys LAS UKIDSS (Lawrence et al. 2007), GPS UKIDSS (Lucas et al. 2008) and WISE (Cutri et al. 2012; Marocco et al. 2021).

3. Morphological structure of radio sources

Based on the morphological structure of a radio source, it is possible to determine its evolutionary status — young, active, fading, as well as its environment.

For half of SS-sources, there are VLA observations with an angular resolution of $0.1'' \div 2.38''$ (Fletcher et al. 1996; Parijskij et al. 1995), and for the other half, there are maps from the VLASS survey with an angular resolution of 2.5″. For the radio source RC J0311+0507 (4C 04.11), MERLIN and EVN maps with an angular resolution of 0.025″ (Parijskij et al. 2014) were obtained, and for RC J1740+0502, MERLIN maps with an angular resolution of 0.1″.

According to these radio maps, point unresolved radio sources make up 18 % of the sample, with 9 of them being point sources on the VLASS maps and 11 unresolved on maps with an angular resolution of $0.4'' \div 1.6''$. For 44 double sources, the morphology was determined from the VLASS maps, and for 49 — from maps with an angular resolution of $0.025'' \div 2.38''$.

Visual examination of radio maps and cutouts from the DESI, DES, HSC-SSP optical surveys, including the LAS UKIDSS and WISE infrared surveys, revealed that some radio sources are not single but consist of two sources located close to each other in the picture plane.

There were six such sources. Moreover, each of RC J0126+0502, RC J0213+0516, RC J0318+0506, and RC J1251+0446 forms a pair of close radio sources with angular distances between the parent galaxies of about $6'' - 8''$ or about 50–70 kpc.

In the NVSS and TGSS radio surveys, the sources RC J0318+0456 and RC J0324+0442 are double radio sources. Higher angular resolution maps and optical data have shown that each component of the radio sources RC J0318+0456 and RC J0324+0442 are actually independent sources that happen to be in the line of sight.

As an example of a pair of radio sources, we consider RC J0213+0516 (Fig. 1a), where the galaxy SDSS J021336.32+051819.0 is the host of a double X-shaped radio source with the coordinates of the core $\alpha_{2000} = 02^h12^m36.32^s$ and $\delta_{2000} = +05°18'18.8''$. It has a redshift of $z_{\rm sp}$=0.935 (Parijskij et al. 2010). The quasar SDSS J021336.80+051820.7 has $z_{\rm sp}^{\rm SDSS}$=0.934 and is associated with the weak radio source with coordinates $\alpha_{2000} = 02^h13^m36.77^s$ and $\delta_{2000} = +05°18'20.7''$. The angular distance between the hosts is $7.9''$ or 61 kpc.

Among the double radio sources, there are sources that cannot be classified as either FRI or FRII (Fanaroff & Riley 1974). They are classified as FRI/FRII or HyMoRS (HYbrid MOrphology Radio Sources) (Gopal-Krishna & Wiita 2000; Kapinska et al. 2017; Stroe et al. 2022).

Radio galaxies with double lobes DDRG (Double-double Radio Galaxy) (Schoenmakers et al. 2000; Saikia et al. 2006) also do not quite fit into the FRII type. In the SS sample, we classified six radio sources as the hybrid type and three radio sources as the DDRG type. An example of a double-double radio source RC J0519+0510 is shown in Fig. 1b.

37 (27 %) double sources have a core, and for 16 of them the contribution of the core to the total flux density at 3 GHz is less than 5 %, and for 15 sources with a core this contribution can be from 10 % to 60 %. We classified double sources with a core for which the contribution of the core to the total flux density at 3 GHz is more than 10 % as triple sources. In addition, for 6 radio sources, the contribution of the core is more than 35 %, and they can be classified as CDT (Core-Dominated Triple) (Marecki et al. 2006).

There are radio sources with deformed lobes. They are classified into the following types — winged sources WRG (Winged Radio Galaxy)[2] (Cohen et al. 2007; Yang et al. 2019; Bera et al. 2022), “head-tail” radio sources HT (Head-tailed)[3](Rudnick & Owen 1976; Blanton et al. 2000; Missaglia et al. 2019; Sasmal et al. 2022), as well as recently discovered radio sources with a ring-shaped diffuse radio emission — ORC (Odd Radio Circle) (Norris et al. 2021) and HSR (Horseshoe-Shaped Ring) (Kumari & Pal 2024).

In the SS sample, we classified 12 WRGs, 8 WAT sources, and two more sources that are C-shaped or even horseshoe-shaped (HSR). RCJ0519+0510 is shown in Fig. 1b as an example.

The sample included two giant radio galaxies (Willis et al. 1974; Lara et al. 2001; Andernach et al. 2021) — RC J0152+0453 and RC J1333+0451 with projected linear sizes of 990 and 1100 kpc, respectively, as well as twenty-six compact radio sources with sizes from 0.7 to 19 kpc or with an angular size less than $3''$, if the redshift is not known for the host of the unresolved radio source.

4. Analysis of total flux densities and spectral indices

Using a representative set of flux density measurements, we calculated spectral indices for each source in the SS sample. The calculations utilized a linear fit to flux densities across three different datasets, covering the following frequency ranges: 365–3940 MHz (data prior to 1996), 340–3000 MHz (from recent catalogs), and 76–227 MHz (GLEAM survey data). A comparative analysis of the results revealed a systematic decrease in the proportion of sources with spectral indices satisfying the condition $\alpha < -0.9$.

When linearly fitting flux densities, the edge points of the spectral indices can have a significant impact on the resulting indices, especially with a limited number of data points. To address this issue, we conducted a targeted comparison of old and new measurements at frequencies of 365 MHz (TXS) versus 340 MHz (VSSS) and 1400 MHz (NVSS) versus 1368 MHz (RACS). According

---

[2] WRG include X-, S-, Z-shaped radio galaxies (XRG, ZRG).

[3] HT galaxies include WAT (Wide-Angle Tailed), NAT (Narrow-Angle Tailed) and C-shaped radio galaxies.

to established astrophysical concepts, sources with steep spectra typically exhibit greater temporal stability than sources with flat spectra.

To identify sources with significant discrepancies between measurements, we implemented a two-step procedure: first, we calculated the variability index for each source; second, we performed a detailed analysis of sources with variability indices greater than 3. This threshold allows us to select objects with significant discrepancies between the data points. Particular attention was paid to the data at 340 and 365 MHz, as these frequencies are important in determining spectral steepness. Refining the flux densities at these frequencies allows for a more accurate interpretation of the observed decrease in the number of sources with $\alpha < -0.9$. This analysis proves the importance of separating instrumental effects from properties of sources.

4.1. Variability indices

For the vast majority of sources in the sample, there is sufficient data to compare integrated flux densities over two or more epochs. We compared fluxes at 340–365 MHz (VCSS, TXS), 1368–1400 MHz (RACS-mid, NVSS), 3900–3940 MHz (GAISh, Cold), and 4850–5000 MHz (MIT-GB, GB6, PMN, PKS).

The time interval between the observations of the VCSS and TXS surveys is about 40 years, if the average value between the year of the beginning and the end of the survey is taken as the observation epoch. The interval between the average epochs of the RACS-mid and NVSS surveys is 27 years. The interval between the observations of one source in the Zelenchuk-GAISh survey (Amirkhanyan et al. 1985) and the series of Cold surveys can be from 2 to 19 years. In surveys MIT-GB (Bennett et al. 1986), GB6 (Gregory et al. 1996), PMN (Griffith et al. 1995) and PKS (Shimmins et al. 1974; Binette et al. 1981) the interval between observations can be up to 18 years. Note that data for 340–365 MHz are available for 77 % of the sample, for 1368–1400 MHz – 100 %, 3940 MHz – 89 %, 4850 MHz – 82 %.

We calculated several variability indices using a simple variability criterion:
V=$(S_{\max} - S_{\min})/\sqrt{\sigma^2_{\max} + \sigma^2_{\min}} > 3$,
where $S_{\max}$, $\sigma_{\max}$ and $S_{\min}$, $\sigma_{\min}$ are the maximum and minimum flux densities and their measurement errors, respectively. In a such way the variability indices V_{3940} for 3900–3940 MHz and V_{4850} for 4775–5000 MHz have been calculated.

The variability index V_{340} for frequencies of 340 and 365 MHz according to VCSS and TXS data, as well as the index V_{1400} for 1368 and 1400 MHz according to RACS-mid and NVSS data, was determined as follows:
$V_{340} = (S_{340} - S_{365})/\sqrt{\sigma^2_{340} + \sigma^2_{365}}$,
$V_{1400} = (S_{1368} - S_{1400})/\sqrt{\sigma^2_{1368} + \sigma^2_{1400}}$,
since it was interesting to compare where S_{340} is greater than S_{365} and vice versa. For this reason, negative values appeared for V_{340} and V_{1400}.

The variability indices distributions V_{340} and V_{1400}, V_{3940} and V_{4850} are shown in the Fig. 2a, Fig. 2b, respectively. The significant difference between the distributions of the indices V_{340} and V_{1400} turned out to be unexpected, with all 113 radio sources in the sample having a variability index $|V_{340}| < 3$.

Of the 87 sources for which data is available in the VCSS and TXS catalogs, 44 % have $|V_{340}| > 3$. At frequencies of 3900–3940 MHz, of the 101 radio sources, 31 % have $V_{3940} > 3$, and at 4850–5000 MHz, of the 93 objects, 37 % have $V_{4850} > 3$. For 47 radio sources, at least one of V_{3940} and V_{4850} is greater than 3; for 10 radio sources, both indices are greater than 3. And for 4 sources, RC J0934+0505, RC J1142+0455, RC J1456+0456, and RC J2225+0523, all three indices $|V_{340}|$, V_{3940}, and V_{4850} are greater than 3.

Next, we will try to figure out why there is such a difference between the variability index V_{340} and V_{1400}.

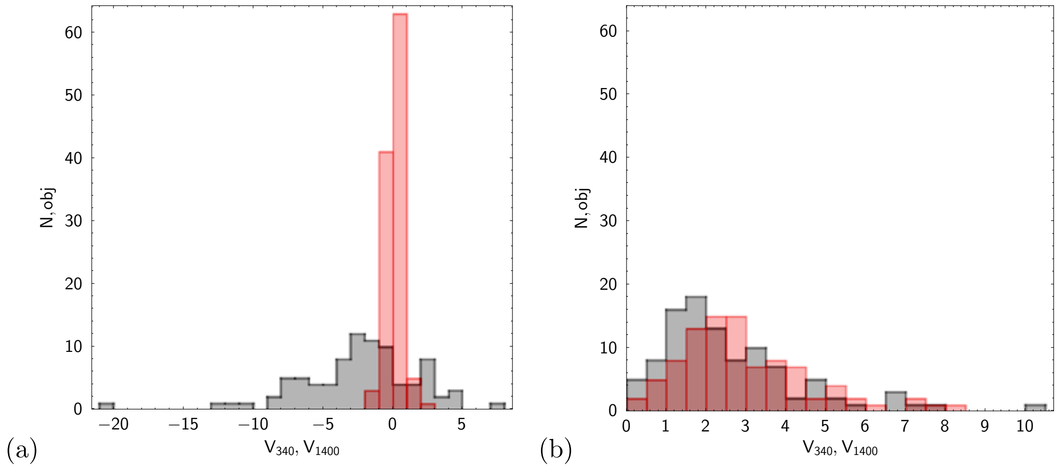

Figure 2. The variability indices distribution: (a) V_{340} (grey) and V_{1400} (red); (b) V_{3940} (grey) and V_{4850} (red).

4.2. Flux density measurement errors

We inspected the vicinity of the radio sources using cutouts from the GLEAM, TGSS, RACS-low, and RACS-mid surveys, which were checked for the presence of the radio sources close to the object under investigation, which could make an additional contribution to the value of S_{365}, as well as other reasons that could affect the value of S_{340}.

4.2.1. Contribution from nearby radio sources

Note that Douglas et al. (1996) indicated that two sources of comparable brightness would be resolved in the TXS catalog if they were separated by $> 9.6'$ in right ascension or by $> 8.1'$ in declenation. Trying to account for the contribution from nearby radio sources to S_{365} for the object under study, we chose a search area of approximately the same size. Using the RACS-low cutouts, we counted the sources that fell into the area, summed up their flux densities, and determined their total fraction relative to the source under study, which was then taken into account in S^c_{365} by subtracting this fraction from the total flux density S_{365}. For 16 out of 87 radio sources, neighboring sources were not detected in the studied regions.

The histogram in Fig. 3a shows the distributions of variability parameters V_{340} (grey) and V^c_{340} (red) for sources with neighbors. The parameter V^c_{340} takes into account the contribution of neighboring sources to the integral flux density S_{365}. The average value of the variability index is $V_{340} = -2.38$; and after correction for the contribution of neighbors, it became $V^c_{340} = -0.56$.

4.2.2. Errors of flux determination for double radio sources

From the sources with VCSS data, we selected double sources with angular sizes $LAS > 15''$, exceeding the angular resolution of the VCSS survey. The LAS angular size (the largest angular size) was measured from the outer VLASS components of the radio source. The sample included 28 double sources with angular sizes in the range of $15'' \div 124''$.

As it turned out, the integral flux density of some sources in the VCSS catalog is not always determined correctly. This is especially true for sources with asymmetric flux density components, according to the maps of the FIRST and VLASS surveys. Such radio sources can be represented in VCSS by a single component, and then the integral flux density S_{340} turns out to be underestimated. Note that only two sources out of 28 double radio sources have two components in the VCSS catalog — RC J0318+0456 ($LAS = 77.7''$) and RC J1148+0455 ($LAS = 40.5''$).

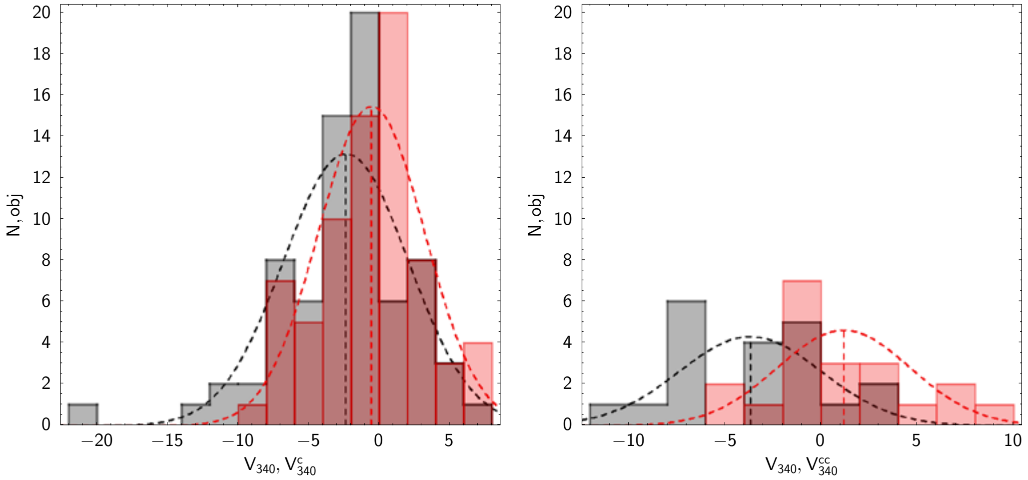

Figure 3. Diagrams showing the distribution of variability indices (a) V_{340} (marked in grey) for sources with neighbors, and V^c_{340} (in red), where the contribution from neighbors is taken into account; (b) for double sources V_{340} (grey) and V^{cc}_{340} (red). The index V^{cc}_{340} takes into account both the underestimated flux S_{340} of double radio sources and the contribution from neighbors. The Gaussian approximation of the quantities is shown by the dashed lines in black and red, respectively.

As a result, for 11 double radio sources with $LAS > 15''$, when correcting the integrated flux density of S_{340} using data from other radio catalogs, the value of S^{cc}_{340} was increased by $7\% \div 50\%$ compared to S_{340}. As a result, their variability indices in absolute value decreased and became less than 3. Figure 3b shows histograms showing the distributions of V_{340} (grey) and V^{cc}_{340} (red) for the double radio sources. When calculating the index V^{cc}_{340}, the contribution from nearby sources to the value of S_{365} was taken into account, as well as the correction of the flux density S_{340} for double radio sources.

The average value of the variability index of double sources was $V_{340} = -3.70$, and after correction of the underestimation of the integral flux densities, it became $V^{cc}_{340} = 1.15$.

Nevertheless, after these corrections, the variability index for double radio sources RC J1031+0443, RC J1142+0455, RC J2029+0456, and RC J2036+0451 remained at the level of $|V^{cc}_{340}| > 3$. We believe that the value of the variability index V_{340} for these double radio sources is overestimated, since we failed to correct the underestimated flux density S_{340}.

There are two possible reasons for the underestimation of the integrated flux density S_{340}. One of them is the peculiarities of the procedure for processing double sources with LAS $> 15''$ in the VCSS survey; the second is the presence of extended low surface brightness emission, which is not recorded in VCSS but can make an additional contribution to the integrated flux density in the GLEAM and TXS surveys.

4.3. Radio sources with $|V^c_{340} > 3|$

If we discard the sources for which the contribution to the flux density S_{365} from nearby sources is taken into account, then 19 sources with $|V^c_{340}| > 3$ remain. The parameters of these sources are presented in Table 1. The type and magnitude of the parent object were determined from the LS survey, the redshift — Parijskij et al. (2010), SDSS, LS.

The Table 1 presents the parameters of three groups of radio sources: 5 sources with a peak in the spectrum in the range 100–500 MHz, 6 sources with $V^c_{340} > 3$ and 9 with $V^c_{340} < -3$. Eight sources in the sample have a peak in the radio spectrum at frequencies of 100–500 MHz. Five of them have VCSS survey data. Four sources have $V^c_{340} < -3$, and one source, RC J0133+0459, has $V^c_{340} < 3$. All five sources have small angular sizes (see Table 1) and are not resolved in the VLASS survey. The parent objects are faint galaxies of 23–25 magnitudes in optical band, except for the quasar RC J1100+0444.

Table 1. Parameters of radio sources with a significant variability index. Name — radio source; V^c_{340}, V_{3940}, V_{4850} — variability indices at 340, 3940 and 4850 MHz; Type — the type of the host: Q — quasar, G — galaxy, EF — empty field; mag$_r$ — the magnitude in the r-filter; LAS — the angular size; Maj — the major axis of the source in VLASS; RType — the type of the radio source: P — point, D — double, T — triple, cdt — triple with dominant core, css — compact radio source with steep spectrum; z — the redshift; mz — "s" — spectroscopic z, "p" — photometric z. A sign "?" indicates an uncertain type definition. Sources marked with "*" are presumably variable in terms of total flux density.

Name	V^c_{340}	V_{3940}	V_{4850}	Type	mag$_r$	LAS, ″	Maj, ″	Rtype	z	mz
Peaked-spectrum radio sources										
1. RC J0133+0459	2.7	0.1	1.7	G?	25.1	0.2	3.3	P		
2. RC J0250+0512	-9.8	2.6	3.9	EF	>25	1.2	2.9	D/css		
3. RC J0907+0439	-5.7	5.0	1.8	G?	24.7	0.3	2.8	P		
4. RC J1100+0444*	-3.1	4.8	1.8	Q	19.1	0.3	2.8	P	0.886	s
5. RC J1150+0459	-4.8	1.7	2.6	G?	23.3	0.3	2.9	P	1.27	s
Radio sources with $V^c_{340} > 3$										
1. RC J0135+0450*	3.5	-	1.5	Q?	18.6	7.8	7.7	T/cdt	0.372	s
2. RC J0143+0505*	4.1	-	4.2	Q	20.8	7.4	7.4	T	2.135	s
3. RC J1456+0456*	7.2	3.5	3.1	Q	20.1	2.2	3.2	P	2.136	s
4. RC J1503+0456*	4.9	1.7	1.2	Q?	22.9	4.5	4.5	T/cdt	0.788	s
5. RC J1551+0458*	3.1	1.0	1.2	G	23.9	11.6	11.5	D	1.29	p
6. RC J1703+0502	4.1	0.8	2.8	G?	23.8	1.8	3.4	D/css	1.23	p
Radio sources with $V^c_{340} < -3$										
1. RC J0034+0513	-6.5	1.5	1.8	G	23.1	12.1	12.2	T?	0.962	s
2. RC J0226+0512*	-7.6	2.6	1.9	Q	20.1	10.7	19.8	D;dd	1.242	s
3. RC J0311+0507	-5.8	1.3	2.9	G	22.9	2.8	17.4	D;mc	4.508	s
4. RC J0355+0449	-4.8	1.4	7.7	G?	24.1	2.4	18.6	D;css	2.7	p
5. RC J0934+0505	-5.2	3.1	7.0	G?	23.0	5.0	17.7	D	1.68	p
6. RC J1011+0502	-4.0	1.6	2.1	G?	23.8	2.8	20.0	D;css		
7. RC J1124+0456*	-7.6	2.7	3.7	G	17.3	11.9	-	D;mc	0.284	s
8. RC J1154+0431*	-3.6	1.2	2.0	Q	19.3	6.7	20.4	D	0.988	s
9. RC J2225+0523*	-3.8	4.9	4.4	Q	17.8	2.7	17.9	T	2.323	s

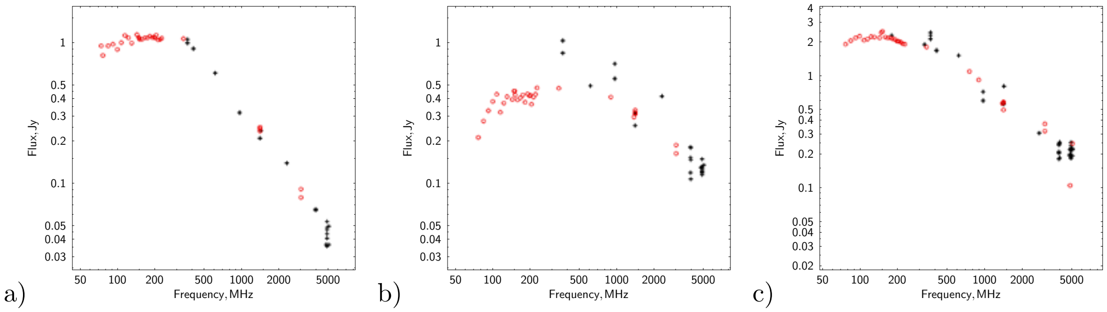

Figure 4. Radio spectra of sources with a spectral peak: (a) RC J0133+0459, (b) RC J0907+0439, (c) RC J1100+0444, constructed using data from Bursov et al. (1996) and new data from GLEAM, VCSS, RACS, VLASS (marked in red).

Orienti & Dallacasa (2021) noted that during the adiabatic expansion of homogeneous synchrotron sources, a shift of the spectral peak towards low frequencies can be observed in the continuum spectrum.

The radio spectra of the MPS sources RC J0133+0459, RC J0250+0512, RC J0907+0439, RC J1100+0444, and RC J1150+0459 are shown in Fig. 4. Of these sources, no spectrum shift is observed for RC J0133+0459 (Fig. 4a), while for RC J0907+0439 such shift is most noticeable (Fig. 4b). The quasar RC J1100+0444 (Fig. 4c) is a variable source that may exhibit a peak in the spectrum during periods of activity.

We suggest that the lower flux density S_{340} compared to S_{365} for these MPS sources, excluding RC J1100+0444, is due to a shift of the spectral peak caused by the radio source expansion, which was noticeable in the TXS and VCSS data over an interval of 34÷48 years between the observing epochs of these surveys.

Nine sources with $V^c_{340} < -3$ (see Table 1) have small angular sizes LAS $< 8''$. Four of them have quasars as their parent objects and are most likely variable objects. The remaining five objects are even smaller in angular size and are presumably young sources and exhibit a shift of spectral maximum to low frequencies in their spectrum, like MPS sources. Together with MPS sources, including those without data in the VSSS, these 13 sources (12 % of the sample) are young.

Thus, the presence of a large proportion of objects with $|V_{340} > 3|$ among the sample sources is explained, first of all, by the difference in the angular resolution of the surveys and the contribution to the integral flux density of S^o_{365} close sources, as well as the underestimated value of S_{340} for some double sources.

Ultimately, we concluded that sources with $|V_{340} > 3|$ may include young, rapidly evolving sources, variable sources, and sources with an extended low-surface-brightness component, likely generated by a previous episode of activity in radio band. For such sources, the extended component may not be detected in the VCSS, but is more likely to be detected in the TXS and GLEAM.

The Table 1 shows 10 sources: RC J0135+0450, RC J0143+0505, RC J0226+0512, RC J1100+0444, RC J1124+0456 (4C+05.50), RC J1154+0431, RC J1456+0456, RC J1503+0456, RC J1551+0458 and RC J2225+0523, which we classified as variables based on the available data. Note that when searching for variable sources in the Cold experiment surveys, RC J0506+0508, RC J1124+0456, RC J1213+0500, RC J1551+0458 were marked as variable radio sources (Majorova & Zhelenkova 2012; Majorova et al. 2015). As a result, 12 radio sources, which is at least 11 % of the sample, exhibit total flux density variability.

5. Spectral indices of sources of the SS-sample

The initial selection of candidates for the sample of sources with steep spectra was made by the two-frequency spectral index $\alpha^{\rm RC}_{\rm UTR} \leq -0.9$ at frequencies of 365 and 3940 MHz using the integral flux densities from the UTRAO and RC (Soboleva et al. 1994) catalogs. And according to the data of this publication, 94 % of the sources in the sample that we study have $\alpha^{\rm RC}_{\rm UTR} \leq -0.9$.

We compared the spectral indices of the SS sample sources obtained from the spectra constructed by approximating data from several sets of integrated flux densities.

We calculated spectral indices for the following data sets:

"old": Spectral index α^{3940}_{365} at 365 and 3940 MHz is determined by a linear approximation of the data from Bursov et al. (1996), which contains the most complete collection of measurements obtained before 1996, as well as from observations performed on RATAN-600 (Parijskij et al. 1991; Pariiskij et al. 1992; Soboleva et al. 1994; Bursov 1996; Bursov et al. 1996; Parijskij et al. 1996; Soboleva et al. 2010; Zhelenkova et al. 2017; Zhelenkova & Majorova et al. 2018);

"new": The spectral index α^{3000}_{340} is determined in the frequency range 340–3000 MHz using linear approximation of VCSS, RACS-low, RACS-mid, NVSS, VLASS data, as well as from Tung

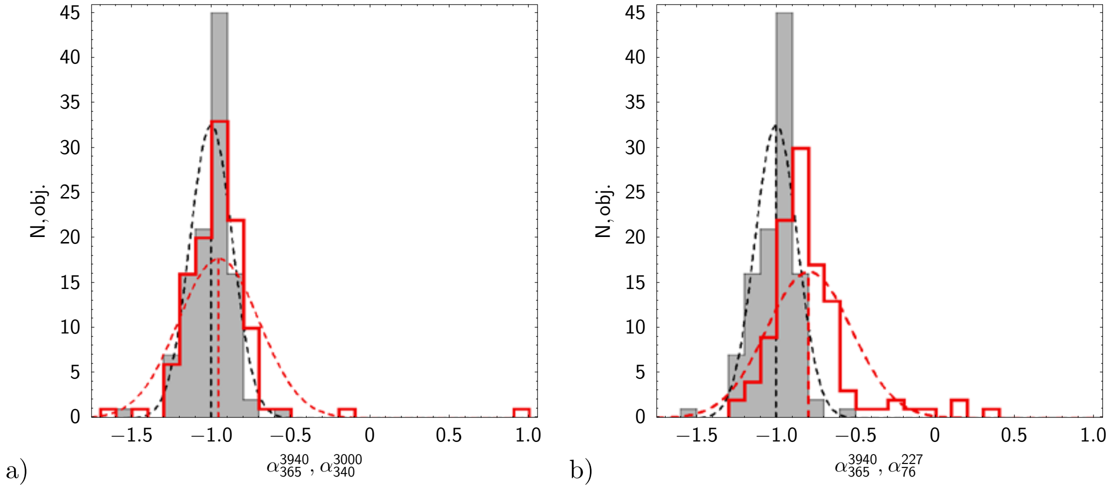

Figure 5. Comparison of spectral indices α_{365}^{3940} calculated using linear approximation of “old” data, α_{340}^{3000} — of “new” data, and α_{74}^{231} — of “glm” data for radio sources of the Big Trio program. Distributions and their approximation by Gaussians for spectral indices: (a) α_{365}^{3940} (grey) and α_{340}^{3000} (red line); (b) distributions of spectral indices α_{365}^{3940} (grey) and α_{76}^{227} (red line).

et al. (2017); de Gasperin et al. (2018); Bruzewski et al. (2021); Gordon et al. (2023). The frequency range is chosen in such a way that it coincides to some extent with the range 365–3940 MHz;

“glm”: α_{76}^{227} is calculated by linearly fitting the GLEAM data;

“all”: Spectral indices α_{74} and α_{7700} are calculated by parabolic approximation of all available flux density data for each source, respectively, at frequencies of 74 and 7700 MHz. The spectral curvature parameter is calculated as $\mathrm{SCP} = \alpha_{74} - \alpha_{7700}$. This parameter is often used to estimate the evolutionary stage of a radio source (Murgia et al. 2011).

We compared the spectral indices of the Big Trio program sources, which were calculated by linearly fitting the data from the “old”, “new”, and “glm” datasets. The histograms (see Fig. 5a) show a comparison of the old and new spectral indices α_{365}^{3940} and α_{340}^{3000}. The index distributions do not differ significantly from each other. When comparing the α_{365}^{3940} with α_{76}^{227} (see Fig. 5b), it is noticeable that α_{76}^{227} indices are shifted toward flatter spectra.

According to the above-mentioned publication Soboleva et al. (1994), 83 out of the 88 sources presented there, which were included in the Big Trio, had $\alpha_{\mathrm{all}} \leq -0.9$ (i.e. 94 %). If we stick to the same frequency range, then for the “old” data set, 90 (80 %) out of 112 sources have $\alpha_{\mathrm{all}} \leq -0.9$, and for the “new” set, 79 (70 %) out of 113 sources have such a spectral index. For the spectral indices determined from the “glm” set, it turns out that 39 sources have $\alpha_{\mathrm{all}} \leq -0.9$, which is 35 % of the sample. The low percentage of steep-spectrum sources whose spectral index was determined from GLEAM data can be explained by the spectrum roll-off at low frequencies due to electron ageing.

Next, we divided the radio sources into two subsamples. Subsample (I) included radio sources that do not have a peak in the spectrum; the curvature of the continuous spectrum, determined by the SCP parameter, lies in the range 0.0–0.5 (Murgia et al. 2011), and the variability index $|V_{340}^{cc} < 3|$. For sources included in this subsample, we believe that the linear approximation of the continuous spectrum will not depend strongly on the different data sets on the basis of which the spectral index is determined. The subsample included 55 sources. The second subsample (II) includes all other sources that were not included in subsample (I).

When comparing subsamples (I) and (II), the discrepancy in the spectral index distributions is particularly noticeable for subsample (II) (see Fig. 6). In subsample (I), the number of sources with $\alpha \leq -0.9$, calculated using spectral indices from the “old” and “new” datasets, remained virtually

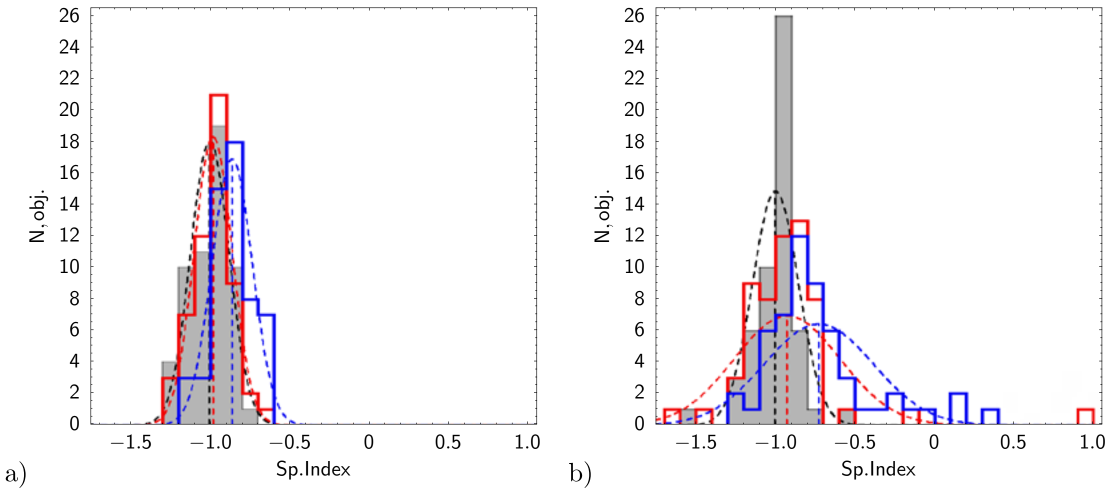

Figure 6. Comparison of the distributions of spectral indices α_{365}^{3940} (marked in grey), α_{340}^{3000} (marked in red), and α_{76}^{227} (marked in blue) and their Gaussian approximations for (a) subsample (I) and (b) subsample (II).

Table 2. Comparison of spectral indices of subsamples (I) and (II). Sp.Ind. — mean and RMS of distribution; Median — median of distribution; SS — number of sources with steep spectra ($\alpha \leq -0.9$)

	Sp.Ind.	Median	SS, obj
(I)	$\alpha_{365}^{3940} = -1.05 \pm 0.10$	-1.03	44
(II)	$\alpha_{365}^{3940} = -1.04 \pm 0.12$	-1.00	46
(I)	$\alpha_{340}^{3000} = -1.03 \pm 0.09$	-1.01	43
(II)	$\alpha_{340}^{3000} = -1.08 \pm 0.15$	-1.06	36
(I)	$\alpha_{76}^{227} = -0.99 \pm 0.06$	-0.96	22
(II)	$\alpha_{76}^{227} = -1.04 \pm 0.09$	-1.03	17

unchanged (see Table 2). However, in subsample (II), the number of such sources decreased from 46 (based on the “old” data) to 36 (based on the “new” data), and the number of sources with $\alpha_{76}^{227} \leq -0.9$ is also lower than in subsample (I).

This can be explained by the fact that subsample (I) includes sources whose jets continue to receive power from the active nucleus. The situation is different in subsample (II). In addition to variable sources, it includes young radio sources, whose jets are in the initial stages of development, and fading sources, whose jets cease receiving power from the active nucleus. Thus, in subsample (II), the change in the continuous spectra – the shift of the entire spectrum to the low-frequency region and the roll-off of the spectrum at low frequencies – should occur more noticeably than in subsample (I).

6. Results

6.1. Morphology

For a well-studied sample of steep-spectrum sources of the Big Trio program, we refined the radio morphology using radio maps with angular resolutions ranging from $0.1''$ to $2.5''$.

Visual inspection of radio maps and cutouts from optical and infrared surveys revealed that some radio sources are not a single radio source, but consist of two sources located close to each other on the observational plane. There were six such objects, with four sources being formed from pairs of close radio sources, which are confirmed by the redshift of the hosts, the distance between which is about 60 kpc.

In addition to the FRII-type radio galaxies, which make up 72 % of the sample, there are 3 % of FRI-type galaxies, 11 % of the hybrid FRI/FRII type, and 18 % of point sources that cannot be resolved on the available radio maps. 27 % of the double sources have a core.

In six radio sources, the contribution of the core is more than 35 % and they can be classified as core-dominated triple radio sources. Three radio sources have double-double lobes. Thus, according to morphological features, 8 % of the sources in the sample show a restart of activity in the radio range.

The deformation of the radio lobes indicates interaction with the environment of the radio source at different distances from the active nucleus. Thus, wing-shaped lobes of the radio source indicate a sharp reorientation of the jet caused by the instability of the accretion disk, possibly caused by interaction with a nearby massive object. Hybrid radio lobes are explained by the inhomogeneity of the environment surrounding the radio galaxy. WATs indicate the presence of the radio source in a group or cluster of galaxies.

In the sample, we classified 12 sources as WRGs, 8 sources as WATs, and 4 sources as horseshoe-shaped and C-shaped. If we add another 8 FRI/FRII sources, then 20 % of the hosts in the sample[4] have neighbors or are located in a group or cluster of galaxies.

The sample includes two giant radio galaxies, as well as twenty-six compact radio sources with sizes from 0.7 to 19 kpc.

6.2. Variability

We compared the integral flux densities of radio sources at frequencies of 340–365 MHz, 1368–1400 MHz, 3900–3940 MHz, and 4850–5000 MHz. Of the 87 sources for which data are available in the VCSS and TXS catalogs, 44 % have variability indices $|V_{340}| > 3$. According to RACS and NVSS data, there are no variable sources in the sample. At frequencies of 3900–3940 MHz, 31 % of 101 radio sources have $V_{3940} > 3$, and at 4850–5000 MHz, 37 % of 93 objects have $V_{4850} > 3$.

We studied the VCSS and TXS data in more detail, since the maximum interval between mean epochs of the surveys is about 40 years. The presence of a large proportion of objects with $|V_{340} > 3|$ among the sources in the sample is explained, first of all, by the difference in the angular resolution of the surveys and, as a result, the contribution to the integrated flux density from nearby sources in S_{365}, as well as, as it turned out, an underestimated value of S_{340} for some double sources.

After the corrections were made, there are still 19 radio sources with $|V_{340} > 3|$. The sources with $|V_{340} > 3|$ may include sources with a peak in the spectrum and compact, rapidly evolving sources whose spectral maximum shifts to the low-frequency region. We assume that a time interval of about 4 decades is sufficient for such an evolution to be noticeable. Such sources turned out to be 11 %.

It is also possible that some sources have extended low surface brightness components that not are detected in the VCSS survey, but most likely detected in TXS and GLEAM. We did not consider this hypothesis in detail here.

Among the sources with the variability index $|V_{340}| > 3$ there may be variable sources. In the studied sample of sources suspected of variability, there were about 10 % of them. These are mainly compact radio quasars.

---

[4] Some radio sources may combine morphological features, for example DD and VAT.

6.3. Continuum spectra

We compared the spectral indices of the Big Trio sample sources obtained from spectra constructed by fitting data from several sets of integral flux densities, namely, data available before 1996 and data from new radio surveys.

Of the 113 sources, 90 sources have a two-frequency spectral index of $\alpha_{3940}^{365} \leq -0.9$, 79 sources have $\alpha_{3000}^{340} \leq -0.9$ according to new surveys VCSS, RACS and VLASS, and 39 sources have $\alpha_{227}^{76} \leq -0.9$ according to GLEAM data. Most likely, this is due to the addition of low-frequency GLEAM data. Although for some radio sources the change in spectrum may be caused by the evolution of the source, expressed in a shift of the peak or roll-off of the spectrum towards lower frequencies, which is noted by measurements of the flux density in various catalogues over an interval of up to forty years.

Acknowledgements The observations were carried out with the RATAN-600 scientific facility. This research has made use of the NASA/IPAC Extragalactic Database (NED), which is operated by the Jet Propulsion Laboratory, California Institute of Technology, under contract with the National Aeronautics and Space Administration; the CATS database available on the Special Astrophysical Observatory website.

References

Abbott T., Abdalla F., Allam S., et al., 2018, Astrophysical Journal Suppl., 239, 2, id. 18
Abbott T., Adamów M., Aguena M., et al., 2021, Astrophysical Journal Suppl., 255, 2, id. 20
Afanasiev V., Dodonov S., Moiseev A., et al., 2003, Astronomy Reports, 47, 5, p. 377
Afanasiev V. and Moiseev A., 2005, Astronomy Letters, 31, 3, p. 194
Aihara H., AlSayyad Y., Ando M., et al., 2019, Publications of the Astronomical Society of Japan, 71, 6, id. 114
Aihara H., AlSayyad Y., Ando M., et al., 2022, Publications of the Astronomical Society of Japan, 74, 2, p. 247
Aird J., Nandra K., Laird E., et al., 2010, Monthly Notices of the Royal Astronomical Society, 401, 4, p. 2531
Amirkhanyan V., Gorshkov A., Kapustkin A., et al., 1985, Soobshch. SAO, 47, p. 5
Andernach H., Jimenez-Andrade E., Willis A., 2021, Galaxies, 9, 4, id. 99
Bennett C., Lawrence C., Burke B., et al., 1986, Astrophysical Journal Suppl., 61, p. 1
Bera S., Sasmal T., Patra D., et al., 2022, Astrophysical Journal Suppl., 260, 1, id. 7
Berlin A., Bulaenko E., Golnev V., et al., 1981, Soviet Astronomy Letters, 7, p. 161
Berlin A., Gassanov L., GolNev V., et al., 1984, Soobshch. Spets. Astrofiz. Obs., 41, 84 pp.
Berlin A., Gassanov L., GolNev V., et al., 1984, Soobshch. Spets. Astrofiz. Obs., 42, 73 pp.
Binette L., Carignan C., Bolton J., et al., 1981, Australian Journal of Physics, 34, p. 407
Blanton E., Gregg M., Helfand D., et al., 2000, Astrophysical Journal, 531, 1, p. 118
Bonnarel F., Fernique P., Bienayme O., et al., 2000, Astronomy and Astrophysics Suppl., 143, p. 33
Broderick J., Bryant J., Hunstead R., et al., 2007, Monthly Notices of the Royal Astronomical Society, 381, 1, p. 341
Bruzewski S., Schinzel F., Taylor G., et al., 2021, Astrophysical Journal, 914, 1, id. 42
Bryant J., Johnston H., Broderick J., et al., 2009, Monthly Notices of the Royal Astronomical Society, 395, 2, p. 1099
Bursov N., Bulletin of the Special Astrophysical Observatory, 40, p. 128
Bursov N., Lipovka N., Soboleva N., et al., 1996, Bulletin of the Special Astrophysical Observatory, 42, p. 5
Carilli C., Rottgering H., van Ojik R., et al., 1997, Astrophysical Journal Suppl., 109, 1, p. 1
Carilli C., Gnedin N., Owen F., 2002, Astrophysical Journal, 577, 1, p. 22
Cohen A., Lane W., Cotton W., et al., 2007, Astronomical Journal, 134, 3, p. 1245
Condon J., Cotton W., Greisen E., et al., 1998, Astronomical Journal, 115, 5, p. 1693
Cutri R., Wright E., Conrow T., et al., 2012, Explanatory Supplement to the WISE All-Sky Data Release Products, p. 1
De Breuck C., van Breugel W., Röttgering H., et al., 2000, Astronomy and Astrophysics Suppl., 143, p. 303
De Breuck C., Hunstead R., Sadler E., et al., 2004, Monthly Notices of the Royal Astronomical Society, 347, 3, p. 837
De Breuck C., Klamer I., Johnston H., et al., 2006, Monthly Notices of the Royal Astronomical Society, 366, 1, p. 58
De Breuck C., Seymour N., Stern D., et al., 2010, Astrophysical Journal, 725, 1, p. 36
de Gasperin F., Intema H. T., Frail D., 2018, Monthly Notices of the Royal Astronomical Society, 474, 4, p. 5008
Dodonov S., Pariiskii Yu., Goss W., et al., 1999, Astronomy Reports, 43, 5, p. 275
Douglas J., Bash F., Torrence G., et al., 1980, University of Texas - Publications in Astronomy, 17, p. 1
Douglas J., Bash F., Bozyan F., et al., 1996, Astronomical Journal, 111, p. 1945

Drouart G., De Breuck C., Vernet J., et al., 2012, Astronomy and Astrophysics, 548, id. A45
Duchesne S., Grundy J., Heald G., et al., 2024, Publications of the Astronomical Society of Australia, 41, id. E003
Falder J., Stevens J., Jarvis M., et al., 2010, Monthly Notices of the Royal Astronomical Society, 405, 1, p. 347
Fanaroff B. and Riley J., 1974, Monthly Notices of the Royal Astronomical Society, 167, p. 31
Fletcher A., Conner S., Crawford F., et al., 1996, Astronomy Reports, 40, 6, p. 759
Galametz A., Stern D., De Breuck C., et al., 2012, Astrophysical Journal, 749, 2, id. 169, p. 12
Gopal-Krishna and Wiita, P., 2000, Astronomy and Astrophysics, 363, p. 507
Gordon Y., Rudnick L., Andernach H., et al., 2023, Astrophysical Journal Suppl., 267, 2, id. 37
Goss W., Parijskij Yu., Soboleva N., et al., 1992, Astronomicheskii Zhurnal, 69, p. 673
Goss W., Pariiskii Y., Soboleva N., et al., 1992, Soviet Astronomy, 36, 4, p. 343
Gregory P., Scott W., Douglas K., et al., 1996, Astrophysical Journal Suppl., 103, p. 427
Griffith M., Wright A., Burke B., et al., 1995, Astrophysical Journal Suppl., 97, p. 347
Hale C., McConnell D., Thomson A., et al., 2021, Publications of the Astronomical Society of Australia, 38, id. E058
Haring N. and Rix H.-W., 2004, Astrophysical Journal, 604, 2, p. L89
Helfand D., White R., Becker R., 2015, Astrophysical Journal, 801, 1, id. 26
Hopkins A. and Beacom J., 2006, Astrophysical Journal,651, 1, p. 142
Hopkins P., Hernquist L., Cox T., et al., 2006, Astrophysical Journal Suppl., 163, 1, p. 50
Huang W., Olsen K., Fitzpatrick M., et al., 2020, ADSS XXVII. ASP Conf. Ser., 522, p. 153
Hurley-Walker N., Callingham J., Hancock P., et al., 2017, Monthly Notices of the Royal Astronomical Society, 464, 1, p. 1146
Intema H., Jagannathan P., Mooley K., et al., 2017, Astronomy and Astrophysics, 598, id. A78
Kapahi V. and Kulkarni V., 1990, Astronomical Journal, 99, p. 1397
Kapinska A., Terentev I., Wong O., et al., 2017, Astronomical Journal,154, 6, id. 253
Kopylov A., Goss V., Pariiskii Yu., et al., 1995, Astronomy Reports, 39, 5, p. 543
Kopylov A., Goss W., Parijskij Yu., et al., 2006, Astronomy Letters, 32, 7, p. 433
Kumari S. and Pal S., 2024, Astronomy and Astrophysics, 683, id. A175
Lane W., Cotton W., van Velzen S., et al., 2014, Monthly Notices of the Royal Astronomical Society, 440, 1, p. 327
Lara L., Cotton W., Feretti L., et al., 2001, Astronomy and Astrophysics, 370, p. 409
Large M., Cram L., Burgess A., 1991, Observatory, 111, p. 72
Lawrence A., Warren S., Almaini O., et al., 2007, Monthly Notices of the Royal Astronomical Society, 379, 4, p. 1599
Lucas P., Hoare M., Longmore A., et al., 2008, Monthly Notices of the Royal Astronomical Society, 391, 1, p. 136
Magorrian J., Tremaine S., Richstone D., 1998, Astronomical Journal, 115, 6, p. 2285
Majorova E., Zhelenkova O., Temirova A., 2015, Astrophysical Bulletin, 70, 1, p. 33
Majorova E. and Zhelenkova O., 2012, Astrophysical Bulletin, 67, 3, p. 318
Marecki A., Thomasson P., Mack K.-H., et al., 2006, Astronomy and Astrophysics, 448, 2, p. 479
Marocco F., Eisenhardt P., Fowler J., et al., 2021, Astrophysical Journal Suppl., 253, 1, id. 8
Mayo J., Vernet J., De Breuck C., et al., 2012, Astronomy and Astrophysics, 539, id. A33
Miley G. and De Breuck C., 2008, Astronomy and Astrophysics Review, 15, 2, p. 67
Missaglia V., Massaro F., Capetti A., et al., 2019, Astronomy and Astrophysics, 626, id. A8
Murgia M., Parma P., Mack K., 2011, Astronomy and Astrophysics, 526, id. A148
Nesvadba N., Lehnert M., De Breuck C., et al., 2008, Astronomy and Astrophysics, 491, 2, p. 407
Norris R., Crawford E., Macgregor P., 2021, Galaxies, 9, 4, id. 83
Orienti M. and Dallacasa D., 2021, Astronomische Nachrichten, 342, 1151, p. 1151
Pariiskij Yu., Bursov N., Lipovka N., et al., 1991, Astronomy and Astrophysics Suppl., 87, p. 1
Pariiskij Yu., Bursov N., Lipovka N., et al., 1992, Astronomy and Astrophysics Suppl., 96, p. 583
Parijskij Yu., Goss W., Kopylov A., et al., 1995, Bulletin of the Special Astrophysical Observatory, 40, p. 5
Parijskij Y., Goss W., Kopylov A., et al., 1996, Bulletin of the Special Astrophysical Observatory, 40, p. 5
Parijskij Yu., Goss W., Kopylov A., et al., 2000, Astronomical and Astrophysical Transactions, 19, 3, p. 297
Parijskij Yu., Kopylov A., Temirova A., et al., 2010, Astronomy Reports, 54, 8, p. 675
Parijskij Yu., Thomasson P., Kopylov A., et al., 2014, Monthly Notices of the Royal Astronomical Society, 439, 3, p. 2314
Peters W., Polisensky E., Brisken W., et al., 2021, American Astronomical Society meeting N237, Bull. of the American Astronomical Society, 53, 1, e-id 2021n1i211p06
Planck Collaboration, 2020, Astronomy and Astrophysics, 641, id. A6
Polisensky E., Lane W., Hyman S., et al., 2016, Astrophysical Journal, 832, 1, id. 60
Pursimo T., Nilsson K., Teerikorpi P., et al., 1999, Astronomy and Astrophysics Suppl., 134, p. 505
Rawlings J., Seymour N., Page M., et al., 2013, Monthly Notices of the Royal Astronomical Society, 429, 1, p. 744
Roettgering H., Lacy M., Miley G., et al., 1994, Astronomy and Astrophysics Suppl., 108, p. 79
Roettgering H., van Ojik R., Miley G., et al., 1997, Astronomy and Astrophysics, 326, p. 505
Rudnick L. and Owen F., 1976, Astrophysical Journal, 203, p. L107
Saikia D., Konar C., Kulkarni V., 2006, Monthly Notices of the Royal Astronomical Society, 366, 4, p. 1391
Sasmal T., Bera S., Pal S., et al., 2022, Astrophysical Journal Suppl., 259, 2, id. 31
Saxena A., Jagannathan P., Röttgering H., et al., 2018, Monthly Notices of the Royal Astronomical Society, 475, 4, p. 5041
Saxena A., Marinello M., Overzier R., et al., 2018, Monthly Notices of the Royal Astronomical Society, 480, 2, p. 2733

Saxena A., 2019, PhD thesis, Leiden University

Schoenmakers A., de Bruyn A., Rottgering H., et al., 2000, Monthly Notices of the Royal Astronomical Society, 315, 2, p. 371

Seymour N., Stern D., De Breuck C., et al., 2007, Astrophysical Journal Suppl., 171, 2, p. 353

Shimmins A., Bolton J., Wall J., 1974, Australian Journal of Physics, Astrophysical Suppl., 34, p. 63

Soboleva N., Pariiskii Yu., Naugolnaya M., 1994, Astronomicheskii Zhurnal, 71, p. 684

Soboleva N., Majorova E., Zhelenkova O., et al., 2010, Astrophysical Bulletin, 65, 1, p. 42

Stevens J., Ivison R., Dunlop J., et al., 2003, Nature, 425, 6955, p. 264

Stevens J., Jarvis M., Coppin K., et al., 2010, Monthly Notices of the Royal Astronomical Society, 405, 4, p. 2623

Stroe A, Catlett V., Harwood J., et al., 2022, Astrophysical Journal, 941, 2, id. 136

Taylor M., 2005, ADASS XIV, ASP Conf. Ser, 347, p. 29

Tielens A., Miley G., Willis A., 1979, Astronomy and Astrophysics Suppl., 35, p. 153

Tung A., Kothes R., Landecker T., et al., 2017, Astronomical Journal, 154, 4, id. 156

Verkhodanov O., Erukhimov B., Monosov M., et al., 1993, Bulletin of the Special Astrophysical Observatory, 36, p. 132

Verkhodanov O., Kopylov A., Zhelenkova O., et al., 2002, Proc. of IAU Symposium 199, p. 247

Verkhodanov O. V., Trushkin S. A., Andernach H., et al., 2005, Bulletin of Special Astrophysical observatory, 58, p. 118

Vernet J., Fosbury R., Villar-Martín M., et al., 2001, Astronomy and Astrophysics, 366, p. 7

Wang W., Wylezalek D., De Breuck C., et al., 2021, Astronomy and Astrophysics, 654, id. A88

Wenger M., Ochsenbein F., Egret D., et al., 2000, Astronomy and Astrophysics Suppl., 143, p. 9

White S. and Rees M., 1978, Monthly Notices of the Royal Astronomical Society, 183, p. 341

Willis A., Strom R., Wilson A., 1974, Nature, 250, 5468, p. 625

Wright A. and Otrupcek R., 1990, PKS Catalog

Wright A., Griffith M., Burke B., 1994, Astrophysical Journal Suppl., 91, p. 111

Yang X., Joshi R., Gopal-Krishna, et al., 2019, Astrophysical Journal Suppl., 245, 1, id. 17

Zhelenkova O., Soboleva N., Temirova A., et al., 2017, Astrophysical Bulletin, 72, 2, p. 150

Zhelenkova O. and Majorova E., 2018, Astrophysical Bulletin, 73, 2, p. 142

Proton jets as sources of high-energy neutrinos and variable radio emission based on the RATAN-600 and CATS data at 0.01–1000 GHz

Yu. A. Kovalev[1,2] · N. Nizhelsky[3] · Yu. Yu. Kovalev[4] · Yu. Sotnikova[3,2] · S. Troitsky[2] · S. Pustilnik[3] · A. Popkov[5,1] · A. Plavin[6] · P. Tsybulev[3,2] · A. Erkenov[3] · G. Zhekanis[3] · A. Kudryashova[3] · N. Bursov[3]

[1] Lebedev Physical Institute of the Russian Academy of Sciences, Moscow, Russia
[2] Institute for Nuclear Research of the Russian Academy of Sciences, Moscow, Russia
[3] Special Astrophysical Observatory of the Russian Academy of Sciences, Nizhny Arkhyz, 369167 Russia
[4] Max-Planck-Institute fur RadioAstronomy, Bonn, Germany
[5] Moscow Institute of Physics and Technology, Dolgoprudny, Russia
[6] Harvard University, Cambridge, USA

DOI: 10.26119/2025-moc05
eLocator: moc05
EDN: xlnmac

Abstract. Monitoring observations and model analysis of instantaneous 1–22 GHz radio spectra of various samples of blazars with strong VLBI (very-long-baseline interferometry) components obtained at RATAN-600 since 1979 and supplemented outside this range with data from the CATS database are continued. The Hedgehog model of a relativistic jet in a strong quasi-radial magnetic field proposed in 1969 by N.S. Kardashev and successfully applied to interpret variable emission spectra of active galactic nuclei is used. The objective of this work is to study the structure and physical parameters of the SMBH neighborhood, as well as a possible proton source of high-energy neutrinos, using spectral methods. We have estimated the magnetic fields, brightness temperatures, angle sizes and other physical parameters for proton jets from spectra fitting.

Keywords: active galaxies: quasars; general radio continuum

1. Introduction

Oleg Verkhodanov was the main initiator and first author of the CATS Database of the SAO RAS (Verkhodanov et al. 2005). He was very proud of the demand for this database throughout the world. Now, we also start using it widely because it gives new important possibilities to study the spectra and structure in 0.01–1000 GHz range (in addition to Mingaliev et al. 1978; Kovalev & Pustilnik 1979; Berlin et al. 1983; Kovalev 1997; Kovalev et al. 1999; Kovalev & Mikhailutsa 1980; Kovalev et al. 2000, 2020; Sotnikova et al. 2022; Kovalev et al. 2022; Vlasyuk et al. 2024): 1) to improve modeling of the spectra and estimate the main physical parameters of galaxies and quasars, 2) to use the new "neutrino channel" better. Some new results can be found here (see Fig. 1–5 and the figure captions).

2. The Hedgehog model and Observations — a short history

The first RATAN-600 observations of the several extragalactic variable sources were conducted in 1977–1978 by M. Mingaliev, L. Pustilnik, S. Trushkin and two colleagues from the Armenia (Mingaliev et al. 1978). The presented regular monitoring at the radio telescope RATAN-600 was started in 1979 by the astrophysical department (headed by I.S. Shklovsky) of the Space Research Institute of the USSR Academy of Sciences (IKI AN USSR) together with the Special Astrophysical Observatory in order to study the variability of the radio spectra of quasars and galaxies. The department was transformed into the Astro Space Center of the Lebedev Physical Institute in 1990 (ASC FIAN, headed by N.S. Kardashev up to 2020).

In 1978, N.S. Kardashev has suggested to one of the authors to submit an observational Proposal to the Program Committee of the RATAN-600 to perform this task (at that time it was believed that the "Hedgehog" model (Kovalev & Mikhailutsa 1980; Kovalev et al. 2000, 2020) of variable sources could be relatively quickly tested with the help of these observations; the model was popular within certain circles of IKI (I.S. Shklovsky, N.S. Kardashev, G.B. Sholomitsky et al. — at Shklovsky's department), FIAN (LPI, L.M. Ozernoy), GAISH (the Sternberg Astronomical Institute, V.N. Kurilchik) and of some students). The first set of spectra measurements was carried out on May 1–22, 1979 for 5 calibrators and **6** well-known variable sources (BL Lac, OJ 287, 3C 279, 3C 345, 3C 454.3 and PKS 1510-089). In September of that year, the first results of 20-day observations — results for BL Lac at 4 wavelengths from 2.1 to 13 cm — were reported at the USSR radio astronomy conference and published by Kovalev and Pustilnik (Kovalev & Pustilnik 1979). The data were sufficient to disprove the belief of sceptics (V.I. Slysh) that it is impossible to obtain reliable results on variability by using an antenna with variable surface like the RATAN-600. The observations were continued due to the constant support of Yu.N. Parijskij. 11 studied objects and 6 calibrators were monitored in 11 sets of the first 3 years (Kovalev & Pustilnik 1979; Berlin et al. 1983). In the middle of the period under discussion, the number of monitored sources increased up to 115, to 1996 — up to 200, in 1997 — up to 600 (Berlin et al. 1983; Kovalev 1997).

3. Summary

1. The structure of average variable spectra for 11 objects in the range of 0.01–1000 GHz remains the same (as at 1–22 GHz) — it consists of two components: quasi-stationary low-frequency component (LFC) and variable high-frequency component (HFC). In some cases, a new HFC may appear (at frequencies above 100 GHz), which would be worth checking in the future.
2. The strong variability can be generated by the jets with relativistic protons in the strong magnetic fields by synchrotron mechanism, and the high energy part of these proton distribution may take part in the generation of high-energy neutrinos.

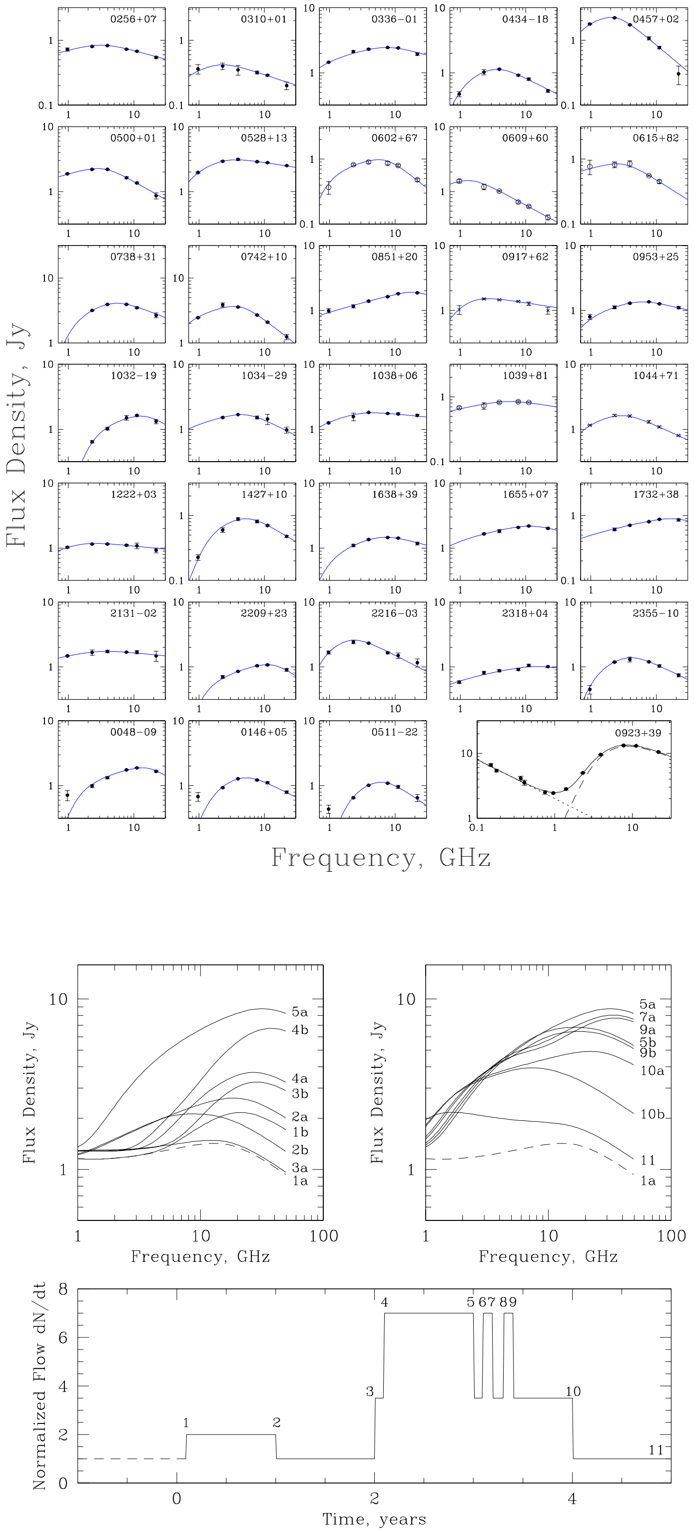

Figure 1. Top (Kovalev et al. 2000): The Hedgehog jet model spectra fitting of the RATAN-600 instantaneous 1–22 GHz spectra. The additional low-frequency data for 0923+39 are from the CATS data base. Bottom (Kovalev et al. 2000): the Hedgehog model variability of the flux density as a result of changing the jet particle flux dN/dt in the time near the jet input.

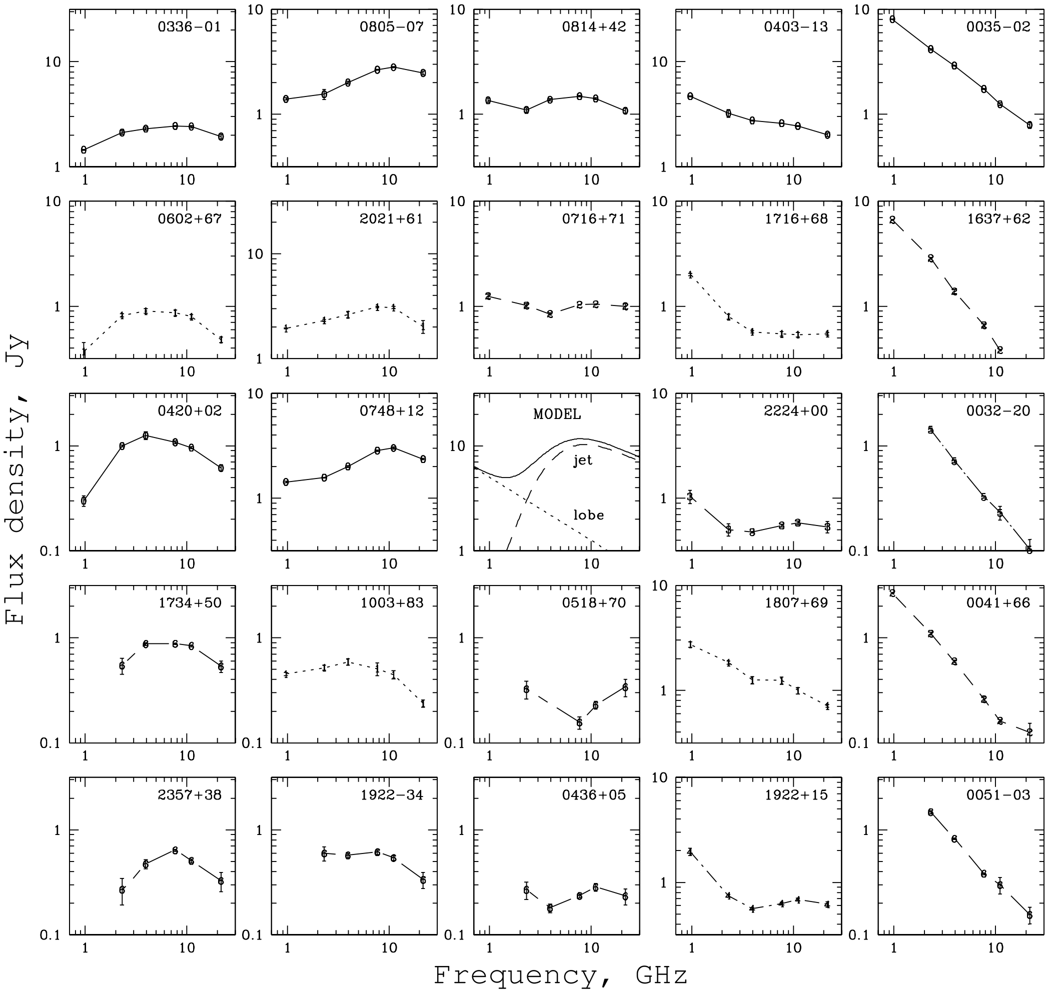

Figure 2. Two-Component spectra (a Low Frequency, LFC, plus a High Frequency, HFC, components): the contribution of the LFC to the spectra of the sources increases from the left to the right columns. The figure in the center: LFC (lobe) plus HFC (jet) give a sum spectrum observed (Kovalev & Pustilnik 1979; Berlin et al. 1983; Kovalev 1997; Kovalev et al. 1999; Kovalev & Mikhailutsa 1980; Kovalev et al. 2000). The HFC is generated by the jet. The LFC is generated by other parts of the source.

Acknowledgements The observations were carried out with the RATAN-600 scientific facility. This research has made use of the CATS database, available on the SAO website. Many of our colleagues from Kovalev (1997), including Oleg, participated in these observations and worked at SAO and RATAN-600 in previous years to ensure that the results we discussed were obtained. We are also grateful to an anonymous reviewer for the valuable comments.

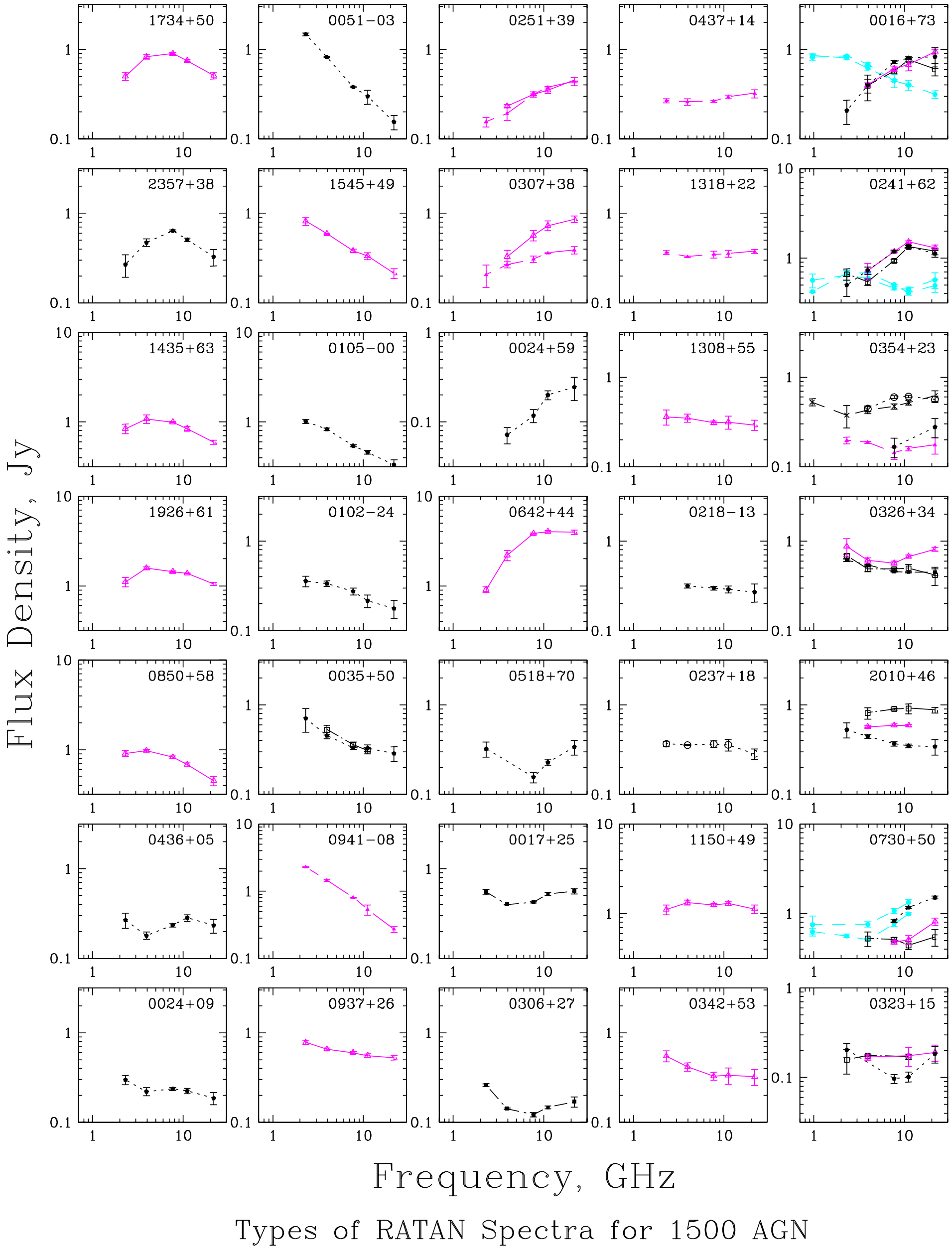

Figure 3. 5 main types of the RATAN-600 instantaneous 1–22 GHz spectra (the columns from left to right): 1) with a maximum, 2) falling and 3) rising towards higher frequencies, 4) super-flat (if the spectral index is changed by less than 0.1 for 3 or more frequencies), 5) variable (between 2, 3 or 4 previous types). Other spectral types may occur in less than 5% of observed spectra (Kovalev et al. 2020).

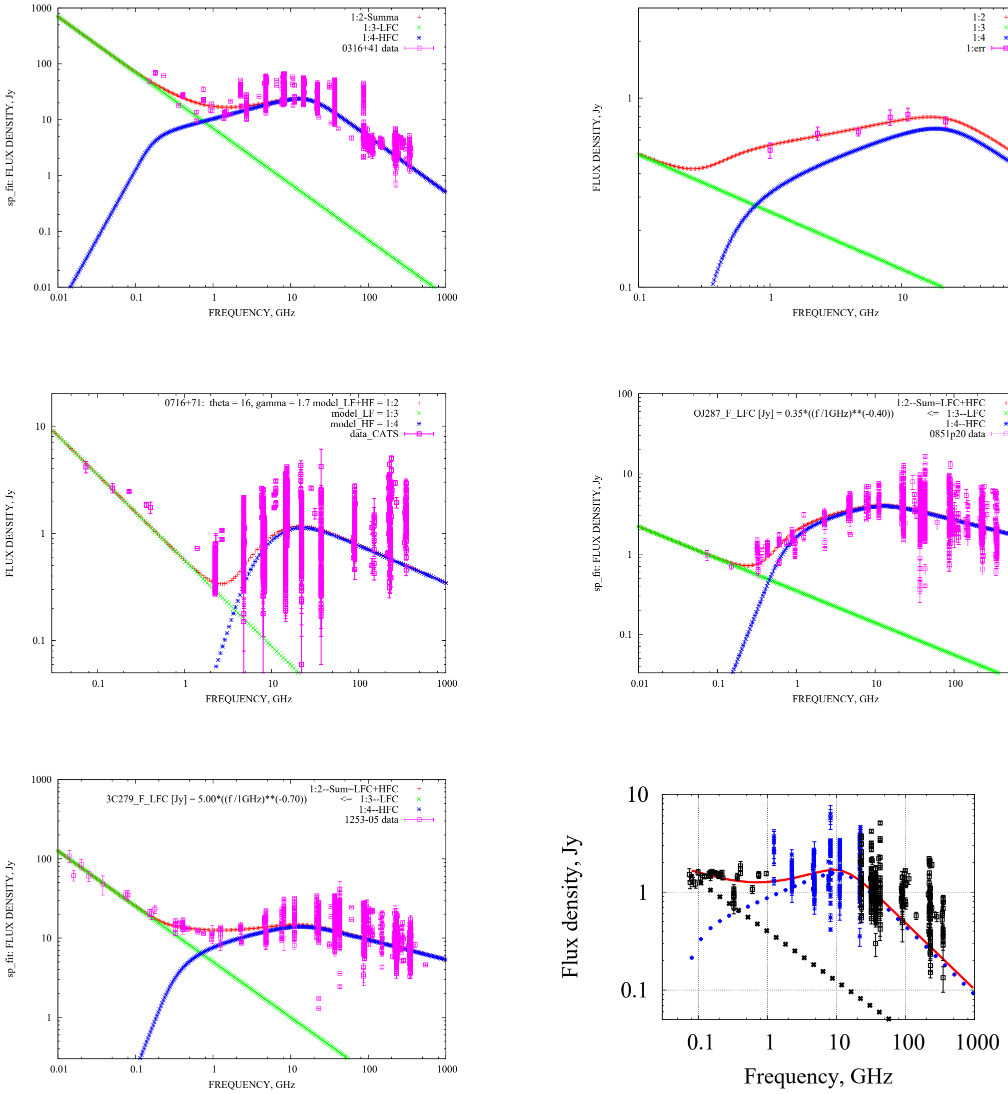

Figure 4. The flux density (in Jy) versus the frequency, (0.01–1000) GHz. Two-component variability of spectra for 11 following blasars: 1st column on the left — 3C84, B0716+71, 3C279; 2nd column – B0506+056, OJ287, B1510−08. Average high-frequency components are the proton jets spectra in the Hedgehog model (see details in Kovalev et al. 1999; Kovalev & Mikhailutsa 1980; Kovalev et al. 2000, 2020; Sotnikova et al. 2022; Kovalev et al. 2022; Vlasyuk et al. 2024). The estimated physical parameters of proton jets for these 6 objects and B1616+045, 3C454.3, B0954+65, B0235+16, B1159+29 are as follows: magnetic field $B \sim (10^3–10^4)$ G, brightness temperatures $T_b \sim 10^{13}–10^{14}$ K, angular sizes $\Theta \sim (0.03–0.003)$ mas. Several objects may have an additional component at frequencies above 100 GHz. If we neglect losses, the Faraday acceleration mechanism allows protons to accelerate in the vicinity of a supermassive black hole to energies of $Ep \sim \Delta B * R * e/2 => 10^{21}$ eV (at $\Delta B \sim 10^4$ G, $R \sim 10^{15}$ cm). Then the neutrino energy is $E_\nu \sim E_p/20$ (see Kovalev et al. 2022; Troitsky 2024). The observational data from RATAN-600 in the frequency range 1–22 GHz for the period from 1997 to 2025 were used. The CATS data (Verkhodanov et al. 2005) contain all data outside this frequency range. The label “sp-fit” to some windows is the name of the program for fitting model spectra.

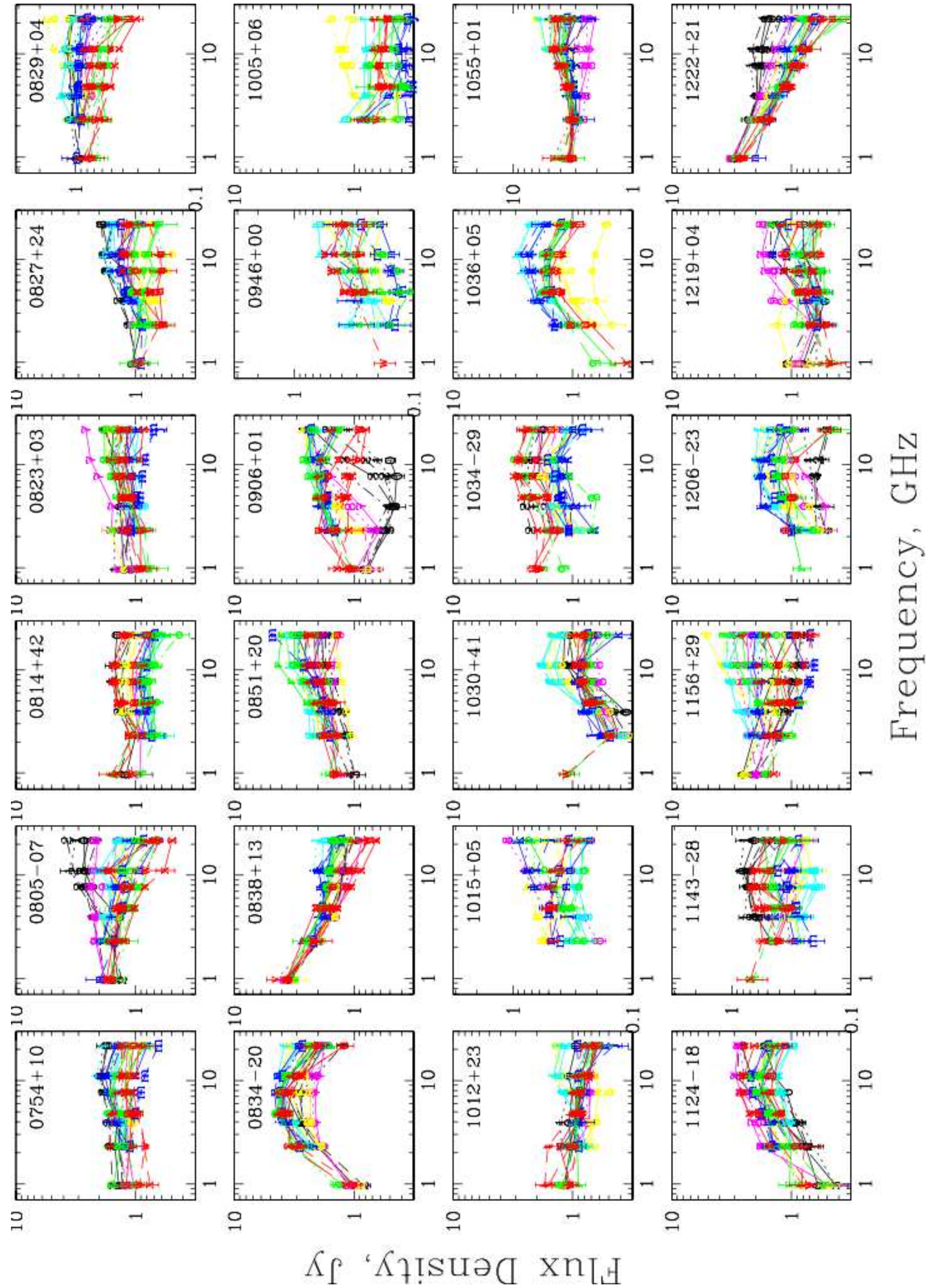

Figure 5. An example of 24 out of 144 AGNs with the strong variability of RATAN-600 1–22 GHz spectra in 1997–2008. It can be expected that such variability is generated also by proton jets. We plan to test this hypothesis similarly to Fig. 4.

References

Berlin A., Kovalev Yu., Nizhelsky N., et al., 1983, Galactic and Extragalactic radio Astronomy, Kharkkov, Publ. IRE Ukr. SSR, p. 56

Kovalev Yu. and Pustilnik S., 1979, XII All-Union Conf.on Galactic and Extragal. Radio Astronomy, Moscow: IKI RAS, p. 31

Kovalev Yu., 1997, Bull. of Spec. Astrophys. Obs., 44, p. 50

Kovalev Yu.A. and Mikhailutsa V.P., 1980, Soviet Astronomy, 24, p. 400

Kovalev Y.Y., Nizhelsky N., Kovalev Y.A., et al., 1999, Astron. Astrophys, Suppl., 139, p. 545

Kovalev Yu.A., Kovalev Y.Y., Nizhelsky N.A., 2000, Publ. Astron. Soc. Japan, 52, p. 1027

Kovalev Yu.A., Kardashev N.S., Kovalev Y.Y., et al., 2020, AdSpR, 65, 2, p. 745

Kovalev Yu.A., Nizhelsky N.A., Kovalev Y.Y., et al., 2022, PoS 425, The Multifaceted Universe: Theory and Observations - 2022, 23-27 May 2022, id. 027

Mingaliev M., Pustilnik S., Trushkin S., et al., 1978, Astrophysics, 14, 1, p. 53

Sotnikova Y.V., Kovalev Yu.A., Kovalev Y.Y., et al., 2022, PoS 399, “European VLBI Network Mini-Symposium and Users” Meeting 2021, 12-14 July 2021, id. 009

Troitsky S., 2024, Physics-Uspekhi, 67, 04, p. 349

Verkhodanov O., Trushkin S., Andernach H., et al., 2005, Data Science Journal, 8, p. 34

Vlasyuk V., Sotnikova Y., Volvach A., et al., 2024, MNRAS, 535, p. 2775

Methodology and the System of automated processing of the RATAN-600 multi-frequency 1–22 GHz observations

Yu.A. Kovalev[1,2] · **V. Amirkhanyan**[3] · **Yu.Yu. Kovalev**[4]

[1] Lebedev Physical Institute of the Russian Academy of Sciences, Moscow, Russia
[2] Institute for Nuclear Research of the Russian Academy of Sciences, Moscow, Russia
[3] Special Astrophysical Observatory of the Russian Academy of Sciences, Nizhny Arkhyz, 369167 Russia
[4] Max-Plank-Institute fur RadioAstronomie, Bonn, Germany

DOI: 10.26119/2025-moc06 EDN: qndjxx
eLocator: moc06

Abstract. The data processing and analysis are carried out at the Astro Space Center of the Lebedev Physical Institute using the YURZUF software package developed and periodically updated by the authors since 1990. The useful signal is separated from the noise by matching the model and observed responses, which is equivalent to the optimal signal filtering mode. For the model response, the RATAN-600 beam is calculated (taking into account real aberrations caused by the transverse displacement of the input feeds from the antenna focus). To reduce errors in the machine inversion of the matrix when approximating the observed response, the well-known SVD program is used. Based on observations of 10–15 known generally accepted secondary calibration sources, the amplitude response of a highly stable noise signal generator (NS) at each wavelength is calibrated in spectral flux density units (in Jansky units) depending on the source height. If necessary, corrections are introduced for the angular sizes and polarization of the calibrators. The core software of the YURZUF multifrequency processing package is described.

Keywords: software; active galaxies: quasars; general radio continuum

1. Introduction

Oleg Verkhodanov and the RATAN-600 Data Processing: Oleg was the first to create a publicly available automated program for step-by-step processing of the RATAN-600 data from the feed cabin No.1 to obtain instantaneous multi-frequency spectra of radio emission for sources in the range of 1–22 GHz — during several years of his working at the radio telescope after graduating from the Leningrad University. This his work, as well as the automation of processing sky survey by the SAI-group, "spurred" also the development of automated processing our joint observations with the SAO at the RATAN-600 in the same years, the results of which are used up to today, and the main software packages are discussed here.

2. Methodology of observations and data processing

The method of obtaining and processing data for many years since the 1990s, in the main, has practically not changed, despite the obvious progress in the operational technology and the modernization of receiver and processing complexes. Due to the horizontal arrangement of the input horns and observations along the meridian with a fixed antenna, practically instantaneous radio spectra are measured in the range from 1 to 22 GHz — by a standard high-sensitivity complex on the RATAN-600 feed cabin №1, consisting of 5–7 broadband radiometers, — at wavelengths of 1.4, 2.1, 2.7, 3.9, 6.2, 7.6, 8.2, 13, 24 and 31 cm (some of them were temporary and today are absent — see Fig. 1–6). Processing the observations and analyzing the results are performed on modern computers using a software package developed and updated by the authors. The useful signal is extracted from the background noise by "fitting" (matching) the model response to the observed one, which is equivalent to the optimal signal filtering mode. In this case, the code by V.R. Amirkhanyan for the formulas by Stotsky is used to calculate the RATAN-600 radiation pattern (taking into account real aberrations due to the transverse offset of the input feeds from the antenna focus) and the well-known SVD singular value analysis program (Forsite et al. 1980) to reduce the errors of machine matrix inversion when approximating the observed response. A number of other processing programs, all programs for statistical and model analysis of the spectra and structure were developed by Y.Y. Kovalev. The signals from all radiometers are recorded simultaneously and independently (see an example in Fig. 2). The multi-frequency response to the passage of the source is obtained in a few minutes due to the daily rotation of the Earth. Each observation at each frequency, usually 3–5–7 minutes long, begins and ends with a series of responses to the switching on of a highly stable noise signal generator (NS) of constant power. As usual, the amplitude of the NS-signal plays the role of the division value of a high-precision ruler (of variable length due to variations of the gain),"applied"' to different records for the relative measurement of the amplitude for the antenna temperatures responses T/T_{NS} . Based on observations of known calibration objects — generally accepted standards of the spectral flux density scale — the amplitude of the NS-response is calibrated in units of this scale (at the heights of the calibrators, after averaging repeated observations and taking into account corrections for partial angular resolution and polarization), and then, using regression analysis methods, the calibration dependence $F_{\mathrm{NS}}(h)$ is approximated over the entire interval of observation heights h (Fig. 3). After this, the measured spectral flux density F of the object under study is calculated as $F = (T/T_{\mathrm{NS}})F_{\mathrm{NS}}(h)$. If necessary, the T/T_{NS} value of the objects under study and calibration is corrected for atmospheric absorption by calculations using meteorological parameters. Errors are estimated using the mean error propagation method and the value of the residual sum of squares. All average values are calculated as weighted averages using the method recommended by Agekyan (Agekyan 1972). Their error was further increased by the Student's correction due to the finite number of measurements, to bring the probability characterizing the root-mean-square interval of one sigma to the standard value of 0.683.

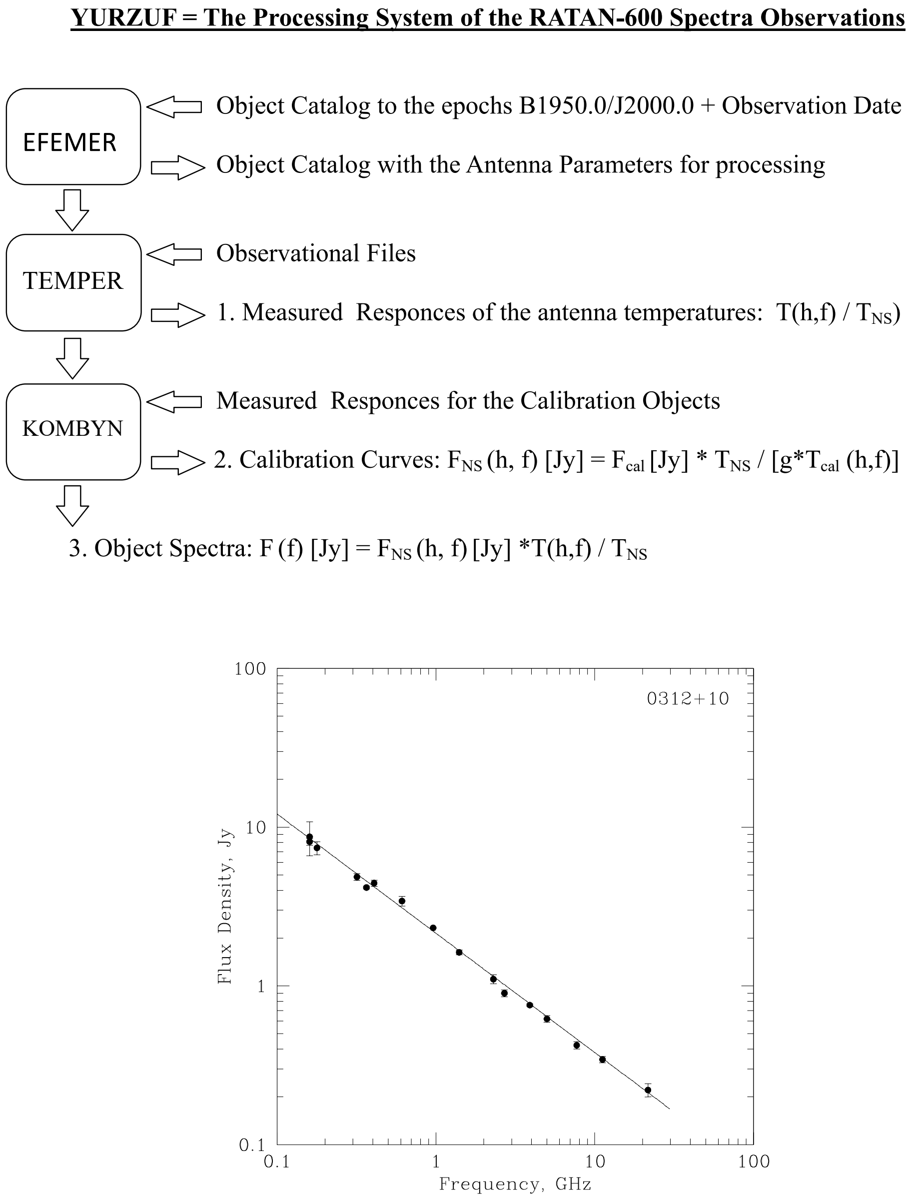

Figure 1. The block diagram of the YURZUF system (top) and the test results of its work (bottom): the RATAN-600 (1–22) GHz data are in agreement with the spectrum (Verkhodanov et al. 2005) out of (1–22) GHz. Top we have defined: T and F — antenna temperature (in K) and spectral flux density (in Jy), $T_{\rm NS}$ — the temperature of the Noise Source, g — correction for angular size and polarization, f — frequency, h — height of the object above the horizon; the calibration curve $F_{\rm NS}(h, f) = 2kT_{\rm NS}/A_{\rm eff}(h, f)$, where $A_{\rm eff}(h, f)$ — the antenna effective area.

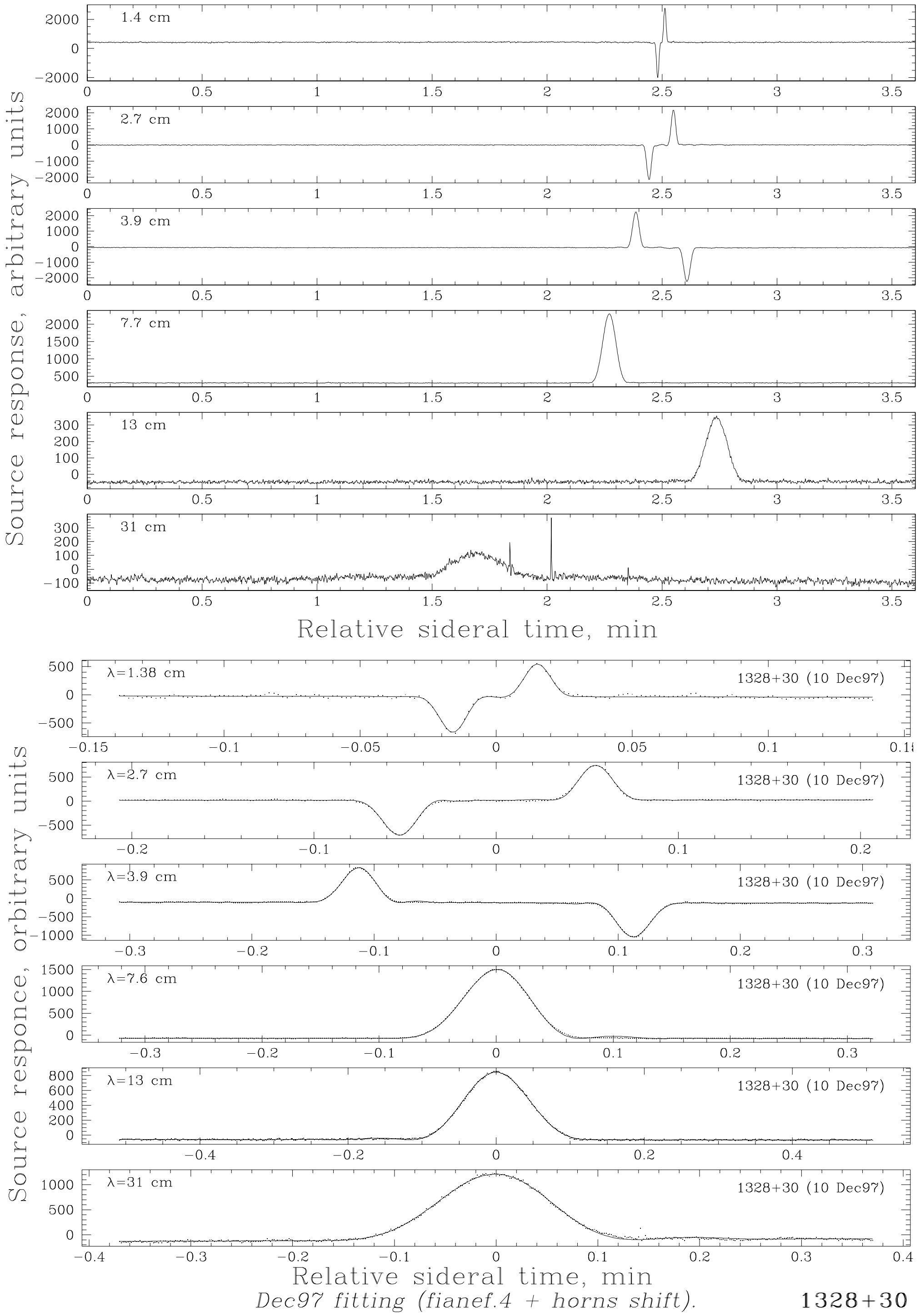

Figure 2. Top (Kovalev et al. 1999): examples of the RATAN-600 radio telescope responce to the passage of the source B0923+39 through fixed antenna patterns during the Earth's daily rotation. Observations were made on December 16, 1997, at 6 wavelengths from 1.4 to 31 cm with an integration time of 0.1 s. Bottom (Kovalev et al. 1999): examples of processing the B1328+30 calibrator. Approximations of the observed responses (dots) by the calculated RATAN-600 radiation pattern (solid line). Two responses at wavelengths of 1.4, 2.7 and 3.9 cm display the diagram modulation of the signal.

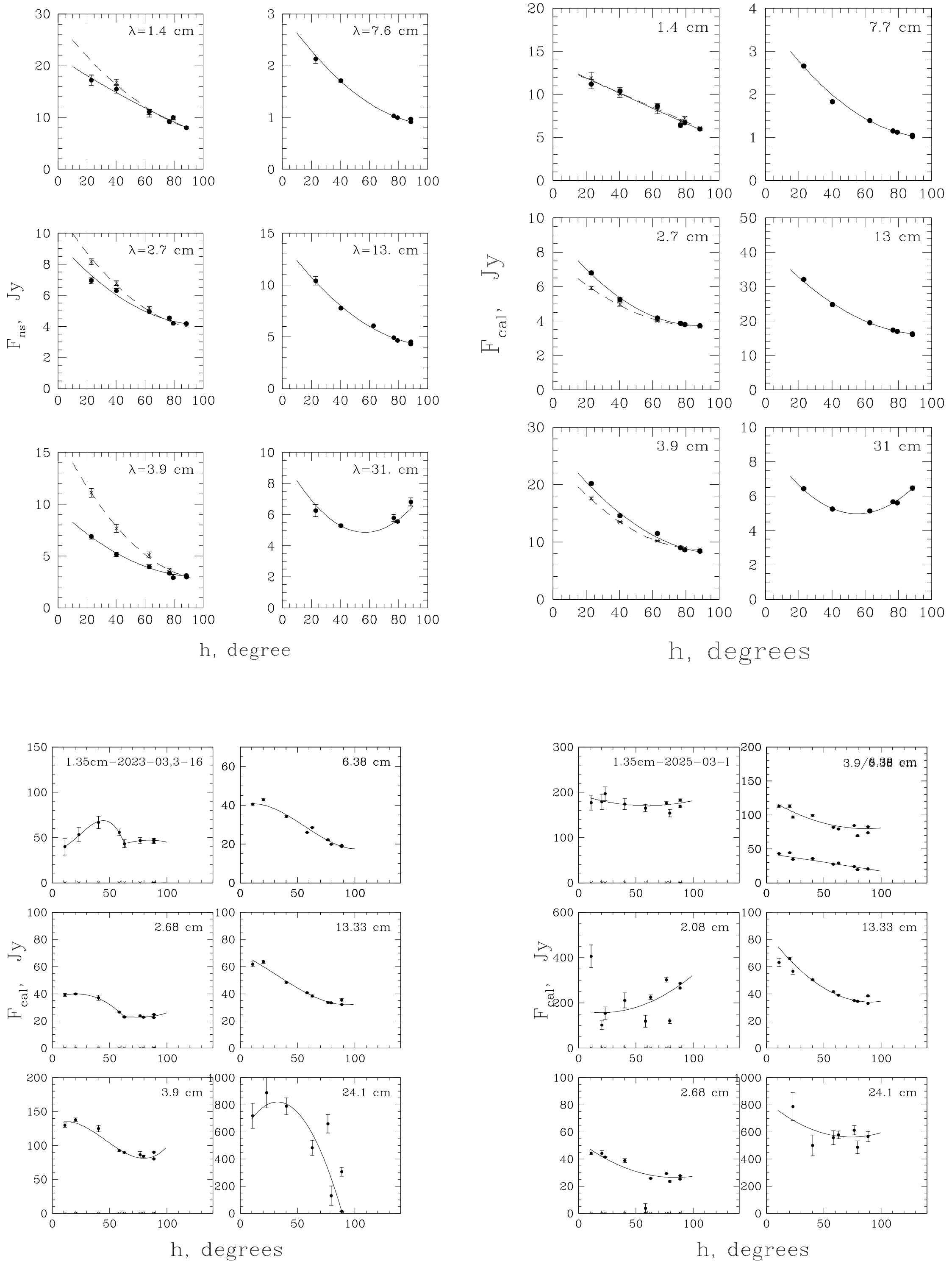

Figure 3. Examples of calibration curves obtained by the program KOMBYN for 4 sets in July 1996 (two columns on the left, top), December 1997 (two columns on the right, top), 3–16 March 2023 (two columns on the left bottom), 2–15 March 2025 (two columns on the right bottom). Calibration curves $F_{\rm ns}(h) = 2kT_{\rm ns}g_{{\rm atm}(h)}/A_{\rm eff}(h)$ display the averaged over the cycle time dependence of the Noise Signal amplitude $F_{\rm cal} = F_{\rm ns}$ on the height h above the horizon at the working wavelengths, obtained by the calibrators. The calibrations of the each of two modulated responces of the signal (top) are different. Such signals are averaged later.

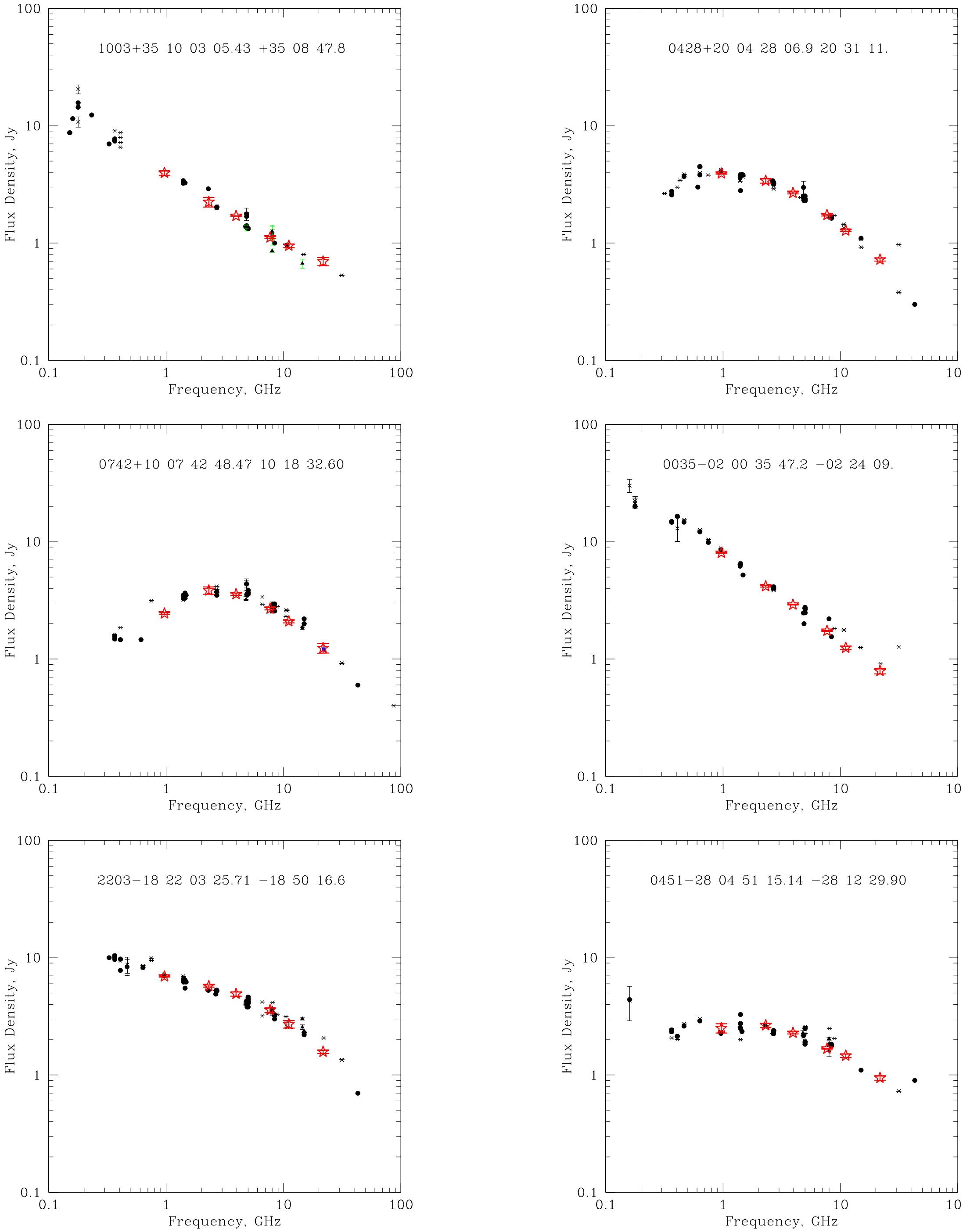

Figure 4. Examples of testing the RATAN-600 calibration solutions in (1–22) GHz using 6 objects with different heights and wide spectra measured by other telescopes (similar to Fig. 1, bottom). RATAN-600 data are marked with a red "asterisk". The rest of the data are from the CATS database (Verkhodanov et al. 2005). To the right of the source name in each window are the source coordinates for the epoch B1950.0.

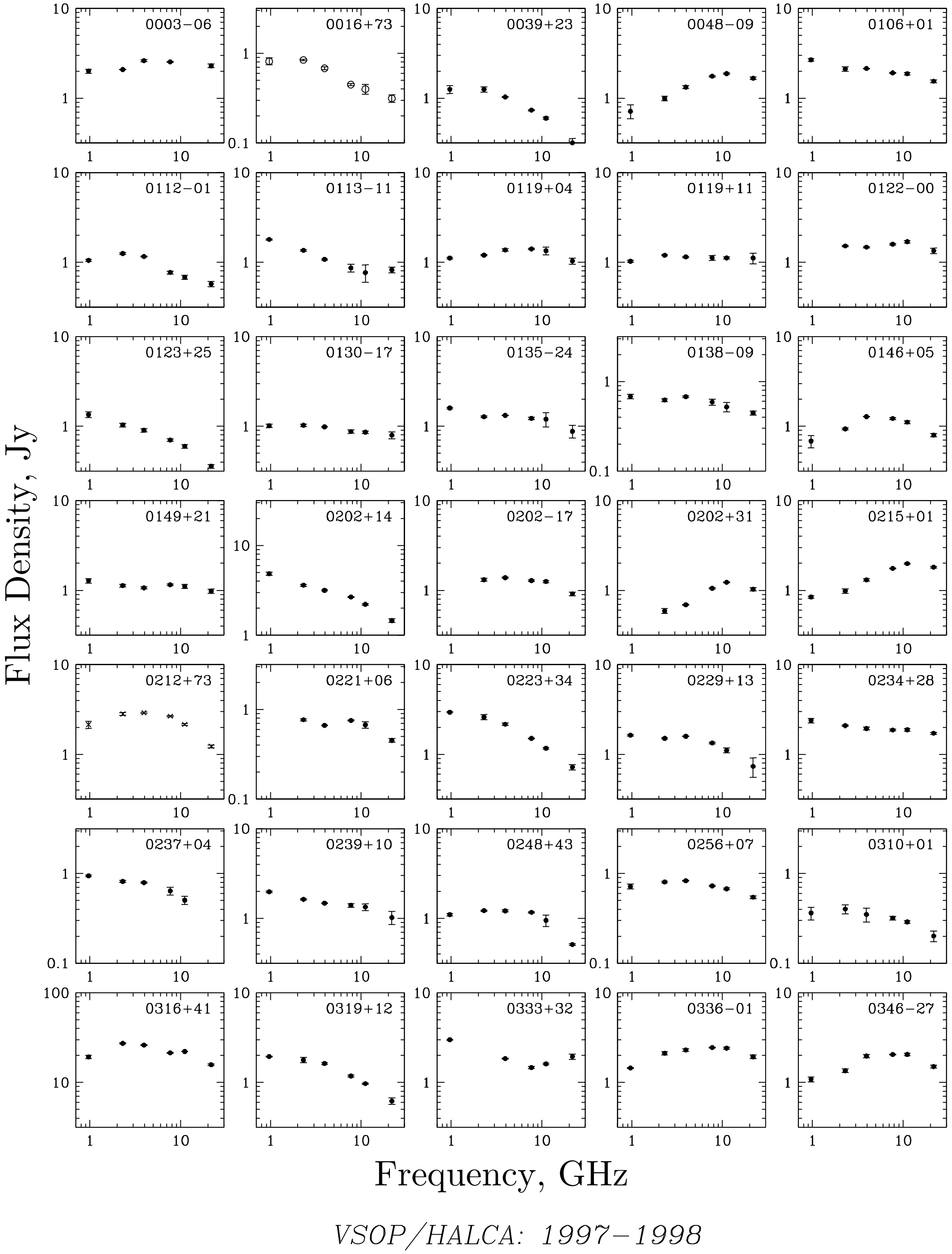

Figure 5. Some examples of reducing the RATAN-600 1–22 GHz spectra observations by the YURZUF package: the instantaneous spectra for 35 VSOP/HALCA objects in 1997–1998 (Kovalev et al. 2000).

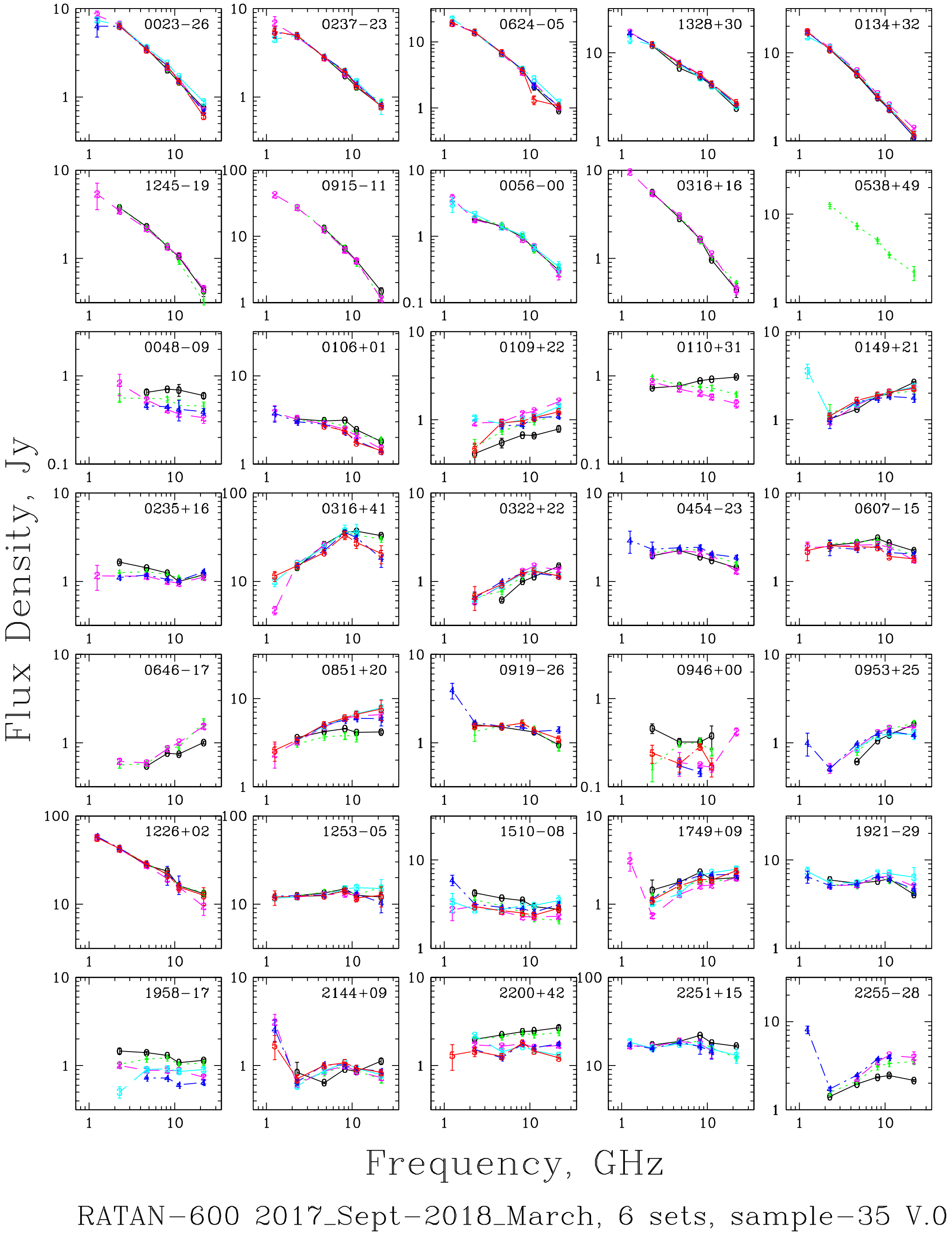

Figure 6. Checking the quality of the RATAN-600 flux density calibrations: 1–22 GHz spectra at 6 frequencies for 10 calibration objects (first 10 objects, top) and for 25 quasars and galaxies from the RadioAstron sample in 6 sets of 2017–2018. The interferences are visible in some cases.

3. The YURZUF software package

The package is intended for automatic processing of instantaneous spectra of radio emission of discrete objects measured on the RATAN-600 radio telescope, and includes the entire set of basic and utility programs and batch scripts necessary for this — from calculating the used parameters of the radio telescope and isolating the signal from the primary noise recording of the telescope response in ADC units to generate a table with the final results of measuring instantaneous and averaged over a cycle spectra for each source.

The package consists of 3 basic processing programs EFEMER, TEMPER and KOMBYN, written in FORTRAN-77, the sequential operation of which implements the processing task, several utilities and command files (see Fig 1). The utilities facilitate the preparation or modification of service files and the conversion of the data format to a form convenient for graphical display of results.

The EFEMER program for each object in the list for a given observation date calculates the coordinates of the source, its height and the speed of image movement in the focal plane (due to the Earth's rotation), as well as the focal parameter of the radio telescope (the distance from the antenna focus on top of the feed cabin to the center of the antenna ring reflector). The results are written to the same table, which is then used as a service file by the TEMPER and KOMBYN programs.

The TEMPER program extracts the desired signal from the original noise record of measurements and normalizes it to the amplitude of the calibration signal from the internal stable noise generator for calibration by antenna temperature. The results for each source at each frequency (channel) are written to a separate output file, which serves as an input for the KOMBYN program.

The KOMBYN program combines 5 independent programs and performs 8 functions: 5 functions for processing calibration objects in order to obtain an approximation of the calibration dependence — of the normalized effective area of the antenna on the source height in order to calibrate measurements in units of the spectral flux density, — and 3 functions for processing measurements of each object from the initial list (specified by the EFEMER program), using this calibration dependence and the output files of the TEMPER program. The final results are obtained for the instantaneous and cycle-averaged flux density spectra (in Jy-units), which are written in tabular form to the corresponding output files (Fig. 5–6).

4. Summary

1. The results demonstrate a high quality of approximation of real responses of quasi-point sources by calculated responses.
2. More details on the methods of observations and data processing can be obtained in Agekyan (1972); Forsite et al. (1980); Kuzmin et al. (1964); Kraus (1966); Esepkina et al. (1973); Konnikova et al. (2011); Kovalev et al. (1999, 2000, 2002); Kovalev (1997); Verkhodanov et al. (2005).

References

Agekyan T.A., 1972, Fundamentals of Error Theory for Astronomers and Physicists, M. "Nauka"
Esepkina N.A., Koroljkov D.A., Parijskij Yu.N., 1973, Radio Telescopes and Radiometers, M. Nauka
Forsite J., Malcolm M., Mouler K., 1980, Machine Methods of Mathematical Calculations, M. "Mir"
Konnikova V.K., Leht E.E., Silantjev N.A., 2011, Practical Radio Astronomy, M. MGU
Kovalev Yu., 1997, Bull. of Spec. Astrophys. Obs., 44, p. 50
Kovalev Yu.Yu., Nizhelsky N., Kovalev Yu.A., et al., 1999, Astron. Astrophys, Suppl., 139, p. 545
Kovalev Yu.A., Kovalev Yu.Yu., Nizhelsky N., 2000, Publ. Astron. Soc. Japan, 52, p. 1027
Kovalev Yu.Yu., Kovalev Yu.A., Nizhelsky N., et al., 2002, Publ. Astron. Soc. Australia, 19, p. 83
Kuzmin A.D., Salomonovich A.E., 1964, Radio Astronomical Methods of Measuring Antenna Parameters, M.: Sov.Radio
Kraus J.D., 1966, Radio Astronomy, McGraw-Hill Book Company
Verkhodanov O., Trushkin S., Andernach H., et al., 2005, Data Science Journal, 8, p. 34

Radio frequency interference at the RATAN-600 radio telescope site

D. Kratov · N. Nizhelsky · P. Tsybulev · R. Udovitskiy

Special Astrophysical Observatory of the Russian Academy of Sciences,
Nizhny Arkhyz, 369167 Russia

DOI: 10.26119/2025-moc07
eLocator: moc07
EDN: kepgfn

Abstract. The analysis of the radio frequency interference (RFI) shows an exponential increase of the artificial RFI level near the radio telescope RATAN-600 over the years. The current RFI situation is presented.

Keywords: radio frequency interference; frequency management; RFI mitigation

1. Introduction

The need for constant monitoring of the radio frequency interference (RFI) situation at radio telescopes is dictated by a sharp increase in the number of radio frequency bands the use of which is limited or unavailable for radio astronomy observations. The radio telescope RATAN-600 performs astronomical observations in a wide range of wavelengths from 1 GHz to 30 GHz. The bandwidths of the RATAN-600 receivers and their protective zones are shown in Fig. 1.

The RFI situation is currently particularly complex in the decimeter wavelength range from 1 to 3 GHz. This is due to the rapid development of communication systems, television, radio broadcasting, and household microwave equipment. Classical methods of RFI mitigation such as frequency tuning to interference-free areas are becoming unavailable due to the absence of such intervals in the decimeter wavelength range for frequency bands that are 10–15% wide (Kratov et al. 2010). Out-of-band radiation, variable both in amplitude and frequency, makes effective long-term filtering of the signal impossible, and moving to RFI-free zones does not provide the expected long-term effect since the RFI situation in the decimeter wavelength range changes dynamically, which requires constant RFI monitoring (Tsybulev et al. 2007).

2. RFI measurement methods at RATAN-600

2.1. Method 1 — RFI measurement using the radio telescope antenna

The main method of RFI measurement at RATAN-600 is the standard operation mode as in usual radio astronomical observations with the total microwave gain of the radiometer. However, this method requires suspension of observations on the radiometer which is being measured, so its use is limited in time. To use the method without interruptions, a small modification of the standard radio telescope radiometers is necessary. A typical solution to complement a radiometer is shown in Fig. 2. The modification of the radiometer allows conducting the RFI investigation during observations. This method has a number of obvious advantages:

- measurement of the exact spectrum of the RFI that is intercepted by the radio telescope antenna during observations;
- detection of even the smallest variation in RFI power, which is achieved by using the large radio telescope antenna and full amplification of standard radiometers;
- a side effect of this method is the ability to quickly test the amplification paths of radiometers using the interference measurement system connected to the output of the microwave radiometer blocks.

2.2. Method 2 — RFI measurement with a portable antenna

The primary receiver is a broadband antenna HL040 manufactured by Rohde & Schwarz, designed for the range of 400 MHz – 3.2 GHz, and a spectrum analyzer Rohde & Schwarz FSU46 for the range of 20 Hz – 46 GHz. The spectrum analyzer is connected to the HL040 antenna using a 5-m-long semirigid copper coaxial cable. Additionally, a block of two broadband low-noise amplifiers with an operating range of 200 MHz – 3 GHz with a gain of 34 dB is installed at the output of HL040. We call this solution a "Mobile highly sensitive complex for measuring RFI in the decimeter and meter wavelength range".

Based on the results of testing the measuring complex, it was established that the complex is also capable of measuring RFI within 80 to 400 MHz outside the standard range with an efficiency of approximately 20 percent lower than the manufacturer's specifications.

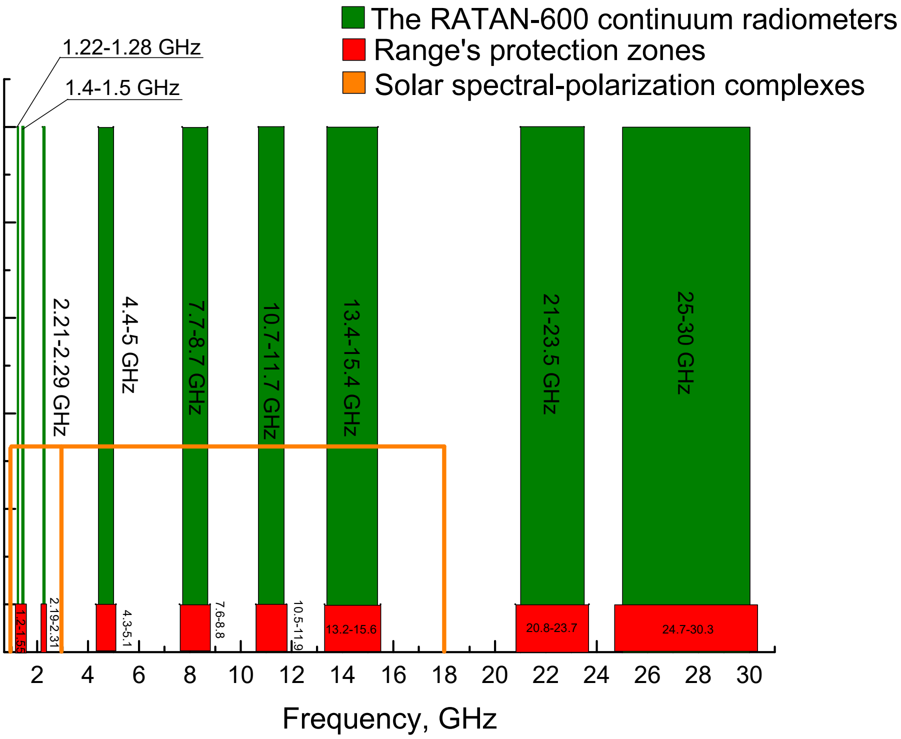

Figure 1. Operating bandwidths of the RATAN-600 receivers.

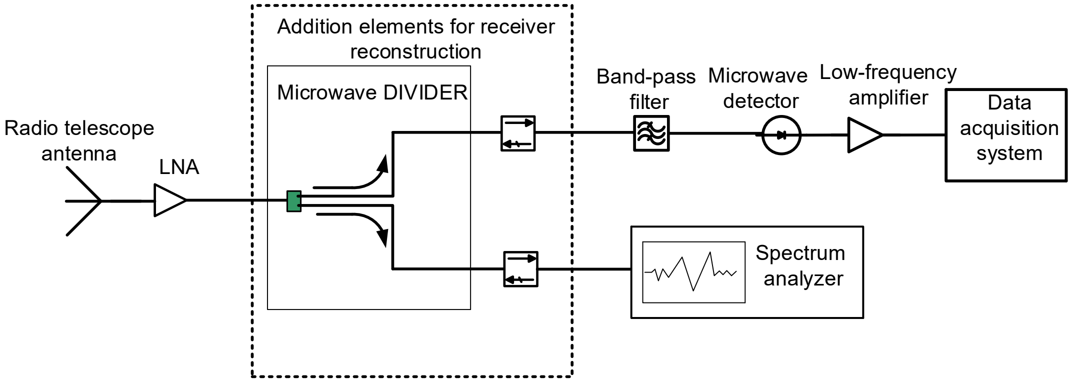

Figure 2. Block diagram of RATAN-600 receiver modification.

3. Results of RFI measurements

The main strong sources of RFI in the decimeter wavelength range are the GSM communication networks working in the bands of 850–980 MHz, 1700–1900 MHz, 2100–2170 MHz (3G), and 2570–2680 MHz (LTE). Among the strong RFI, we can also highlight Wi-Fi in the range of 2400–2480 MHz and frequencies around 400 MHz: these are usually radios, automatic doors, gates, etc. This type of interference does not act constantly both in the frequency range and in time. We can

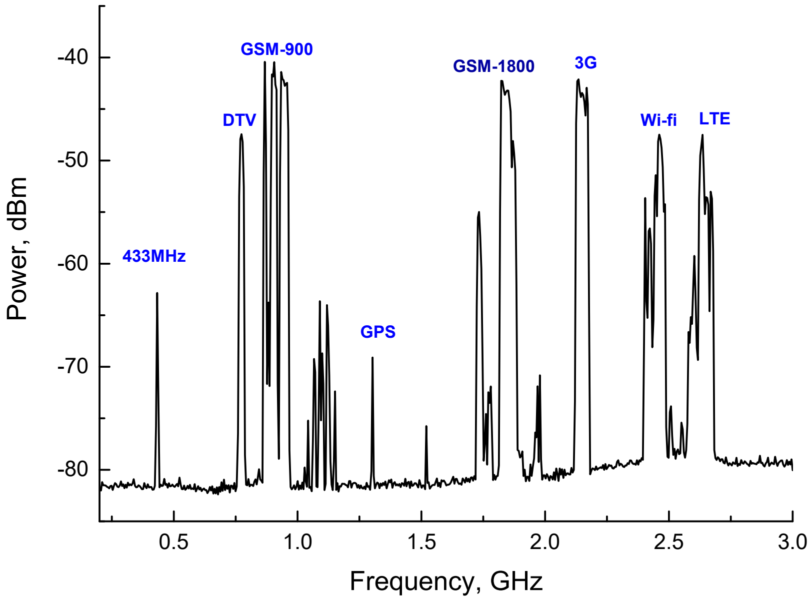

Figure 3. Known sources of RFI in the decimeter wavelength range.

also point out a high RFI level from digital television (DVB-T2) in the range of 750–800 MHz and from global positioning systems at several frequencies in the range of 1100–1600 MHz.

Harmonics or out-of-band radiation of strong RFI signals are the only other types of weaker interference. In Fig. 3 the interference environment is shown, considering the known sources of RFI.

Due to its design, RATAN-600 simultaneously conducts several observing programs using different sectors of the primary mirror and different secondary mirrors. Usually, three observing programs are carried out simultaneously. Since they use different primary mirror sectors, the RFI situation differs for each of the program because the beam patterns of the sectors and secondary mirrors are oriented differently with respect to the RFI sources. Figure 4 demonstrates this difference in RFI for two sectors of the RATAN-600 antenna in the decimeter wavelength range. The measurements were carried out using method 1 described above.

We should note that the above-described features of RATAN-600 can be both an advantage and a disadvantage of the radio telescope, depending on the observing program. It should also be taken into account that part of the RFI signals are polarized. Figure 5 shows the difference in the RFI situation depending on polarization.

At the same time, the RFI situation in the decimeter wavelength range at RATAN-600 is not that bad as it could have been if the telescope were located elsewhere. Let us compare the RFI at RATAN-600 with the RFI near the 6-m optical telescope (BTA) located not far from RATAN-600. In a simple case (the mathematical model of the absolute sphere), the difference between the radio horizons at the RATAN-600 altitude (we take it as the zero altitude) and at the BTA height of +800 meters is approximately 116 km, i.e. the radio horizon for the RFI reception at the BTA location is approximately 116 km further compared to the RATAN-600 site.

The above-described result of calculating the radio horizon does not take into account refraction and diffraction, the properties of the medium and underlying surface, and other phenomena. In reality, most often the effect of “bending” the wave downward occurs (although sometimes it happens the other way around), which allows “looking beyond the horizon”; and to take this effect

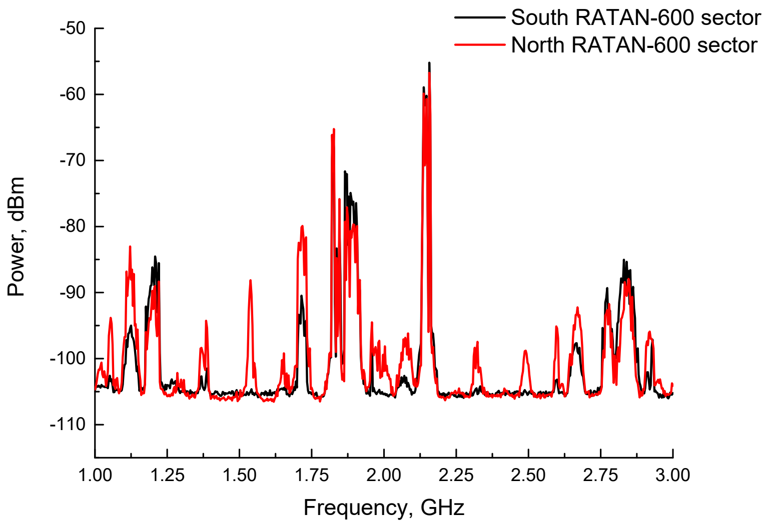

Figure 4. Comparison of RFI in the decimeter wavelength range for different RATAN-600 sectors.

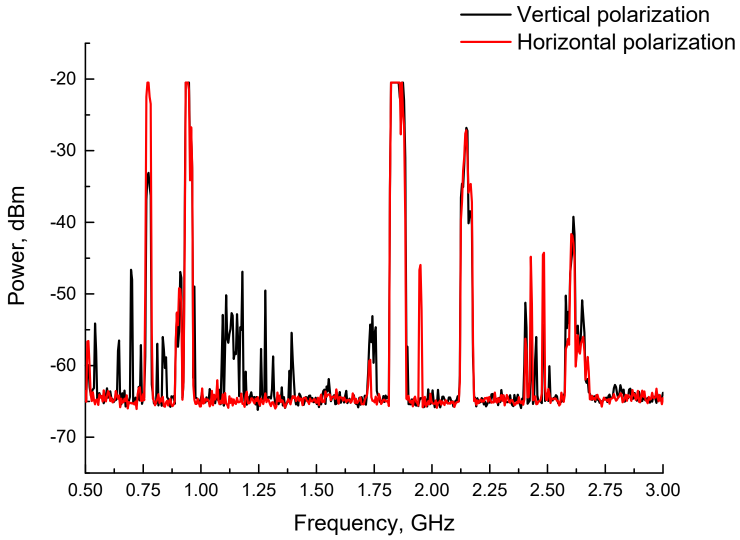

Figure 5. RFI dependence on polarization.

into account, an empirical coefficient of 4/3 is usually used, which increases the radio horizon by 33%, although this is also a simplification to a very large extent and does not take into account the dependence on wavelength, the state of the atmosphere at a particular moment in time, etc. Based on the above, we accept the difference between the "ideal" radio horizons at the RATAN-600 and BTA locations as 154 km.

In the case of comparing the terrain of the BTA and RATAN-600 locations, this difference is even worse, since RATAN-600 is located in the valley of the Bolshoy Zelenchuk River. This means that RATAN-600 is shielded on two sides by the natural landscape of the valley (the height of the slopes above the RATAN-600 altitude is on average about 80 meters), on the third side it is protected by

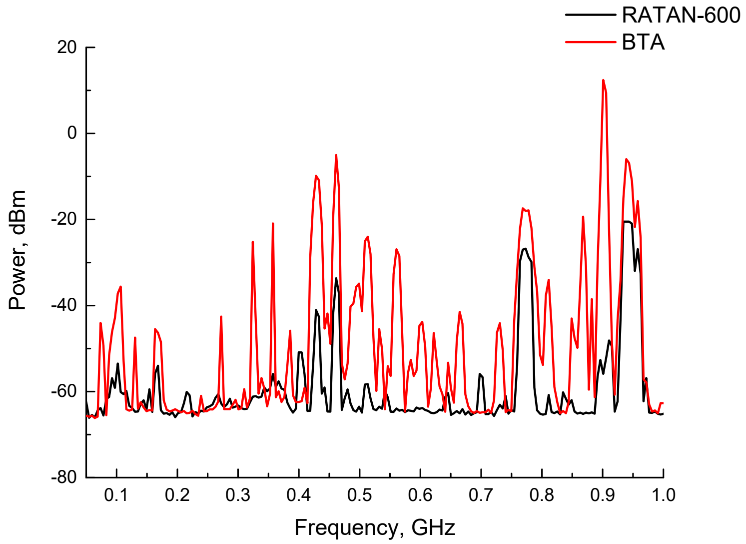

Figure 6. A comparison of RFI at the RATAN-600 and BTA locations, 50 MHz–1 GHz.

Mount Dzhissa (about 300 m above RATAN-600), and from the side of Georgia/Abkhazia there is the Greater Caucasus Range. Thus, in the neighborhood of RATAN-600, RFI comes mainly from the settlements closest to the telescope (Zelenchukskaya, Dausuz, Ermolovka): government and civilian services and home appliances.

At the BTA location, RFI are detectable from settlements at least 154 km farther. These are cities such as Cherkessk, Dzheguta, and Karachayevsk, and at least more than 80 smaller settlements. It is likely that at the BTA site we also detect RFI from Mineralnye Vody, Stavropol, Kislovodsk, Pyatigorsk, and other cities, which are formally farther than the calculated distance of 154 km, but this value does not take into account the terrain and the location of RATAN-600 under the "natural screen" protection provided by the valley of the Zelenchuk River and by the mountains in the directions toward these relatively large cities. Figures 6, 7, and 8 show a comparison of RFI at the RATAN-600 and BTA locations.

4. Summary

The electromagnetic environment in all wavelength ranges used by RATAN-600 has been deteriorating for the last 30 years and will continue to deteriorate. One possible solution in the decimeter wavelength range is shielding RATAN-600 from the main source of RFI – Zelenchukskaya. Satellite Internet systems and other services are being independently developed in the EU, China, Russia, Brazil, and India, and despite the fact that their frequency grids are most likely going to be close to Starlink, they still will be shifted for each new system relative to its predecessors, which may affect the frequencies currently used by observational radio astronomy.

The recently approved 5G range (4.4–4.99 GHz) in Russia will make it impossible to observe with one of our radiometers at the 4.4–5 GHz bandwidth. The RFI situation in the band from 300 MHz to 6.2 GHz is going to worsen due to the upcoming data transmission technologies in this frequency range. It may be assumed that in the coming years the RFI in the range from 3 GHz to 6 GHz will become similar to the situation in the decimeter wavelength range at present.

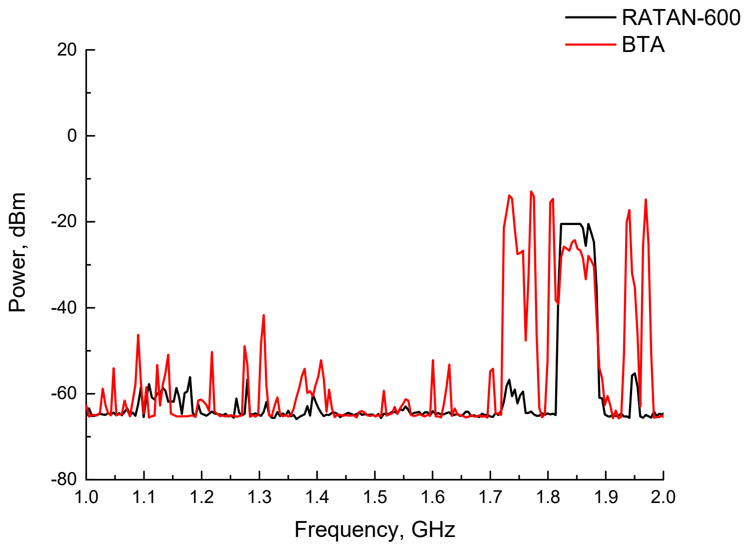

Figure 7. A comparison of RFI at the RATAN-600 and BTA locations, 1–2 GHz.

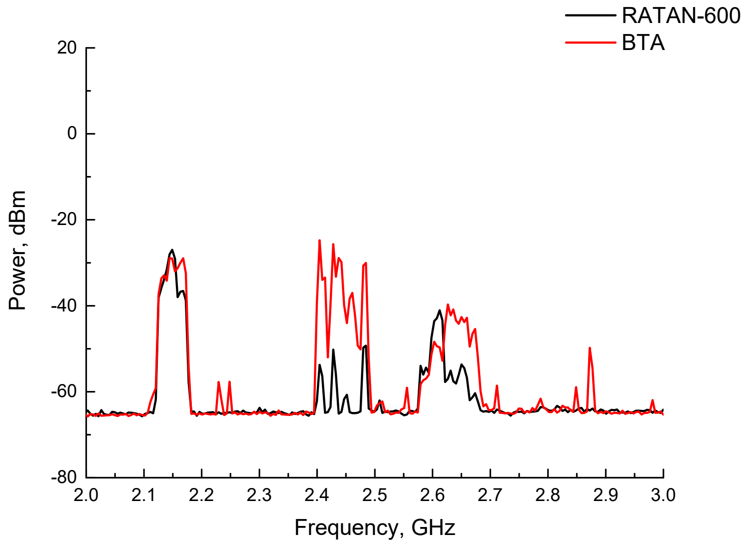

Figure 8. A comparison of RFI at the RATAN-600 and BTA locations, 2–3 GHz.

Acknowledgements Observations with the SAO RAS telescopes are supported by the Ministry of Science and Higher Education of the Russian Federation. The renovation of telescope equipment is currently provided within the national project "Science and Universities."

References

Kratov D., Berlin A., Nizhel'skij N., et al., 2010, Proceedings of the RFI Mitigation Workshop, 29–31 March 2010, Groningen, the Netherlands, id. 022

Tsybulev P., Berlin A., Nizhel'skij N., et al., 2007, Astrophysical Bulletin, 62, 2, p. 193

Running a hybrid astronomy program for school students and adults: insights from Petrozavodsk State University

M. Maricheva[1] · **N. Lyapsina**[1] · **N. Skorikova**[2] ·
N. Larionova[3]

[1] Special Astrophysical Observatory of the Russian Academy of Sciences, Nizhny Arkhyz, 369167 Russia
[2] Petrozavodsk State University, 33 Lenin Av., Petrozavodsk, 185910 Russia
[3] Volzhsky Industrial and Technological College, 6 Shchorsa st., Volzhsk, 425005
Russia

DOI: 10.26119/2025-moc08
eLocator: moc08
EDN: fnggio

Abstract. With astronomy removed from the school curriculum, students have limited opportunities to pursue their interest in this field: they can either study for specialized Olympiads or independently watch documentaries and read popular science books. As a natural science, astronomy not only broadens students' worldview but can also influence their career choices and academic trajectories. In order to popularize astronomy both as a science and as a hobby, it is essential to provide educational opportunities in astronomy to adults as well. Yet only a few cities offer specialized clubs where non-students can deepen their knowledge of astronomy and pursue their interest in space. The advances in information technologies expand the potential of both educational and popular science projects. The introduction of online classes not only increases participant numbers but also allows for the involvement of a broader pool of instructors and creates more flexible learning conditions. This report discusses the experience of transitioning the Asterion Astronomy Program at Petrozavodsk State University from in-person classes to an online format. It examines the advantages and disadvantages of this model, the challenges of engaging young people and sustaining their motivation, and analyzes the results achieved over several years. The authors emphasize the importance of implementing various astronomy-related projects for both school students and adults within the framework of continuous natural science education, contributing to the development of a well-prepared cohort of future university students and professionals pursuing careers in astronomy.

Keywords: astronomy education; supplementary education; astronomy club

1. Introduction

After astronomy was removed from the school curriculum, students have had limited opportunities to engage with this field of interest. Within the existing curriculum, astronomy is addressed only incidentally in subjects such as physics and geography, which hinders the development of a coherent scientific worldview. In addition to its role in shaping a broader scientific outlook, studying astronomy during school years may influence students' future career choices and academic pathways (Parko et al. 2016; Skorikova & Kuznetsova 2020).

A number of studies report a decline in scientific literacy among Russian school students (Kersha & Obukhov 2023; Shiling 2023; Belikova & Novolodskaya 2022). Shiling (2023) argues that the cultivation of scientific literacy can be effectively supported through various extracurricular activities, special interest classes, and project-based learning. Consequently, expanding supplementary education in this area remains a relevant objective.

Krupa et al. (2021) examine a number of studies on the implementation of digital technologies and online formats in supplementary education.

In its traditional form, astronomy education in Russia is maintained primarily through school Olympiads, in-person clubs, and interest groups at schools and universities. Planetariums also play a notable role, with outreach activities targeting both students and adults (Novichonok & Skorikova 2015).

Previous studies have highlighted several benefits of incorporating digital technologies into education, noting in particular the flexibility of online formats and the opportunities they provide for independent study. Research also suggests that student engagement in online classes increases when learners can interact with one another, receive feedback from teachers, and participate in smaller groups. Students' evaluations of online courses are reported to depend on such factors as the teacher's involvement and enthusiasm, the appeal of the course content, the inclusion of assessment, and the cost of participation. Moreover, online education is considered to have a positive impact on reducing social and economic inequality by expanding access to supplementary education and offering a degree of anonymity in the digital environment (Krupa et al. 2021; Harvey et al. 2014).

Despite these findings, the specific issue of online clubs as a form of supplementary education for school students has received little scholarly attention. Most existing studies focus primarily on the use of digital tools within traditional in-person classes. Addressing this gap, the present paper explores the potential of distance learning for supplementary education, using the astronomy program for school students organized at Petrozavodsk State University as a case study.

2. Program structure and delivery

The Asterion Astronomy Program dates back to 2008, when it was established at Petrozavodsk State University as a club for university students. Since then, it has expanded to include astronomy enthusiasts of all ages who appreciate the subject in its broadest sense – not only as a science but also as a hobby.

In response to the participants' request, a general astronomy program for school students was launched in 2012 as part of Asterion. Its members attended in-person lectures covering various astronomy topics, delivered in a popular science format.

The primary goal of the Asterion Astronomy Program is to popularize astronomy and science in general. At the same time, it aims to address the following objectives:

- educational – to provide all interested individuals with a general understanding of basic concepts in astronomy;
- career guidance – to encourage high school students to pursue astronomy as well as other science-related fields;

- popularization – to attract a broader audience to amateur astronomy.

For a detailed account of the program's experience with in-person activities, see Novichonok & Skorikova (2015).

In 2020, due to the COVID-19 pandemic and restrictions on in-person events, Asterion launched online classes, which have continued ever since. These classes are held once a week throughout the academic year for two age groups: the younger group (school students in grades 1–6) and the older group (school students in grades 7–11 and adults). The program structure allows the same topic to be studied in both groups but with different approaches: the younger group receives adapted, condensed information through the use of game-based methods, while the older group follows a more in-depth curriculum aligned with the school physics syllabus.

Each academic year focuses on one specific branch of astronomy, such as *General Astronomy and Space Exploration*, *The Solar System*, or *The World of Stars and Galaxies*. Students can join the program at any time and attend it for several years, continuously exploring new topics. Moving from the younger group to the older one also marks an important milestone for participants. The course curriculum is compiled by a team of instructors before the start of each academic year, and it includes 26 one-hour classes per age group, conducted from October to May, with special emphasis placed on ongoing astronomical events and recent discoveries.

Unlike the more common model of distance learning which relies on students independently viewing pre-recorded lessons, classes are conducted in real time via online conferencing platforms and take the form of lectures with opportunities for discussion. This format enables continuous interaction between participants and instructors, allowing students to seek clarification at any point via microphone or chat. Additionally, at the end of each class there is designated time for discussion, questions, and feedback.

3. Online delivery: effectiveness and limitations

The transition to an online format has had a considerable impact on membership numbers. In the 2012–2019 academic years, the number of registered attendees fluctuated from 36 to 84 per year, with the majority (55–60%) belonging to the older age group. On average, each class was attended by approximately 7 to 10 participants. Following the shift to the online model, attendance increased due to the inclusion of participants from various districts of Karelia and even other Russian regions. In the 2024–2025 academic year, 182 participants registered for the program, representing 10 districts within Karelia and 16 other regions across Russia. Among these, 47% enrolled in the younger group and 53% in the older group; notably, 25% of all applicants were returning participants. On average, about 20 individuals attended each class, and approximately 60 participants attended more than half of all classes throughout the year.

The experience gained from the online model has helped determine the optimal group size: no more than 25 participants per class. This number enables instructors to sustain engagement, address all questions, and ensure proper classroom management – the latter being particularly important for younger students. The curriculum is designed in a way that allows participants to join the course at any point during the academic year.

That said, there is a notable discrepancy between the number of applications submitted and actual attendance. Attrition occurs due to various reasons, including a demanding academic or professional workload, changing priorities, a mismatch between participants' expectations and the course format, or the difficulty of the material. Attracting and retaining students is a challenge faced by many supplementary education providers, and in order to address this, the Asterion Astronomy Program conducts annual surveys to evaluate its strengths and areas for improvement.

It should also be noted that the program's activities extend beyond the online format, since observations – an essential component of astronomy education – are highly challenging to conduct remotely. Therefore, members from Petrozavodsk and its surroundings are regularly invited to in-person observations as well as training sessions on working with astronomical instruments. Provided that they have the appropriate personal equipment, participants from other regions have the opportunity to conduct observations independently with remote guidance of the program's instructors via online or telephone communication. Asterion also regularly shares links to live broadcasts of major astronomical events on its VKontakte page. In addition, the program's instructors have organized a number of lectures and practical sessions in schools across various districts in Karelia; with stable funding, such outreach efforts could be sustained on a consistent basis.

In conclusion, it is worth outlining the key advantages and challenges of the hybrid format employed by the Asterion Astronomy Program.

Advantages

- *Wider reach among students and educators.* The online format brings in participants from remote areas of Karelia, which is particularly important given the limited availability of similar opportunities in smaller towns. Moreover, highly qualified experts, such as observatory staff, planetarium employees, and other specialists, can also be invited to participate.
- *More reliable class scheduling and attendance.* The transition to online classes minimizes the impact of illnesses, quarantines, and other unanticipated disruptions.
- *Faster and more effective feedback.* Modern school students are accustomed to online communication and, in many cases, find it easier to ask questions from the comfort of their own homes than in a classroom setting. Moreover, many online conferencing platforms allow attendees to send questions directly to the instructor or to the group chat while the class is in progress.
- *Opportunity for people with limited mobility to participate.*

Challenges

- *High level of engagement and self-discipline required.* It can be difficult for school students to remain focused throughout an entire class session, and the home environment provides numerous distractions, such as gaming, snacking, or simply moving around.
- *Technical issues.* Unstable Internet connection, microphone malfunctions, and sound problems – for both teachers and students. In most cases, such issues are resolved promptly or mitigated through compromise solutions.
- *Difficulty in monitoring comprehension.* Although some students may remain silent in in-person classes as well, they are easier to notice in a face-to-face setting, where instructors can engage them directly by asking questions or eliciting opinions. In online classes, it is more difficult to identify such "silent participants."
- *Limited opportunities for group work.* The online setting poses challenges for organizing group work. While some platforms offer breakout room functionality, it can be difficult for a single instructor to switch between rooms in order to effectively monitor progress in each group.

The lack of face-to-face interaction between all participants is also often cited as a disadvantage of online classes; however, given the program's hybrid format, this disadvantage is mitigated by in-person events.

In summary, the program currently serves a relatively small region, so the online lecture format described in this paper has proven to be both sufficiently effective and convenient. However, an increase in the number of students could lead to organizational difficulties and a decrease in instructional quality. In this case, launching similar initiatives in other regions could be a viable solution. The experience of the Asterion Astronomy Program demonstrates that such projects in supplementary astronomical education are in demand and can serve not only as a meaningful stepping stone in the training of future experts in the natural sciences but also as a valuable tool for improving public literacy in astronomy.

4. Conclusion

The experience of the Asterion Astronomy Program at Petrozavodsk State University operating in a hybrid format demonstrates the high demand for supplementary education in astronomy among both school students and adults. The shift to online classes has significantly expanded the audience, bringing in participants from remote areas of Karelia and other regions of Russia, which is particularly important given the absence of astronomy in the compulsory school curriculum.

The flexible format of online lectures with opportunities for discussion, adapted to different age groups, has proven effective. Key advantages of distance learning include accessibility for remote participants, the opportunity to involve highly qualified experts, and resilience to external factors such as illnesses and quarantines. At the same time, several significant limitations have been identified: decreased engagement due to distractions at home, technical issues, and challenges in organizing group work and monitoring comprehension.

End-of-year surveys indicate that students respond positively to the program's format, emphasizing its welcoming atmosphere, clarity of instruction, and motivation to explore the sciences.

In-person observations and practical training remain vital components of the program alongside online classes, helping to overcome one of the major shortcomings of distance learning – the lack of hands-on interaction with astronomical instruments.

The analysis demonstrates that the hybrid format of the program not only contributes to science outreach efforts, but also plays an important role in career guidance and in fostering public literacy in the natural sciences. To ensure successful development of such initiatives, it is essential to maintain a balance between the scalability of the online format and a personal approach to students. The experience of Asterion can serve as a model for establishing similar programs in other regions, advancing scientific literacy and helping to train the next generation of specialists in the natural sciences.

References

Belikova R. and Novolodskaya E., 2022, Pedagogical Perspective, 1, p. 57
Harvey D., Greer D., Basham J., et al., 2014, American Journal of Distance Education, 28, 1, p. 14
Kersha Y. and Obukhov A., 2023, Integration of Education, 27, 2, p. 208
Krupa T., Lebedev A., Obukhov A., 2021, MCU Jornal of Pedagogy and Psychology, 3, 57, p. 182
Parko I., Damm V., Simkina A., et al., 2016, Interexpo GEO-Siberia, 5, 2, p. 82
Novichonok A. and Skorikova N., 2015, Lifelong Education: The 21st Century, 1, 9, p. 62
Shiling G., 2023, Teacher of Altai, 2, 15, p. 57
Skorikova N. and Kuznetsova N., 2020, Nizhny Novgorod Education, 2, p. 24

On the 100th anniversary of Dmitry Viktorovich Korolkov

N. Nizhelsky

Special Astrophysical Observatory of the Russian Academy of Sciences,
Nizhny Arkhyz, 369167 Russia

DOI: 10.26119/2025-moc09 EDN: pazcey
eLocator: moc09

Abstract. Dmitry Viktorovich Korolkov (06.14.1925–01.10.1984) was a Soviet radio astronomer, Doctor of Sciences in physics and mathematics (1972). Dmitry Viktorovich was born in Gomel, Belarus. In 1942, he joined the Red Army as a volunteer and took part in the fighting of the Great Patriotic War. Dmitry Viktorovich was wounded twice and was demobilized in 1948. He was awarded State Awards – the Order of the October Revolution and the medals: For Battle Merit (twice), For the Defense of the Caucasus, and For the Victory over Germany (twice). D. V. Korolkov was the initiator of equipping the RATAN-600 radio telescope with highly sensitive receivers. First radiometers, including the cryogenic ones, were developed under his leadership. He was also a very cheerful and humorous person. This was evident from his funny drawings in wall newspapers.

Keywords: general: radio telescopes, continuum radiometers

I first met Dmitry Viktorovich on May 9, 1975. He was adjusting the antenna to the Sun at RATAN-600 feed cabin No. 1 (Korolkov and Pariiskii 1979). After our conversation, he tore off a piece of chart tape from the recorder, wrote down his address, and invited me and my wife to work. That was how our acquaintance with this remarkable man, and almost 50 years of work in the observatory, began.

Everything about him is unusual, even the facts of his biography. At the age of 17, he volunteered for the front in 1942 and took part in the unsuccessful Crimean Landing. Then, he said, he was enrolled in the reinforcements of the famous paratrooper detachment of Tsezar Kunikov, although that was after the brutal battles for Malaya Zemlya. They didn't accept everyone...

He graduated from the Leningrad Polytechnic Institute. Our colleague G. B. Gelfreich recalled that during his studies, student D. V. Korolkov failed the exam in radio engineering, and a few years later the same professor came to Korolkov to explain to him how it was possible to obtain a sensitivity several orders of magnitude better than the receiver's own noise, and the yesterday's student had to tell the professor about that very mysterious "radiometric gain" (the square root of receiver bandwidth multiplied by accumulation time). This was a completely new direction in radio engineering, and even in the 1970s everything related to radiometry was still printed in small print in textbooks on microwave electronics. He wrote in detail about radiometry and receiver designs in a section of the "handbook" for radio astronomers (N. A. Esepkina, D. V. Korolkov, Yu. N. Parijskij Radio telescopes and radiometers, Moscow, Nauka, 1973).

Dmitry Viktorovich was Head of the RATAN-600 Department of Radio Astronomy Instrumentation and supervised the development of the receiving equipment for solar observations, spectral studies, continuum, and antenna adjustments. In the absence of Yu. N. Parijskij, he always replaced him, solving all current problems. It can be said that he raised several generations of radiometry engineers for many scientific institutes in the country. He was not only my first supervisor but also a role model in everything: in work, in life, and in moments of rest.

Dmitry Viktorovich was phenomenal in his ability to convince and achieve results. I have seen his rationale for the construction of a new RATAN-600 Automation and Electronics Building: "But how can one justify such obvious things?! D. Korolkov." And in 1986 we had already moved to new laboratories. He planned there even a section for the technology of integrated circuits, which were so necessary for radio astronomy equipment.

Below, I will tell you about several developments of radio receiving equipment that he supervised. As a rule, he also participated in the most important works and experiments. At that time, there were still no suitable microwave transistor amplifiers, and the parametric amplifiers (paramps) were with the lowest noise. These were complex devices with ferrite circulators, the diodes worked on reflection, and they also needed microwave pumping. But paramps could be cooled down to cryogenic temperatures. The 3.9 cm radiometer, with which the first observation at RATAN-600 took place on July 12, 1974, was also based on parametric amplifiers with cooling. At first, liquid nitrogen was poured three times a day (8 liters of liquid nitrogen evaporated in 9–10 hours), then modern cryostats began to be used. There were also rules for constructing such radiometers: in each individual block there was no more than 20 dB of gain, the following stages were tunnel diodes, Gann diodes, and traveling-wave lamps. Klystrons were used as pumping, which required frequent adjustment. The modern radiometric module on HEMT microchips fits in the palm of your hand.

Korolkov D. led the creation of a highly sensitive cryogenic radiometer and the preparation of the RATAN-600 antenna for the first deep sky survey "Cold" (March 1978).

Sealing the slots and installing the grids covering the antenna foundation, as well as optimal irradiation of the antenna, made it possible to reduce its noise temperature by more than 10 K and reach 11.5 K. The 7.6 cm radiometer was built on the basis of a parametric amplifier pumped with Gann diodes (49 GHz) and cooled to 15 K by a closed-helium-cycle refrigerator. During the first survey of the sky, it was possible to obtain a then-record sensitivity of 5 mJy at 1 s of integration time.

His latest work concerned extremely deep two-dimensional sky surveys using a special conical secondary mirror and a highly sensitive cryogenic radiometer. In this observation mode, the entire

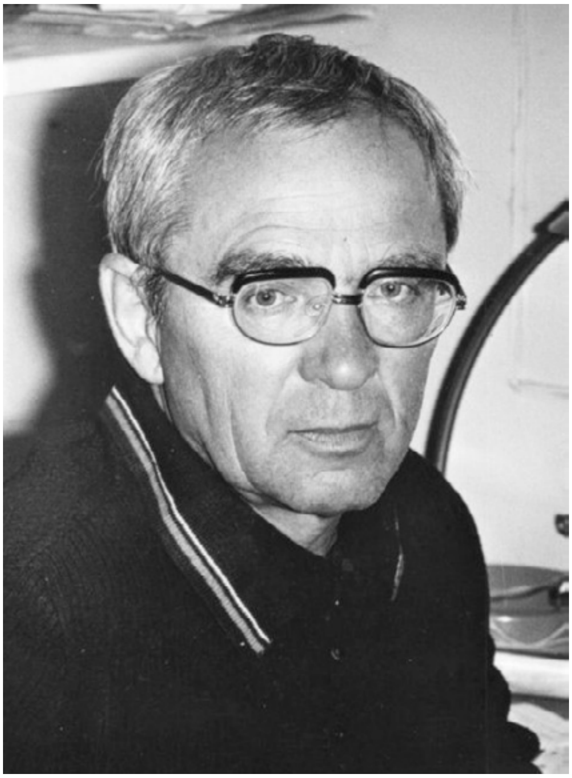

Figure 1. Dmitry Viktorovich Korolkov.

Figure 2. Generations of radiometer developers, D. V. Korolkov's fellows, at the RATAN-600 radio telescope.

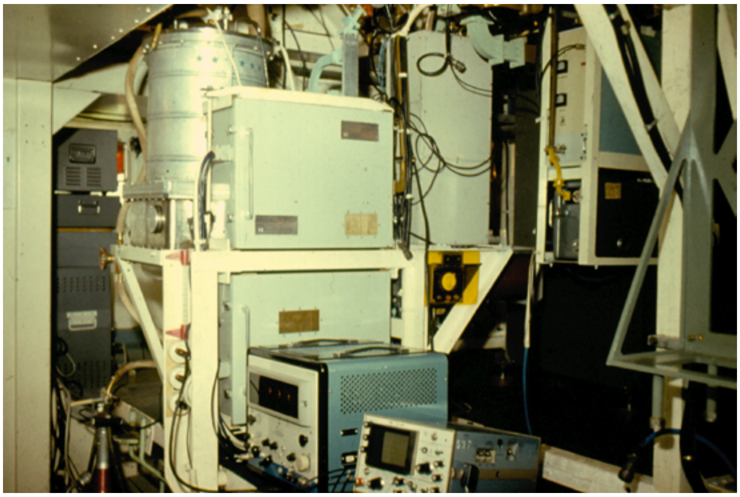

Figure 3. The first radiometers with parametric amplifiers at wavelengths of 3.9 and 2.08 cm.

Figure 4. Sealing the slots between the panels with aluminum foil to reduce noise at the Northern Sector of the antenna (D. V. Korolkov is on the right).

huge surface of the complete ring of the RATAN-600 antenna (about 14 000 square meters) was used, and it became possible to receive radiation from extremely weak radio sources. The first Zenith Field sky surveys were conducted after his death, in 1986.

The observations and life at the radio telescope were reflected in the issues of humorous wall newspapers. Dmitry Viktorovich had always been the editor-in-chief and the main artist, his comic drawings were always funny and kind. The most frequent hero of these drawings was the responsible scientist for RATAN-600, a corresponding member (and then a full member) of the Academy of Sciences Yury Nikolaevich Parijskij.

Every year, April 1st (Fool's Day) was celebrated with cocktails, jests, and practical jokes. Here is Order No. 13 of April 1st, 1981 on the transition of RATAN-600 to sidereal time: "The day that

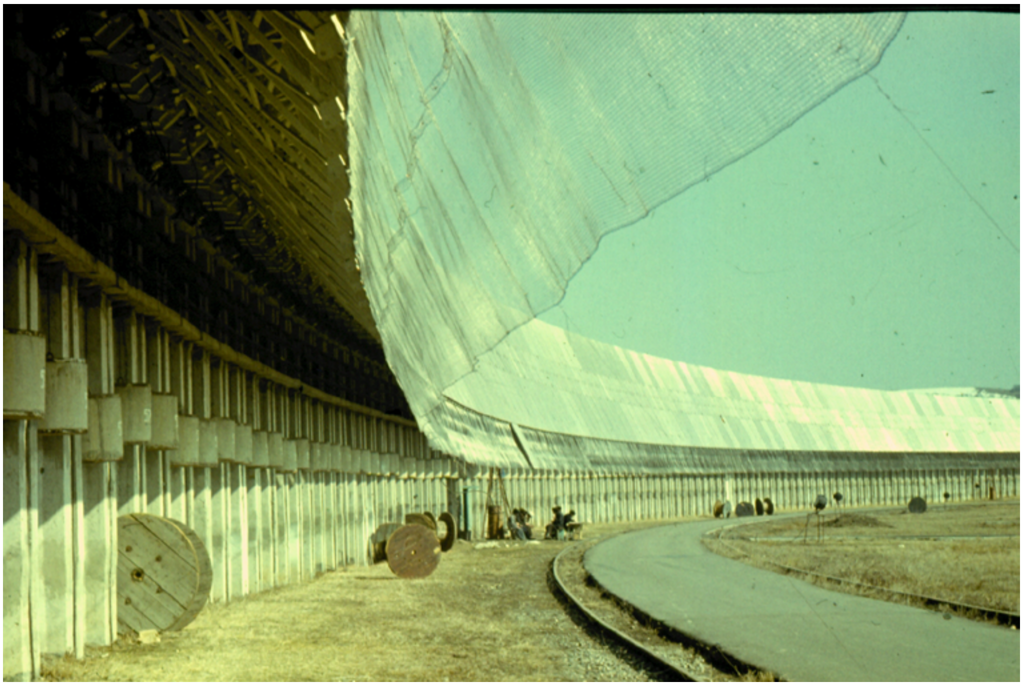

Figure 5. “Cooled” antenna.

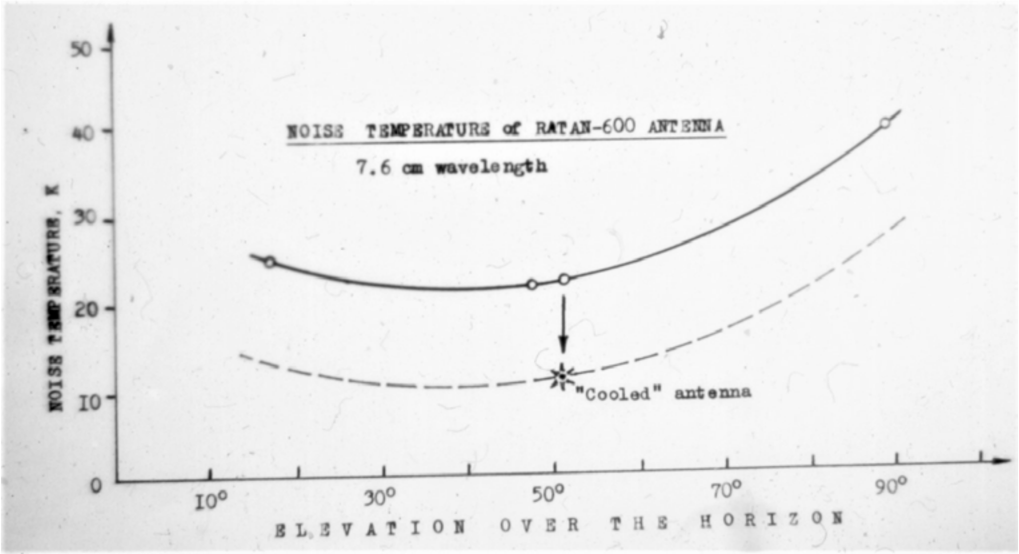

Figure 6. Noise temperature of the RATAN-600 antenna after the procedure of “cooling.”

accumulates throughout the year due to the difference between sidereal and solar times will be set as an annual day off on April 1st.”

Everyone who was lucky enough to work with Dmitry Viktorovich Korolkov will always have a bright memory of this extraordinary man and a wonderful teacher, who made a great contribution to the development of Russian radio astronomy.

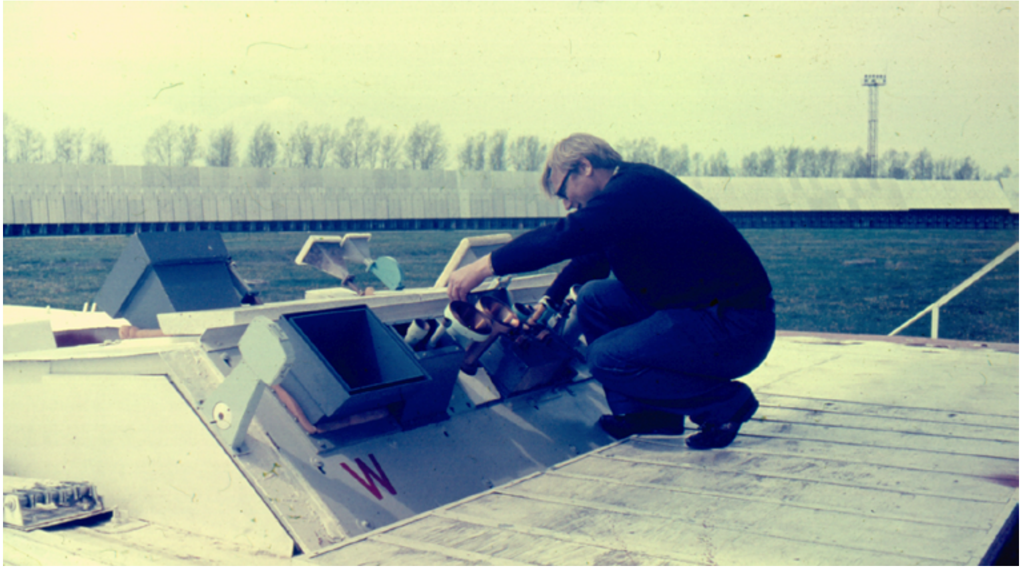

Figure 7. Focal line of secondary mirror No. 1 with the primary feeds.

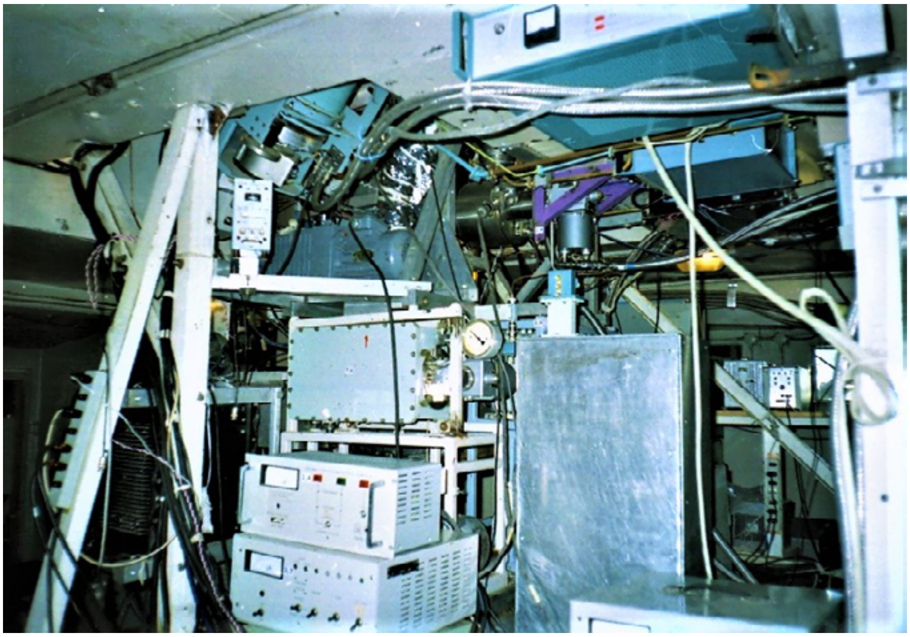

Figure 8. Cryogenic radiometer at a wavelength of 7.6 cm.

Figure 9. Without waiting for computer processing of the obtained files, Yu. N. Parijskij discovered “sources,” “just noise,” and “events” in the diagram tapes of the first “Cold” survey. The “events” turned out to be the work of the paramp pumping control and the “gaiety” of radiometer cooling. We had to eliminate them urgently.

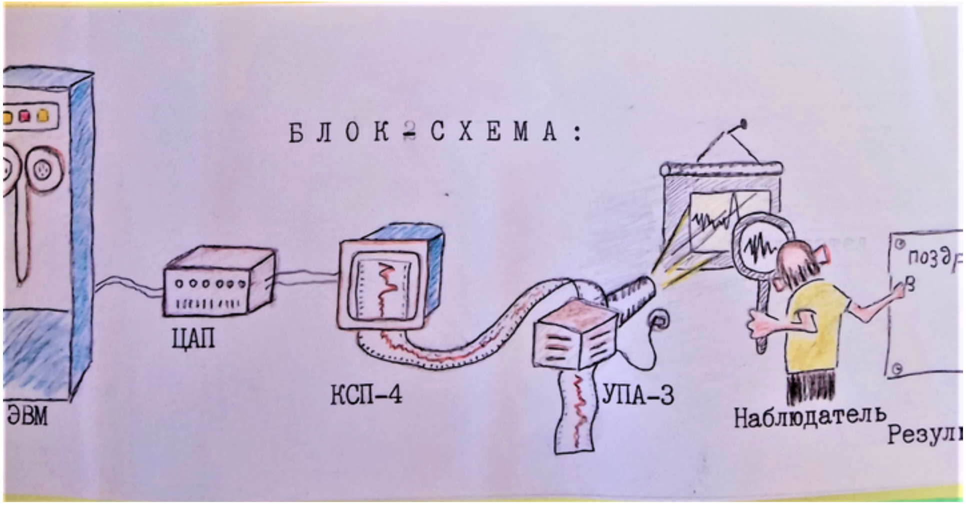

Figure 10. Another comic drawing is Yu. N. Parijskij’s processing of the “Cold” survey records using a children’s film strip projector. A comic copyright certificate, very similar to a real one, was also issued for this processing method.

Figure 11. An invitation to take advantage of a unique opportunity to look beyond the Border of the Universe!

Figure 12. The RATAN-600 precise time service.

Figure 13. Excursion to RATAN-600 for the Zelenchuk school-seminar on SETI at the Special Astrophysical Observatory (V. S. Troitsky, I. S. Shklovsky, D. V. Korolkov, October 1975).

References

Korolkov D.V. and Pariiskii Iu. N., 1979, Sky and Telescope, 57, p. 324

Modern Observational Cosmology
Dedicated to the 60th anniversary of O.V. Verkhodanov
May 21-24, 2025, SAO RAS, Nizhny Arkhyz, Russia

High-frequency peaked radio sources

K. Iuzhanina[1] · **A. Mikhailov**[1] · **Yu. Sotnikova**[1] · **V. Vlasyuk**[1] · **D. Kudryavtsev**[1] · **T. Mufakharov**[1] · **Yu.A. Kovalev**[2] · **Yu.Yu. Kovalev**[3] · **A. Popkov**[2,4] · **M. Kharinov**[5] · **M. Khabibullina**[1] · **A. Volvach**[6] · **L. Volvach**[6]

[1] Special Astrophysical Observatory of the Russian Academy of Sciences, Nizhny Arkhyz, 369167 Russia
[2] Astro Space Center, Lebedev Physical Institute, Russian Academy of Sciences, Moscow, 117997 Russia
[3] Max-Planck-Institut für Radioastronomie, Auf dem Hügel 69, 53121 Bonn, Germany
[4] Moscow Institute of Physics and Technology, Institutsky per. 9, Dolgoprudny, 141700 Russia
[5] Institute of Applied Astronomy, Russian Academy of Sciences, Kutuzova Embankment 10, St. Petersburg, 191187 Russia

[6] Crimean Astrophysical Observatory of the Russian Academy of Sciences,

Nauchny, 298409 Russia

DOI: 10.26119/2025-moc10
eLocator: moc10
EDN: kaqgqa

Abstract. We present a study of the multiwavelength properties of high-frequency peaked (HFP) radio sources. The study involved the simultaneous RATAN-600 measurements at frequencies of 1.2, 2.3, 4.7, 8.2, 11.2, and 22.3 GHz in 1997–2024, the RT-32 measurements at 5.05 and 8.63 GHz (IAA RAS), the RT-22 data at 36.8 GHz (CrAO RAS), and the literature data. It was found that the variability of the HFP synchrotron emission is relatively low, it reaches 0.02–0.23 on the monitoring time scale of 17–27 years. Modeling of the broadband radio spectra of HFP sources shows that they can be satisfactorily described both by synchrotron self-absorption and by free-free absorption. For two of the sources, PKS 1614+051 and PKS 2126−158, we calculated the evolution of the synchrotron self-absorption spectrum parameters and the magnetic field strength. The results of the optical spectroscopical study of PKS 1614+051 and PKS 2126−158, performed with the SCORPIO-1 spectrograph at the 6-meter telescope, revealed that they have different internal structures and are located in different galactic environments.

Keywords: galaxies: active; radio continuum: galaxies; methods: observational

SAO RAS, Nizhny Arkhyz, Russia 2025 https://cosmology2025.ru

1. Introduction

Understanding the origin and evolution of radio emission in extragalactic radio sources remains a central problem in modern astrophysics. In the evolutionary scenario, the physical size of a radio source is directly related to its age. Compact peaked-spectrum (PS) radio sources are therefore considered progenitors of classical radio galaxies (Fanti 1995). An empirical anticorrelation between the spectral peak frequency ν_m (also called the turnover frequency) and the projected linear size of the source (O'Dea & Baum 1997) indicates that high-frequency peaked (HFP) sources can be the youngest objects. HFP sources exhibit a convex broadband radio spectrum with a peak above 5 GHz and are thought to represent newly born radio sources with ages of only 10^2–10^3 years (Dallacasa et al. 2000; Dallacasa 2003). Their spectra are generally explained by synchrotron self-absorption (SSA) or free-free absorption (FFA) (see, e.g., Tingay & de Kool 2003).

The radio properties of HFP sources have been established mainly through bright-source samples (Dallacasa et al. 2000; Orienti et al. 2006). Two populations can be distinguished based on their spectral variability. One consists of the sources with a persistent convex spectrum and little variability, interpreted as genuinely young radio galaxies in an early evolutionary stage. The other consists of objects with strongly variable spectra, which are instead jet-dominated, beamed sources, i.e., blazars (Orienti et al. 2010). Supporting this view, Massaro et al. (2009) included all known PS sources in the Roma-BZCAT blazar catalogue. It is therefore important to distinguish between genuinely young HFP sources and blazar contaminants. Genuine HFP sources are compact symmetric objects or compact doubles, characterized by small projected sizes (≤ 100 pc), stable convex spectra, and weak variability. In contrast, blazar-like HFP sources are core-jet objects where a new, self-absorbed jet component can temporarily mimic a peaked spectrum at high frequencies. Their spectra evolve rapidly, showing variability and flattening over time. Thus, long-term spectral monitoring combined with the morphology obtained from very long baseline interferometry (VLBI) is essential to discriminate between young HFP galaxies/quasars and beamed blazar sources.

Multiwavelength studies of HFP sources are a powerful tool for investigating both the nature of young active galactic nuclei (AGNs) and the properties of their environment. Particularly intriguing are HFP sources at high redshifts ($z > 3$), corresponding to the cosmic epoch when the Universe was only about 15% of its present age, and AGNs were at the earliest evolutionary stages.

In this paper we analyze the long-term radio properties of five HFP candidates: J0927+3902, J0555+3948, J0428+3259, PKS 1614+051 (Sotnikova et al. 2024), and PKS 2126−158, selected from the RATAN-600 long-term blazar monitoring program, and investigate their variability and spectral evolution on time scales of up to nearly three decades.

2. Radio observations

The spectral flux densities were measured with the RATAN-600 radio telescope at 1.2, 2.3, 4.7, 8.2, 11.2, and 22.3 GHz in 1997–2024 (Kovalev et al. 1999; Mingaliev et al. 2012; Sotnikova et al. 2022), with the RT-22 radio telescope (CrAO RAS) at 36.8 GHz (PKS 1614+051, PKS 2126−158), and with the RT-32 radio telescope (IAA RAS) at 5.05 and 8.63 GHz. Since the observing frequencies of the RT-32 and RATAN-600 are close, we use their rounded values, 8 and 5 GHz, in the analysis. The other frequencies, 36.8, 22.3, 11.2, 2.3, and 1.2 GHz, are also used in rounded form: 37, 22, 11, 2, and 1 GHz. Some of the flux density measurements were taken from the interactive RATAN-600 Multi-Frequency Catalogue of Blazars—BLcat.[1] To construct quasi-simultaneous radio spectra, the spectral flux densities obtained with different telescopes must be averaged over a certain time period. We chose the interval of 39 days for PKS 1614+051 and PKS 2126−158 to get the maximum number of quasi-simultaneous radio spectra with flux densities measured at at least four frequencies. The quasi-simultaneous radio spectra of PKS 2126−158 are presented in Fig. 1.

---

[1] https://www.sao.ru/blcat/

Table 1. Timescale of observations

Name	z	Epoch	N_{sp}
J0428+3259	0.47	2006–2023	13
J0555+3948	2.36	1997–2024	21
J0927+3902	0.69	1997–2023	16
PKS 1614+051	3.21	1997–2024	48
PKS 2126−158	3.26	1997–2024	65

Table 2. Fractional variability for HFP candidates at different frequencies

ν, GHz	PKS 1614+051	PKS 2126−158	J0927+3902	J0555+3948	J0428+3259
22	0.12±0.04	0.23±0.2	0.20±0.02	–	0.15±0.04
11	0.18±0.01	0.19±0.1	0.14±0.02	–	0.04±0.03
8	0.16±0.07	0.20±0.1	0.14±0.01	–	0.07±0.02
5	0.10±0.07	0.15±0.1	0.08±0.01	0.01±0.02	0.02±0.03

The redshifts z of the sources, the monitoring timescale, and the number of radio spectra N_{sp} that have been modeled are presented in Table 1. The longest timescales in the observer's frame of reference is 27 years (1997–2024), reached for the sources J0555+3948, PKS 1614+051, and PKS 2126−158. In the rest frame these timescales vary from 2 to 8 years.

3. Radio variability

The radio variability level is one of the HFP source classification criteria along with the frequency of the spectral maximum. It is generally considered that the variability of the HFP source radio emission does not exceed 0.2 (or 20%). We have evaluated the variability level using the fractional variability index F_{var} (Vaughan et al. 2003). The results at 5, 8, 11, and 22 GHz are presented in Table 2. The least variable sources are J0555+3948 and J0428+3259, with fractional variabilities at 5 GHz of 0.01 and 0.02 on monitoring timescales of 27 and 17 years, respectively. For J0555+3948 we could not calculate the fractional variability at 8, 11, and 22 GHz because the variance was less than the mean square error for these frequencies. J0927+3902 is more variable: $F_{\text{var}} = 0.08$ at 5 GHz, 0.14 at 8 and 11 GHz, and 0.20 at 22 GHz. PKS 1614+051 and PKS 2126−158 are the most variable sources with fractional variability of 0.10 and 0.15 at 5 GHz and 0.18 and 0.19 at 11 GHz.

4. Modeling of broadband radio spectra

The broadband radio spectra have been modeled with the SSA model derived in (Türler 1999), homogeneous SSA model, homogeneous external FFA model, internal FFA model, and inhomogeneous external FFA model (see, e.g., Shao 2022). We compared how the models fit the observed data by calculating the Bayes factor (BF) from marginal likelihoods (evidence) using the UltraNest library (Buchner 2021). The model parameters in the case of SSA (Türler 1999) are as follows: turnover frequency (ν_{m}), flux density at the turnover frequency (S_{m}), spectral index in the optically thin part of the spectrum (α_{thin}), and spectral index in the optically thick part of the spectrum (α_{thick}). In the case of inhomogeneous external FFA, the model parameters are the normalization parameter (S_{norm}), turnover frequency (ν_p), spectral index (α), and gamma function parameter

(p) that corresponds to the distribution of absorbing clouds. Parameters for other models can be found in Shao (2022).

All of the aforementioned models described the majority of spectra of J0428+3259 with rather large errors. It can be assumed that in the case of J0428+3259 the double SSA + FFA model (see, Orienti & Dallacasa 2008 for details) should be used to fit the broadband radio spectra obtained with RATAN-600. The preferred double model reflects the contributions from multiple components, such as a compact SSA-dominated core along with an extended region absorbing via FFA. It means that the source has a hybrid nature: a compact synchrotron emission partially obscured by thermal plasma, which potentially indicates a young AGN embedded in a dense environment.

In the case of J0555+3948, the SSA (Türler 1999) and inhomogeneous FFA models provide the best fits in spectra modeling. The Bayes factor varies from 2 to 11 for different 1997–2022 spectra (moderate evidence in favor of SSA over inhomogeneous FFA). The SSA radio spectra modeled for the 1997–2024 period are presented in Fig. 2. In 1997 the ν_m value is 5.8 GHz, then in other epochs it increases and reaches 7.1 GHz. Since 2018 the turnover frequency has been no more than 5.1 GHz. The spectral flux density for this source has been decreasing for 23 years: in 1997 the flux density at the spectral peak was 6.4 Jy, in 2020 this value dropped to 4.2 Jy.

In modeling the J0927+3902 spectra, the SSA inhomogeneous FFA models are also best suited. The Bayes factors, when comparing these two models for the 2006–2010 spectra, range from 1 to 2, which is insignificant according to Jeffreys' scale and its modifications. For some spectra the model parameters have been obtained with large errors, which indicates that they should be fitted with a combination of different models or the lack of 1 GHz measurements at some epochs is the cause of the poor model approximation. Examples of modeled spectra for J0428+3259 and J0927+3902 are shown in Fig. 3.

For PKS 1614+051 the median Bayes factor is close to 1 (when comparing the SSA and inhomogeneous FFA models). For PKS 2126-158 it was noticed that some of the earlier spectra (1997–2012) have two peaks, which is illustrated in Fig. 4. The two-peak shape of the spectrum may indicate the appearance of a new component contributing to the high-frequency part of the spectrum. Perhaps such spectra should be modeled using, for example, the SSA + FFA model to allow for the contribution of the second component. For details on double models, see Shao (2022). The ν_m value for later epochs, where a two-peak structure has not been longer observed, does not show a decreasing trend. Despite the fact that PKS 2126−158 is the most variable source in the presented sample and has a core-jet morphology, its spectrum has remained convex for more than 27 years.

For PKS 1614+051 and PKS 2126−158, we have calculated magnetic field strength (for details see Sotnikova et al. 2024), and its value varies from 13 mG to 112 mG for PKS 1614+051 and from 4 mG to 90 mG for PKS 2126−158.

5. Optical spectroscopy

The spectroscopy of PKS 1614+051 and PKS 2126−158 was performed at the 6-meter telescope (BTA) with the SCORPIO-1 spectrograph (Afanasiev and Moiseev 2005) under good weather conditions: almost ideal atmosphere's clarity and a seeing of about $1.''5$ (measured as the full width at half maximum of stellar spectra in individual exposures—this value is more correct for spectral data analysis). We used a $1.''2$-wide slit in combination with the VPHG1200B grism from the SCORPIO-1 standard set.[2] The resulting spectral resolution was about 0.6 nm across the total spectral range between 360 and 540 nm. The total exposure was combined from several individual 10-min exposures. The details of the PKS 1614+051 observations, its optical spectrum, and the obtained results can be found in (Sotnikova et al. 2024).

---

[2] https://www.sao.ru/hq/lsfvo/devices/scorpio/scorpio.html

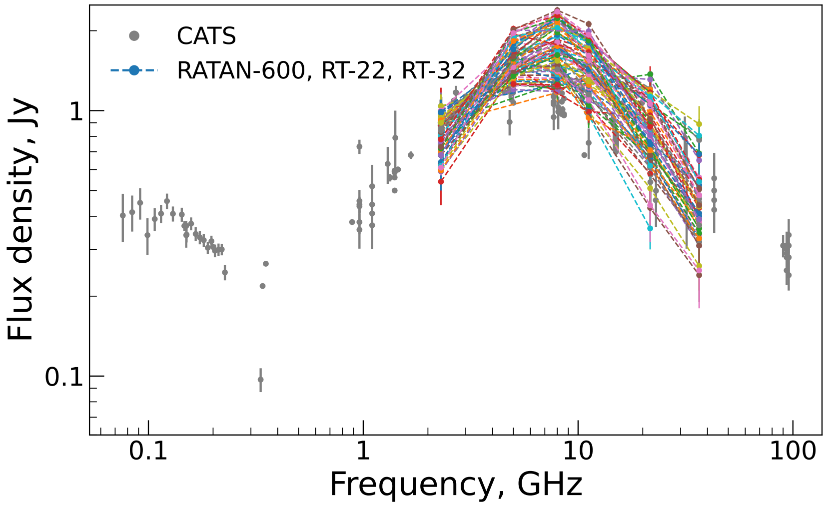

Figure 1. The quasi-simultaneous radio spectra of PKS 2126−158. The data from RATAN-600, RT-32, and RT-22 were obtained in 1997–2024 (colored). The measurements from the CATS database are shown with grey dots.

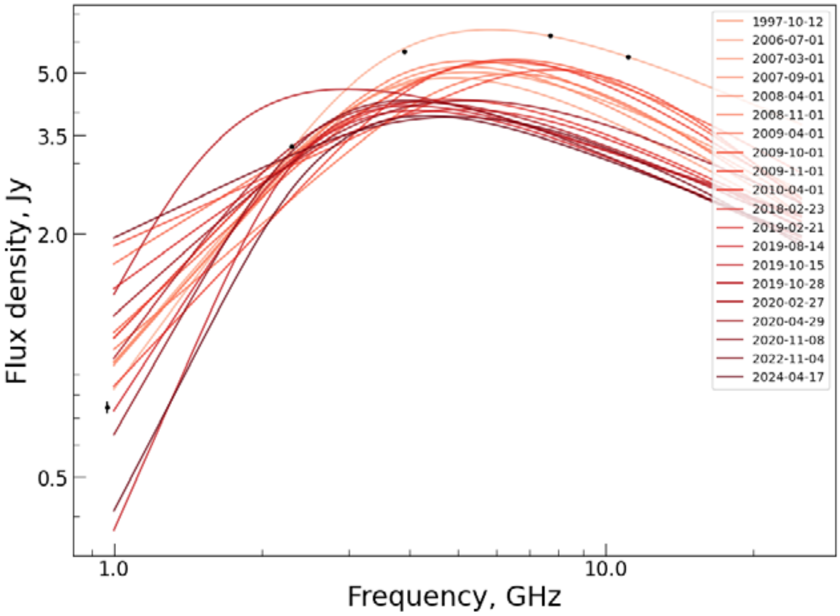

Figure 2. The SSA broadband radio spectra of J0555+3948 modeled for the period of 1997–2024. For illustration, the RATAN-600 data for the 1997-10-12 spectrum are shown with black dots.

In the observations of PKS 2126−158, the slit of the spectrograph was placed across the images of the blazar and the two nearest galaxies located to the west from it. The spectra are presented in Fig. 5. The spectrum of the blazar PKS 2126−158 shows a broad Lyα emission and a rich set of absorption lines in the spectral range between 380 and 520 nm. Most of them have been identified in the previous papers (e.g., Whiting et al. 2006). The obtained spectra of the galaxies have one significant emission line, which is identified with the forbidden line of ionized oxygen [OII] λ 372.7 nm. The redshifts of the foreground galaxies SDSS J212911.80-153841.2 and SDSS J212911.52−153840.8—numbers 1 and 2, respectively—are equal to 0.2392 ± 0.0003 and 0.2092 ± 0.0003. The PKS 2126−158 spectrum demonstrates the absorption doublets of [CaII] $\lambda\lambda$ 393.3 &

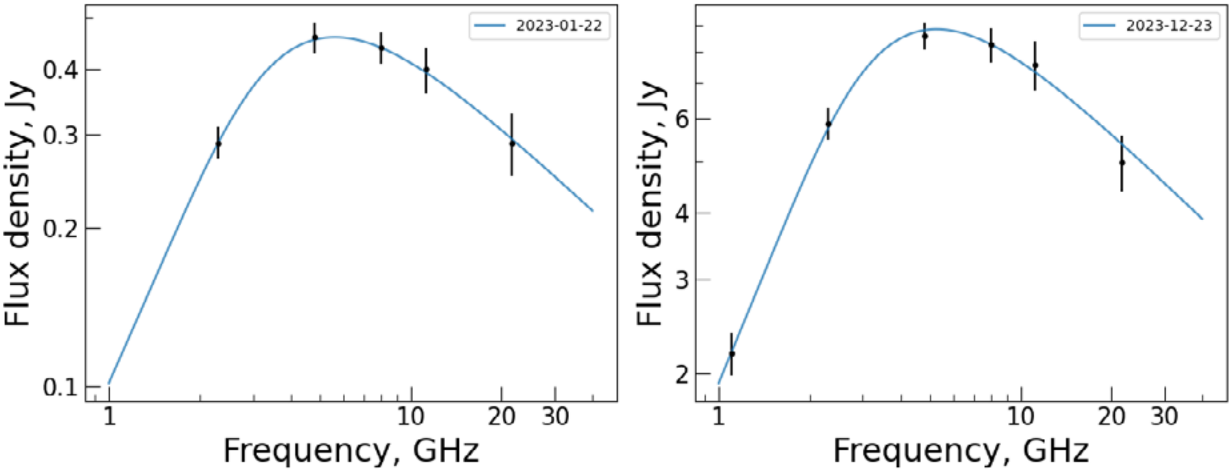

Figure 3. Examples of modeled spectra for J0428+3259 (left) and J0927+3902 (right). The RATAN-600 data are shown with black dots. The best fitting (SSA model) is shown with blue curves.

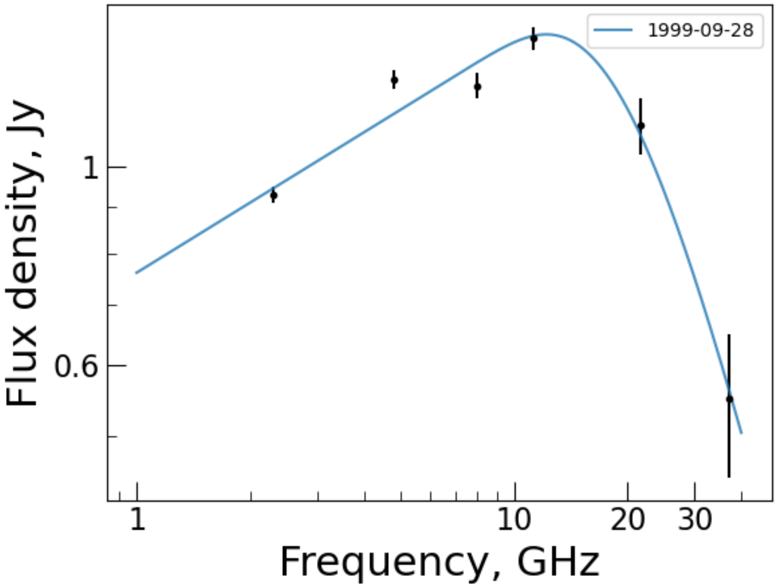

Figure 4. An example of the two-peaked spectrum for PKS 2126−158. The RATAN-600 data are shown with black dots. The best fitting (SSA model) is shown with a blue curve.

396.8 nm at the redshifts of these galaxies. The projected distances of the centers of the galaxies from the line of sight equal to 19 and 35 kpc, respectively.

The spectral studies of PKS 1614+051 and PKS 2126−158 conducted with BTA SCORPIO-1 and at other telescopes (Whiting et al. 2006; Husband et al. 2015) have shown significant differences both in their internal structure and in the presence/absence of a galactic environment. The blazar PKS 1614+051 is located in a dense galactic environment and shows the presence of a gaseous cloud (or disk) with size about 50 kpc; some nearby galaxies emit in Lyα (Husband et al. 2015). The blazar PKS 2126−158 is most likely isolated. Our data and the data taken with the Gemini Multi-Object Spectrograph (GMOS) show that all neighboring galaxies are located at intermediate distances: at redshifts between 0.2 and 0.8 (Whiting et al. 2006). More distant galaxies have not

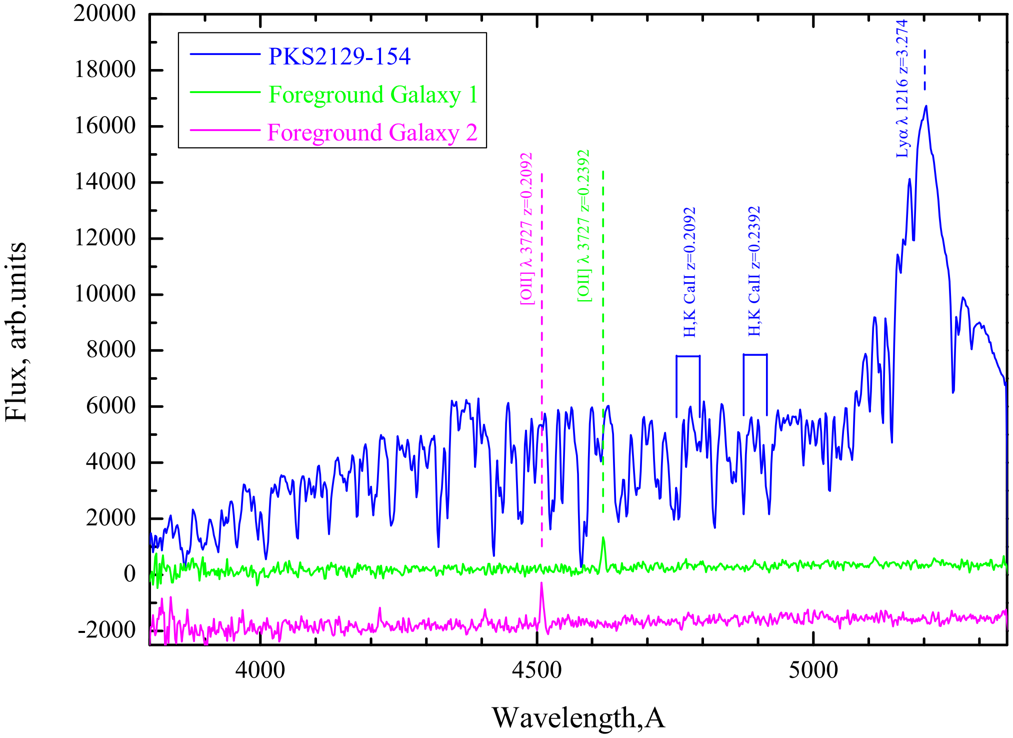

Figure 5. The optical spectra of PKS 2126−15 (blue line) and the neighboring galaxies numbered as 1 and 2 above. The data are presented in relative units. The spectra of galaxies are multiplied by a factor of 5 and shifted along the y-axis for better viewing. The vertical lines mark the emission lines of the blazar, the [OII] 372.7 nm emission lines in the galactic spectra, and the CaII absorptions.

yet been revealed in the field around the blazar. It was established that PS sources tend to reside in groups (Orienti et al. 2010).

6. Summary

We found that the radio variability of the considered HFP blazars is moderate on long timescales from 2 to 8 years (the rest frame). In general, fractional variability reaches ~ 0.2, which is less than the variability observed in most blazars. The flux densities of the HFP blazars have been changing smoothly for several decades, and their spectrum shapes remain almost constant, demonstrating insignificant shifts of the peak frequency.

There is no uniformity among the sources: while SSA is preferable in one case (J0555+3948), the choice between FFA and SSA cannot be made for J0927+3902 and PKS 1614+051 (BF ≤ 2), and a hybrid model is recommended for J0428+3259. These results support the idea that HFP sources are young compact AGNs, in many cases with SSA-driven turnovers determined by intrinsic jet properties (magnetic fields, particle densities). However, the FFA contribution (especially the external inhomogeneous FFA) implies interactions with the environment, such as absorption of the radio emission by ionized gas in the host galaxy.

The low radio variability level makes evolutionary trends more detectable than in the flaring sources. The anomaly in the behavior of the J0555+3948 flux density implies that not all HFP sources follow the standard models: additional processes such as adiabatic losses, entrainment, or variable accretion might be needed.

Despite their similar spectral shape and variability, PKS1614+051 and PKS2126−158 are located in different environments, as shown by a spectroscopic analysis. PKS 1614+051 is located in a dense galactic environment with nearby galaxies emitting in Lyα and shows the presence of a gaseous cloud (or disk), while PKS 2126−158 is most likely isolated.

Acknowledgements Observations with the SAO RAS telescopes are supported by the Ministry of Science and Higher Education of the Russian Federation. The renovation of telescope equipment is currently provided within the national project “Science and Universities”. This research has made use of the NASA/IPAC Extragalactic Database (NED), which is operated by the Jet Propulsion Laboratory, California Institute of Technology, under contract with the National Aeronautics and Space Administration; the CATS database, available on the Special Astrophysical Observatory website.

References

Afanasiev V.L. and Moiseev A.V., 2005, Astronomy Letters, 31, p. 194
Buchner J., 2021, Journal of Open Source Software, 6, 60
Dallacasa D., Stanghellini C., Centonza M., et al., 2000, Astronomy and Astrophysics, 363, p. 887
Dallacasa D., 2003, PASA, 20, 1, p. 79
Fanti C., Fanti R., Dallacasa D., et al., 1995, Astronomy and Astrophysics, 302, p. 317
Husband K., Bremer M.N., Stanway E.R., et al., 2015, Monthly Notices of the Royal Astronomical Society, 452, p. 2388
Kovalev Yu.Yu., Nizhelsky N., Kovalev Yu.A., et al., 1999, Astronomy and Astrophysics Supplement Series, 139, p. 545
Massaro E., Giommi P., Leto C., et al., 2009, Astronomy and Astrophysics, 495, 2, p. 691
Mingaliev M., Sotnikova Yu., Torniainen I., et al., 2012, Astronomy and Astrophysics, 544, id. A25
O’Dea C.P. and Baum S.A., 1997, Astronomical Journal, 113, p. 148
Orienti M. and Dallacasa D., 2008, Astronomy and Astrophysics, 487, p. 885
Orienti M., Dallacasa D., Stanghellini C., 2010, Monthly Notices of the Royal Astronomical Society, 408, 2, p. 1075
Orienti M., Dallacasa D., Tinti S., et al., 2006, Astronomy and Astrophysics, 450, 3, p. 959
Shao Yali, Wagg Jeff, Wang Ran, et al., 2022, Astronomy and Astrophysics, 659, id. A159
Sotnikova Yu., Mikhailov A., Volvach A., et al., 2024, Astrophysical Bulletin, 79, 4, p. 548
Sotnikova Yu., Mufakharov T., Mingaliev M., et al., 2022, Astrophysical Bulletin, 77, 4, p. 361
Tingay S.J. and de Kool M., 2003, Astronomical Journal, 126, 2, p. 723
Türler M., Courvoisier T.J.-L., and Paltani, S., 1999, Astronomy and Astrophysics, 349, p. 45
Vaughan S., Edelson R., Warwick R.S., et al., 2003, Monthly Notices of the Royal Astronomical Society, 345, 4, p. 1271
Whiting M.T., Webster R.L., Francis P.J., 2006, Monthly Notices of the Royal Astronomical Society, 368, p. 341